UNIVERSITY OF EXETER

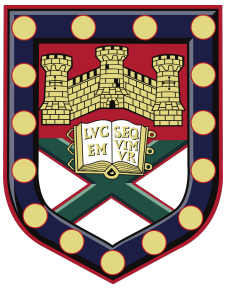

DOCTORAL THESIS

Optical and Electronic Study of Hybrid Light-Matter States

Author:

Henry FERNANDEZ

Supervisors:

Prof. William L. BARNES

Prof. Saverio RUSSO

A thesis submitted in fulfillment of the requirements

for the degree of Doctor of Philosophy

July 2019

Declaration of Authorship

'Optical and Electronic Study of Hybrid Light-Matter States'

Submitted by Henry Alexander Fernández Pizarro to the University of Exeter for the degree of Doctor of Philosophy, July 2019.

I certify that all material in this thesis which is not my own work has been identified and that any material that has previously been submitted and approved for the award of a degree by this or any other University has been acknowledged.

I acknowledge financial support from the Engineering and Physical Sciences Research Council (EPSRC) of the United Kingdom, via the EPSRC Centre for Doctoral Training in Metamaterials (Grant No. EP/L015331/1).

Signed: 

Date: July 10, 2019

Abstract

Hybrid light-matter states are quantum states that result from an efficient combination of light and matter. This combination is efficient when the two constituents exchange their energy faster than the overall energy dissipation. For such efficiency, devices have to be designed and structured to maximise the energy exchange. When an efficient energy exchange between light and matter is achieved, new quasiparticles are formed. One type of these particles are the exciton-polaritons, which result from an efficient energy exchange between excitons and a confined light field.

Over the past 40 years, exciton-polaritons have been extensively studied in conventional semiconductors integrated with devices that confine a light field. However, only in the last five years have exciton-polaritons have been realised in semiconductors with a thickness at the monolayer limit. This was first observed at low temperatures, and later extended to observations at room temperature. These devices performing at room temperature and at the nano-scale are promising for future technologies. Exciton-polaritons may play an important role due to their combined light and matter properties that provide them with the strong non-linearities necessary for quantum communications among other applications. However, one crucial step for the use of exciton-polaritons in real applications is the control over their formation. Recent reports elucidate ways to control the excitation of exciton-polaritons at room temperature, using semiconductor transistors integrated with light confinement devices. This control over the excitation of exciton-polaritons is the main focus of the work presented in this thesis. Previous reports have focused their research in controlling either the light confinement or the excitonic properties of the semiconductor material in separate ways. In this work both have been carefully controlled, allowing for an extended manipulation of exciton-polariton states.

The results presented here set a substantial advance on the manipulation of exciton-polaritons in devices operating at room temperature and using 2-dimensional semiconductor materials in tuneable optical microcavities. These results may lead to applications in future quantum technologies through switchable quantum states.

Acknowledgements

This doctoral thesis is a tangible result in the culmination of a great journey that started four years ago. Many people, in one way or another contributed to making this journey a great experience, which helped me to grow up as a researcher. I am immensely grateful to all of them.

I want to express my deepest gratitude to my supervisors Bill Barnes and Saverio Russo for their continuous support during my PhD research experience. I have learnt from them not only about how to gain knowledge in Physics but also about passion, determination, resilience, and integrity in this fantastic career. I want to thank Bill, especially for always believing in my success and for conducting my research paying attention to many other aspects that helped me to become a better researcher. I want to thank Freddie Withers for his essential contribution and enormous support in my research, without which I would not have achieved the experimental results described in this thesis. I am also immensely grateful to all of those who form part of the Centre for Doctoral Training in Metamaterials of the University of Exeter, staff members and students.

I am especially grateful to my friends, for so many happy moments that I will hold in as my best memories. I will not write down your names guys, so you will not think of what is your position in a list of people. But you know that you are special to me if we went together for a run, or if we were together playing football, basketball or volleyball, even under yellow-warning rain showers and strong winds. You are special to me if we were together in a music festival, or in a music band, or if we danced together at any of those crazy parties and barbecues. I will always remember you guys. You are all at the top of my dearest friends. I also want to thank all of those who were not here, but who

kept constant communication with me; to my family, for being just great all this time. Thanks to my mom and dad for helping me to get started in this journey, and for the great support through all this time even being so many miles away.

Now, I will write your name Constanza, but you have to forgive me for not even trying to find the words to thank you enough, for I fear I will fail. I can only say that I would not be here if you were not here with me and that I want to dedicate this book to you, with my deepest love.

Dedicated to Constanza

Contents

List of Figures

List of Tables

Chapter 1

Introduction

In a hybrid light-matter state, light and matter particles exchange their energy at a higher rate than the overall energy dissipation. This efficient energy exchange leads to the formation of new quasiparticles, whose properties are a combination of light and matter properties, such as an effective mass ~10^{-11} times the mass of an atom [1]. This hybridisation has proven to be an exciting platform for the study of many rich physical phenomena, such as Bose-Einstein condensation [2], superfluidity [3–5], and topological polaritons [6]. Additionally, these light-matter quasiparticles may provide the strong non-linearities for photon-photon interactions highly sought after for future quantum technologies [7].

Exciton-polaritons are a type of hybrid light-matter state that are a result of efficient energy exchange between excitons and a confined light field. Confining the light field is crucial to strengthening the energy exchange as the energy losses are reduced significantly. Different devices can be used to confine the light field, such as plasmonic arrays and optical microcavities.

A type of optical microcavities, the Fabry-Pérot microcavities, are composed of two semitransparent flat mirrors, usually made of a thin metallic film. A portion of the spectral composition of light is confined in between these two metallic mirrors, where this portion depends on the separation of the mirrors, or

the cavity length. The wavelength of this spectral portion is linearly dependent on the cavity length, and the width of this portion depends on the energy loss of the light field; larger losses lead to larger peak widths. One way to reduce the cavity losses is to use mirrors thick enough to reduce scattering through them, and thin enough at the same time to allow for light to pass through the two mirrors in order to detect this spectral portion of the light confinement. The wavelength that is confined, which depends on the cavity length, is called the resonant wavelength. The energy associated with this resonance is $E = \hbar c / \lambda$, where $\hbar$ is the Planck constant, c is the speed of light in free space, and λ the resonant wavelength of the microcavity.

Excitons are electron-hole pairs formed in a semiconductor material. This electron-hole pair remains bounded through a Coulomb interaction. Excitons can be excited through light absorption, where an electron of the valence band in the semiconductor material absorbs a photon with enough energy to allow the electron to occupy the next available state in the conduction band of the semiconductor. This electron-hole pair is unstable, so the electron decays to the valence band in a recombination process, mediated by the emission of a photon with energy equal to the energy difference between the conduction and valence bands. If this excitonic semiconductor material is inserted into an optical microcavity, excitons are excited through the absorption of cavity photons. In the recombination of excitons, the released photons can also be confined in the microcavity, enhancing the rate at which excitons are excited and recombined.

When the excitation and recombination of excitons mediated by cavity photons occurs at a rate larger than the loss rate of photons, the overall exciton-cavity system enters a new hybrid state, and the energy level of the cavity photons and excitons splits into two states that form the hybrid system. The

splitting between the two states of the hybrid system is related to the rate at which energy flows from cavity photons to excitons and at which it flows back to the cavity. This rate is called the Rabi cycle per unit time. The faster the energy exchange, or the Rabi cycle, the larger the splitting of the hybrid state. This new hybrid state is called exciton-polariton.

To use exciton-polaritons in real applications, control over their properties is essential. In this thesis, I present a study on control over the excitation of exciton-polaritons. This control is achieved through manipulating the energy of the cavity photons, for which I implemented a tuneable microcavity system that allows for the control of the cavity length with nanometer precision at room temperature. Moreover, the control is also achieved through strengthening or weakening the ability of excitons to couple to light. To control the exciton strength, the semiconductor material was structured in a field effect device, which was embedded in the optical microcavity. Electrical control allows for the manipulation of the density of free charge carriers populating the conduction band of the semiconductor material through field-effect gating. A high density of charge carriers produceds a decrease in the excitation rate of excitons; therefore, the coupling with light is significantly reduced until exciton-polaritons disappear. I also studied electrical control over the exciton energy exchange between two different semiconductor materials, which to the best of my knowledge, resulted in the first observation of this control using 2-dimensional semiconductors.

In summary, in this thesis, I implemented an optical setup that can tune the resonant energy of an optical microcavity, which allows for the control over the formation of exciton-polaritons through the manipulation of cavity photons. Additionally, I implemented an electrical control over the strength of excitons in the semiconductor material, which allows for the study of the control of

exciton-polaritons through the manipulation of excitons. Both ways of control were achieved at room temperature.

1.1 Overview

This thesis is structured such that a description of the concepts used throughout the study form part of Chapter 2. I give a concise historical overview of light-matter interactions, starting from the very first reported observations by pre-Socratic Greek philosophers, followed by observations reported by Newton and Huygens from the two controversial corpuscle and wave theory of light, and I end this story with the description of light from the foundations of quantum mechanics. Following the historical overview of light-matter interactions, I describe the main concepts that form part of this research: light confinement, energy exchange, electron-hole pairs and excitons, and exciton-polaritons. I also describe the materials studied in this research, providing a review of the literature on this field, including the latest results reported on control over exciton-polaritons in 2-dimensional semiconductor materials. Chapter 3 is dedicated to a description of the experimental methods used in this research. A detailed description of the tuneable microcavity setup is given, and supported with theoretical calculations described in more detail in Chapter 4.

Chapter 4 is dedicated to describing the theoretical modelling of exciton-polaritons used to analyse the experimental results. Computer codes to simulate the optics of multilayer structures included in this chapter, are provided in the Appendix. In this chapter I also discuss three different criteria for describing the transition from weak to strong coupling regimes.

Chapter 5 is dedicated to one of the main results of this research, which is the electrical control of exciton-polaritons in a 2-dimensional semiconductor

microcavity. Chapter 6 is another part of the research project where I describe the electrical control over the exciton energy exchange between two different semiconductor materials. In Chapter 7 I present two ideas for future research, the first one on the dependence of the electrical conductivity of 2-dimensional semiconductors on the coupling strength between excitons in the semiconductor and a confined light field, and the second one on valleytronics in 2-dimensional transition metal dichalcogenide semiconductors; specifically on the possibility of using a confined light field to allow for light polarisation properties to be transferred from one semiconductor material to a different one, which is spatially separated from the first one. Finally, Chapter 8 is dedicated to summarising this research to draw this thesis to a conclusion.

Chapter 2

Background

This chapter is dedicated to a description of the main concepts involved in this research project, using the literature available on light-matter interactions. This field has fascinated researchers for centuries; therefore, I commence the chapter with a concise historical overview of the study of light-matter interactions. Then, I briefly describe the fundamentals of hybrid light-matter particles to provide an understanding of the main parameters that have to be controlled in an experiment to observe this hybridisation. Such parameters are the energy-loss rate and the strength of the light field, which can be enhanced in devices that confine the light field. These devices have to be carefully structured to produce this enhancement and therefore, to support the formation of hybrid light-matter particles. In later sections, I focus the review on more recent literature concerning a type of light-matter particles, exciton-polaritons, that are the main focus in this research. For the description of exciton-polaritons, I briefly describe the properties of excitons in semiconductor materials, and then their ability to hybridise with a confined light field in a microcavity. At the end of the chapter, I present a review on the most recent literature on exciton-polaritons that use a family of two-dimensional semiconductors, the transition metal dichalcogenides, that are promising for future quantum technologies.

2.1 Light-matter interactions: historical overview

In this section, I give a concise historical overview of the study of light-matter interactions since the first written reports by pre-Socratic Greek philosophers until today. These pioneer philosophers understood the importance of describing nature as a whole using basic physical principles that were first described using highly elaborated artistic writing. Later, the need for mathematical tools arose accompanied by methodical observations that almost two thousand years later remain surprisingly accurate.

The interaction between light and matter has been the focus of intense research in the field of quantum optics, nanophotonics, photochemistry, and optoelectronics in the last few decades. However, the fundamental concepts used to describe this phenomenon have been under development since the fifth century BCE, in the first reported works by Democritus (460 - 370 BCE) and Empedocles (494 - 434 BCE), who understood that indivisible particles or atoms form matter. Empedocles, who also developed the cosmogenic theory of four elements (earth, water, air, and fire) forming all things that exist, derived the first theory of light and vision. He described the human vision as a perception of particles streamed out by our eyes that bounce back from things at an incredibly high but finite speed. Although this description of light and vision may sound entirely inaccurate in modern times, Empedocles, who was contemporary to Pitagoras and also influenced by his ideas, hinted at the first concepts involving light and geometry that later influenced Euclid [8]. Euclid (325 - 270 BCE) developed a complete set of axioms that he used to describe the motion of objects, including the propagation of light particles. He derived the laws of reflection based on a mathematical formula that previous Greek philosophers lacked [9]. Euclid's work influenced Ptolemy (~ 86 - 165 CE) who is best known for developing the geocentric theory of the solar system, but

he also wrote what is considered the most important scientific work on optics before Newton's Opticks (1704 CE). Based on Euclid's geometrical formulation of motion, Ptolemy derived the law of refraction of light and observed that the Earth's atmosphere refracts sunlight. He also documented a non-linear relationship between the angle of incidence and the angle of refraction in the water-air interface, and his measurements are surprisingly close to the results obtained by Snell's law of refraction [10].

The theory of vision involving light particles streamed out by our eyes lasted many centuries until Al-Haytham (965 - 1039 CE) overturned previous theories with new highly elaborate experiments using the camera obscura, or pinhole camera. Al-Haytham concluded that humans see sunlight reflected by objects, and he also understood light travelling at an incredibly high but finite speed, which depends on the propagation media [11]. Al-Haytham very well described many optical phenomena in his seven-volume *Book of Optics*, including a mathematical description of spherical aberration. Figure 2.1 shows an image included on the front page of the Latin version of the Book of Optics [12], depicting different optical phenomena like rainbows, the reflection of sunlight, and refraction in water. Although Al-Haytham is considered by many historians as the first proponent of the modern scientific method [11], it was not until Newton's Opticks [14] that the scientific knowledge of light was truly revolutionised. Contemporary to Isaac Newton (1643 - 1727) who developed a complete theory of ray optics, Robert Hooke (1635 - 1703) and Christiaan Huygens (1629 - 1695) developed a wave theory of light that contrasted many claims made by Newton in his corpuscle theory of light [15, 16]. Hooke and Huygens hypothesised that light oscillates perpendicular to the propagation direction and that a medium of propagation is needed for light waves to propagate in a manner similar to sound waves propagating in the air. They were referring

FIGURE 2.1: Image on the front page of the Latin version of Al-Haytham's Thesaurus Optica (*Book of Optics*)[13].

to the ether as proposed by Descartes. Despite this controversy between the wave theory and the particle theory of light, Newton's ray optics was highly influential for the development of technology in many areas of science, for example in astronomy. After Newton's description of the aberration of light passing through lenses, he proposed a design for a reflecting telescope that helped to improve astronomical observations.

Many scientists since Newton's Opticks made essential advances in the field of optics; however, it is not my intention to summarise all of their contributions to the field for it would require many pages. Instead I would like to focus this story on what is more applicable to the concepts used in my research, starting from Maxwell's description of light-matter interactions and proceeding to "The strange theory of light and matter", as Richard Feynman called it [17].

Based on Faraday's experiments on electromagnetism, James Clerck Maxwell

(1831 - 1879) proposed a complete set of mathematical formulae that describe an interconnection between the electric and magnetic fields and the properties of matter, such as matter's susceptibility to respond to the action of the fields. However, Maxwell did not recognise the electromagnetic nature of light until he observed that light and an electromagnetic wave travel at the same speed [18]. Influenced by the notion that light, sound, and heat need a propagation medium, and combining this with the knowledge that there exists an electromagnetic field surrounding bodies, Maxwell in some way described ether as an electromagnetic field. In his paper published in 1865 he wrote [18]:

We have therefore some reason to believe, from the phenomena of light and heat, that there is an ethereal medium filling space and permeating bodies...

Maxwell thought that the electromagnetic field is that ethereal medium filling space, which allows for light to propagate between and through bodies. This assumption led him to imagine the following idea to prove that light is an electromagnetic wave: he supposed that there is an electromagnetic plane wave propagating through the electromagnetic field, and he assigned a velocity v to this plane wave. Using calculations with his theory of electromagnetism and with experimental values of a dielectric medium, he obtained an experimental value of the velocity v that is very close to the experimental values of the speed of light reported by others, so he concluded that the propagating electromagnetic plane wave must be light.

The implications of Maxwell's electromagnetic theory of light are enormous. For the very first time in the history of light and matter interactions there was an excellent understanding of how light and matter can interact, and it is through the electromagnetic nature of light, and the susceptibility of matter to be affected by an electromagnetic field. The electromagnetic theory of light opened up vast possibilities for new explorations using the idea of light as an

electromagnetic wave that propagates through bodies and space. However, the idea of an ether persisted and needed a more accurate explanation. If there was, in fact, an elastic ethereal medium allowing for light propagation through space, it had to oscillate at the same frequency as the transverse oscillations of the electromagnetic field of light This means that the matter which ether is made of had to be incredibly rigid, which makes no sense at all. On the other hand, Maxwell assumed bodies as pure solid forms of matter, however, contemporary to Maxwell, there was an essential development of the laws of thermodynamics that provided essential tools for a better understanding of matter. Thermodynamicists such as Josiah Willard Gibbs (1839 - 1903) understood that energy propagates through a 'sea' of matter with properties dependent on its temperature, and this notion soon had to be contrasted with the electromagnetic theory of light.

In other words, scientists very quickly approached the limits of classical mechanics, which are reached when one considers that matter is formed by atoms and molecules, and that an electromagnetic field modifies the properties of matter from its tiny constituents.

From 1879 to 1896 J. Stefan, L. Boltzmann, and W. Wien made essential observations on the radiation of bodies that absorb all electromagnetic energy, called black body radiation. They found a relationship between the energy of the radiation of the black body and its temperature [19–21]. Boltzmann derived Stefan's law of radiation (which depends on the temperature of the black body) using the second law of thermodynamics. Wien found that the maximum energy of the black body radiation spectrum shifts to shorter wavelengths at higher temperatures. However, his calculations disagreed with experiments at long wavelengths. Although these laws provided significant advances to understanding the electromagnetic radiation of black bodies, and explained

why the sun is yellow, it lacked accuracy when compared with experimental observations. Lord Rayleigh (1842 - 1919) tried to correct Wien's law proposing a new law that agrees well with experimental observations for long wavelengths ($> 3\ \mu$m) but completely disagrees with experiments at ultraviolet wavelengths. This disagreement between theory and experiments is historically known as the ultraviolet catastrophe. The inability of scientists to explain the experimental results of black body radiation over the whole electromagnetic spectrum led Max Planck (1858 - 1947) to find a breakthrough that changed our perception of the world completely. In 1900, Planck proposed a heuristically developed mathematical formula that reproduces with high accuracy the experimental black body radiation spectrum [22]. However, more important than the mathematical formula was his derivation of a theory of the physics behind the formula that he proposed six years later. To explain his formula, Planck proposed a theoretical system in perfect thermodynamic equilibrium consisting of a cavity with perfectly reflective interior walls. Units of frequency are placed inside of this cavity. These units of frequency represent a discrete set of frequencies that a black body can radiate. Moreover, there is a particular number n of each of the units of frequency ν, so the energy of the units of one particular frequency is $E_n = nh\nu$, where h is now known as Planck's constant [23]. The whole number of units of frequency at all frequencies constitute the body that radiates in the cavity. These units of frequency represent quanta of energy, and Planck explained that there is no need for these particles to exist, and still from a theoretical point of view they do explain the black body radiation spectrum.

Although this is a purely theoretical notion of quanta of energy, these new theoretical particles allowed scientists to explain many physical phenomena that classical mechanics failed to explain, especially those phenomena that contrasted thermodynamics with the electromagnetic theory of light. However,

contemporary to Planck, other experiments revealed that quanta of energy do exist.

In 1900, Heinrich Hertz and his student Philipp Lenard observed that the recently discovered electrons (J.J. Thompson, 1887), responsible for the electrical current, change their flux when light illuminates the electrical conductor. Einstein in 1905 explained this as a momentum conservation effect when the particles of light crash against electrons in the electrical conductor. Electrons are then ejected from the conductor when the energy of light is greater than the particular threshold energy of the conductor known as the work function. This explanation is known as the photoelectric effect [24], and essential for this description is that light is considered as tiny particles, quanta of light named photons. The wave theory of light can not explain the photoelectric effect.

All of these observations led scientists to develop an accurate description of the quanta of energy which had to be explained by both the particle theory and the wave theory of light. Many famous scientists contributed to the development of this theory that we know as quantum mechanics. A significant breakthrough was the hypothesis by Louis de Broglie in 1927, when he proposed that not only light behaves as waves or as particles depending on the experimental conditions, but actually any particle with momentum p has a wavelength λ associated with it through a straightforward relation, which is $p = h/\lambda$, where h is Planck's constant.

Since Maxwell's electromagnetic theory of light, scientists have known about quanta of light, or photons, that today are very well understood to the extent that engineers are able to use them for technological applications, for example in transistors that emit light at particular visible wavelengths: millions of these transistors form screens in televisions, laptops, and mobile phones.

Since the development of quantum mechanics, scientists have looked back to Maxwell's electromagnetic theory of light to see whether Maxwell's equations needed revision. This led scientists to the development of the quantum theory of light-matter interactions. Probably one of the most famous scientists that contributed to this theory was Richard Feynman (1918 - 1988) who called this theory 'the strange theory of light and matter interactions'. However strange this theory may be, it led scientists to explore further the quantum description of light-matter interactions. They started asking questions about, for example, how to make two photons interact with each other if we understand an 'interaction' as an exchange of information, which could be energy. If we think of photons as waves, whenever two photons (or two streams of photons) meet each other, a superposition occurs that makes them coexist in a particular point in space, and they do not exchange their energy, at least in a first approximation. A small portion of their energy can be exchanged through non-linear interactions, however, this exchange is too weak to be used for real-life applications. For this reason lightsabers cannot exist in the way George Lucas imagined them for his Star Wars films. However, what if we provide photons with some of the properties of matter? In other words, how can we create a hybrid light-matter particle? We know that two particles of matter exchange their energy when crashing against each other. If these two particles have some volume and elasticity, they can produce a deformation on each other if their initial energy before the collision is large enough. Providing photons with properties of matter could, in principle, allow them to exchange energy through mechanical interactions. For different conditions they could probably coexist through a superposition due to their wave-like nature. So what conditions are these, and how can we manipulate them? Scientists were successful in creating hybrid light-matter particles a few decades ago, which I will describe more technically in the next section. However, to explore more deeply the ideas

of manipulation and control of hybrid light-matter particles, and to produce results applicable to real life, science still needs to develop new theories based on experimental observations. Also, important advances have been made in the field of non-linear interactions, and it has been found that indeed, hybrid light-matter particles exchange their energy more strongly than bare photons. However, we need to explore further the fundamental physics of controlling light-matter interactions, and what the reader will find in this thesis is an essential contribution to this exploration. In my research, I have successfully provided photons with properties of matter, and I have studied a way to turn this provision on and off as desired. However big or small this contribution may seem, science advances through thousands of important steps before any breakthrough occurs, and no one can predict when it will happen.

It has been more than two thousand years since Ptolemy's methodical experimental research on light and matter interactions, and there are still many physical phenomena that we do not entirely understand. Especially the phenomena occurring at the nanoscale, which can be well approached by the quantum description of light and matter interactions, or Quantum Electrodynamics (QED) as it is best known. It is not my intention to give an in-depth background of QED in this thesis, but instead to provide a classical or semi-classical description of some physical concepts involved in the interaction between light and matter at the nanoscale, for example the concept of energy exchange between an emitter and a confined light field. However, I make use of concepts of the QED to describe experimental observations that I will define whenever it is necessary.

2.2 Hybrid light-matter particles

2.2.1 Light field confinement

Hybrid light-matter particles are formed when an efficient energy exchange between an electromagnetic field and a particle susceptible to the field occurs. The energy exchange is efficient when the rate at which the energy is transferred backwards and forwards between the two constituents is larger than the rate at which the total energy of the system is dissipated. To have an efficient energy exchange it is necessary to provide the light-matter system with favourable conditions. Two conditions of high importance are: first, to have a confined electromagnetic field in a small volume V, and second, to have a system with low energy-loss rate. The first condition is met in strongly localised fields in a structured array of materials, i.e. optical microcavities, plasmonic arrays, photonic cavities, dielectric spheres, and plasmonic nanoparticles (among others). These structures have lengths often of subwavelength size. The other necessary condition for an efficient energy exchange is a controlled low energy-loss rate, which is experimentally characterised by the quality factor Q; high-quality factor means low energy-loss rate.

The quality factor and the volume of the field confinement are, in principle, unrelated quantities, i.e. they can be controlled independently when designing a confinement device. However, in an experiment for the hybridisation of the confined light field with an absorber, the quality factor Q and the confinement volume V become inversely proportional. This challenges the realisation of highly confined fields in small volumes with low energy-loss rates. For example, plasmonic nanoparticles provide a small volume V for the field confinement and a significant energy-loss rate. On the other hand, photonic crystals can reach high-quality factors but at large volumes of the field confinement. Microcavities

are considered to reach moderate-quality factors and relatively small volumes of the field confinement.

The electromagnetic field associated with a light beam has an oscillatory nature, i.e. the intensity of the field oscillates as it propagates through the vacuum or materials. One way to confine the electromagnetic field in some structured device is to make use of the ability of the electromagnetic field to resonate or to interfere constructively with itself in a structured device. To study the resonance of an electromagnetic field in a structured device, we can start by considering the propagation of electromagnetic waves in one dimension of space (this can be extended to three dimensions), and we can describe the fields as a plane wave by the mathematical formulae

$$\begin{aligned} \vec{E}(x,t) &= \vec{E}_0\, e^{-i(\vec{k}\cdot\vec{x}-\omega t)}, \\ \vec{B}(x,t) &= \vec{B}_0\, e^{-i(\vec{k}\cdot\vec{x}-\omega t)}, \end{aligned} \tag{2.1}$$

where $\vec{E}$ and $\vec{B}$ are the electric and magnetic components of the light field, with amplitude maxima being $|\vec{E}_0|$ and $|\vec{B}_0|$. $\vec{k}$ is the wave-vector, ω the frequency of the oscillations, and $\vec{x}, t$ are the position and time variables. These functions are solutions of Maxwell's equations in free space. When describing the electromagnetic wave propagation in matter, material properties are introduced. These also introduce an attenuation factor that decreases the intensity of the electromagnetic field as it propagates through the material. This attenuation factor is interpreted as an energy-loss factor. The material property introduced is the permittivity ε that has a complex component responsible for the energy loss. When these properties are introduced, the wave-vector, which depends on the permittivity through a dispersion relation, becomes a complex number as well. The complex component accounts for the energy loss in the material. In a

lossy media, the fields described in equation 2.1 become

$$\begin{aligned} \vec{E}(x,t) &= \vec{E}_0\, e^{i\omega t} e^{-\gamma|\vec{x}|}, \\ \vec{B}(x,t) &= \vec{B}_0\, e^{i\omega t} e^{-\gamma|\vec{x}|}, \end{aligned} \tag{2.2}$$

where $\gamma = \alpha + i\beta$ depends on the complex permittivity $\varepsilon = \varepsilon' + i\varepsilon''$ of the lossy media as follows:

$$\begin{aligned} \alpha^2 &= \omega^2 \frac{\mu\varepsilon'}{2} \left(\sqrt{1 + \left(\frac{\varepsilon''}{\varepsilon'}\right)^2} - 1 \right), \\ \beta^2 &= \omega^2 \frac{\mu\varepsilon'}{2} \left(\sqrt{1 + \left(\frac{\varepsilon''}{\varepsilon'}\right)^2} + 1 \right), \end{aligned} \tag{2.3}$$

where μ is the magnetic permeability. In equation 2.2 there is an oscillatory component of the field with frequency ω and there is an attenuation factor γ which accounts for the energy loss as waves propagate through the material. To confine the fields in a small volume, we need to make use of the harmonic component with frequency ω; we need to design a device that confines the fields through resonance. Additionally, we need to choose materials with a low loss factor γ, which means that we need to carefully look at the complex permittivity of the materials we choose for the design of the device.

In summary, for the realisation of hybrid light-matter particles, we need a confined light field and particles that can exchange energy with the field in an efficient way. A light field can be confined through resonance in a structured device specially designed for the confinement. Two important parameters to consider for efficient light confinement are the quality factor Q and the volume of the confinement V. Moreover, in a light-matter interaction experiment, these two parameters become inversely proportional.

2.2.2 Energy exchange

In the previous subsection, it is stated that light field confinement is necessary for efficient energy exchange between light and matter to form a hybrid light-matter particle. In this subsection, I describe some particles with properties of matter that can form hybrid light-matter particles by exchanging energy with a confined light field.

Particles with the properties of matter needed for the formation of a hybrid light-matter particle would be able to exchange energy with a confined light field if they enter a resonant regime. This resonant regime is usually achieved in a narrow spectrum of frequencies; how narrow the spectrum is, relates to the energy-loss factor. So, to enter a resonant regime and to exchange energy with a confined light field, matter particles need to be susceptible to the light field for a particular resonant frequency ω_0.

To mention an example where this occurs we can consider molecular vibrations. Molecular vibrations have particular frequencies associated with them. Carbon-oxygen double bonds (C=O) in a molecular compound called Poly(Methyl Methacrylate) (PMMA), have a vibrational frequency of ~1730 cm^{-1}. These molecules absorb light through the excitation of the molecular vibrations, and then the energy is dissipated through thermal diffusion. However, as I mentioned before, for the formation of a hybrid light-matter particle we need the energy to flow back to the light field before it dissipates. Also, a confined light field is needed for an efficient energy exchange.

K. Menghrajani *et al* recently reported the formation of hybrid light-matter particles in a device that combines a confined light field in an optical microcavity with PMMA molecules [25] to form vibro-polaritons, a hybrid state formed between molecular vibrations and a confined light field. Moreover, multiple

molecular vibrations of the same molecular species entered a resonant regime with the confined light field with an efficient energy exchange, i.e. hybrid light-matter particles were formed. This hybridisation was achieved with confined light fields in a microcavity as well as in a plasmonic array.

To illustrate the process, let us consider Figure 2.2 which shows an optical microcavity made of two semitransparent mirrors which confine a light field represented by the red sinusoidal line. This light field has a particular frequency ω_0 that depends on the separation between the mirrors. Inside the cavity, there are PMMA molecules that support many different vibrational modes, but one particular mode, the C=O, has a vibrational frequency very similar to the frequency of the light field (or even the same frequency). These similar frequencies allow for the C=O vibrational modes and the light field to enter a resonant regime. In this resonant regime, PMMA molecules absorb the light field through the excitation of C=O molecular vibrations, and then the energy is released back to the light field. The electron clouds surrounding atoms mediate this absorption and release of electromagnetic energy. Electron clouds are formed by electric charges that react to the presence of the confined light field producing a charge displacement followed by a displacement of the atom nuclei. This displacement is oscillatory with a particular frequency ω_0' very similar to the frequency of the confined light field. The collective displacement of the electric charges also produces an electromagnetic field around them, that is confined in the microcavity as well.

In summary, the electromagnetic energy confined in the microcavity device excites C=O molecular vibrations when they have very similar frequencies (or the same frequency), and these vibrations generate an electromagnetic field around the molecules which is also confined in the microcavity. All this electromagnetic energy exchange is faster than any thermal dissipation

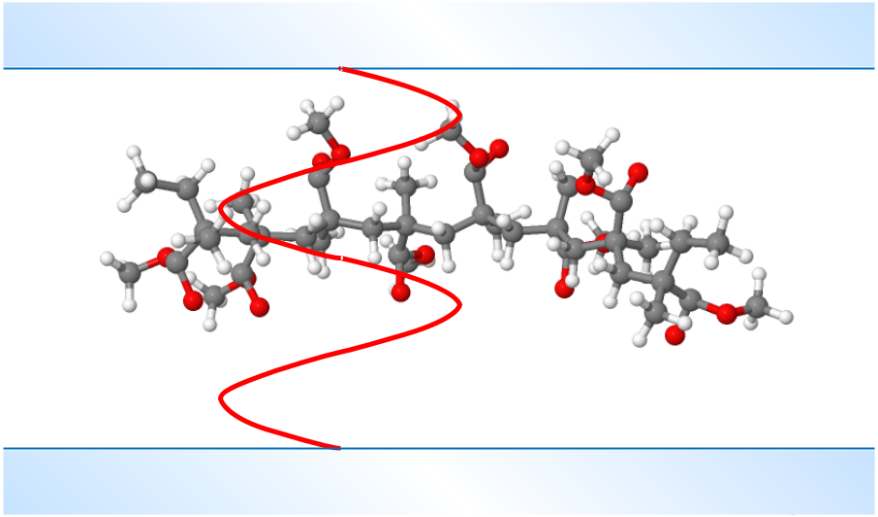

FIGURE 2.2: Optical microcavity filled with PMMA. The microcavity confines a light field represented by the red sinusoidal line. C=O bonds in PMMA molecules exchange energy with the confined field through molecular vibrations to form a type of hybrid light-matter particles called vibro-polaritons.

of molecular vibrations due to the low energy-loss factor of the confined light field in the microcavity, and also of the PMMA material, which has low thermal diffusion.

2.3 Electron-hole pairs and excitons

In this section, I describe the absorption of light by excitonic materials to understand how they form exciton-polaritons, which I will describe in the following subsection. I will focus this description on semiconductor materials. I also briefly describe here experimental techniques to measure excitons supported by different materials.

2.3.1 Energy bandgap and photon absorption

Excitons are particles formed by a bound electron-hole pair in materials that exhibit bandgaps in their electronic band structure [26]. The formation of an

electron-hole pair is mediated by photon absorption. Materials with bandgaps are referred to as semiconductors, as often their Fermi energy is higher than the energy of the lower band. The lower band is entirely populated with electrons while the upper band is empty. The semiconductor material cannot conduct electricity unless electrons populate the upper band.

To briefly describe the formation of bandgaps in a semiconductor let us consider the hydrogen-like model of electronic states. This model describes the electrons in the hydrogen atom as having a discrete set of energy levels that they can populate. A heavier atom can be described as an ionic core that comprises all bound electrons and the atom nucleus, surrounded by unbound or free electrons. This heavier atom is a hydrogen-like atom, where the difference from the hydrogen atom lies in the mass of the ionic core compared to the hydrogen nucleus. Electrons surrounding the ionic core are mainly responsible for the electronic properties of these atoms, and for their properties in a crystalline array of these atoms, i.e. metallic, insulating, or semiconducting properties. In a one dimensional chain of atoms, for example, electrons can propagate as Bloch waves, where each atom in the chain is described as a potential well separated from each other by a distance a. Electron waves have the same periodicity as the chain of atoms, and as the potential wells. In reciprocal space, these electron waves form a discrete set of electronic bands with periodicity π/a. At each position of this reciprocal periodicity, there is a superposition of adjacent electronic bands. If this superposition is destructive, a bandgap is formed, producing the semiconducting properties of the chain of atoms. If no bandgap is formed, the chain of atoms has metallic properties.

In a crystalline system, the first Brillouin zone has symmetry elements depending on the symmetry of the atomic array in the material. Having a crystalline structure forming the material allows us to describe the electronic states

only using one crystalline unit. Let us observe an illustration of the formation of energy bandgaps in a crystalline system that consists of a chain of atoms. Figure 2.3(a) shows a schematic plot of the first energy state of free electrons in one dimension, and (b) shows the energy diagram of electrons in a crystalline material where an energy bandgap is formed. The upper and lower bands in a

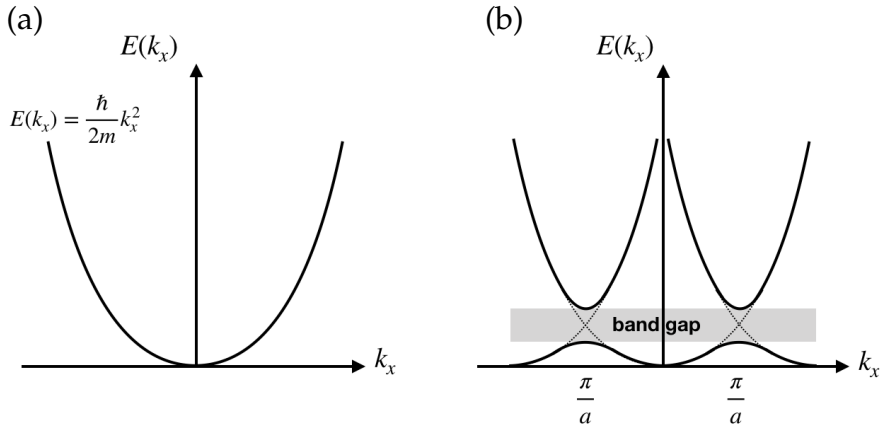

FIGURE 2.3: (a) Energy of the first state of free electrons. (b) Linear combination of the first energy states of atoms separated by a distance a, where an energy bandgap is formed at the reciprocal positions π/a.

semiconductor material are called conduction and valence bands respectively. The energy bandgap is the energy difference between the upper band minimum and the lower band maximum, often referred to as band edges, with energies E_C and E_V respectively.

In an electrically neutral semiconductor material, electrons fill the valence band, while the conduction band remains empty. In this condition, the Fermi energy E_F is in between the band edges. To produce an electric current in the semiconductor material it is necessary to populate the conduction band with electrons. One way to do this is to provide an electron in the valence band with enough energy to 'jump' to the conduction band, which can be achieved by photon absorption. This electronic transition is only possible if

the photon energy $\hbar\omega$ is larger than the energy bandgap E_g ($\hbar\omega > E_g$) where $E_g = |E_C - E_V|$.

The absorption coefficient of photons, α, mediated by electronic transitions from the lower to the upper band in the semiconductor is proportional to the square root of the difference between the energy of photons and the energy bandgap: $\alpha \propto \sqrt{\hbar\omega - E_g}$ [26]. Figure 2.4 shows an illustration of the dependence of the absorption coefficient on the photon energy. Different phenomena

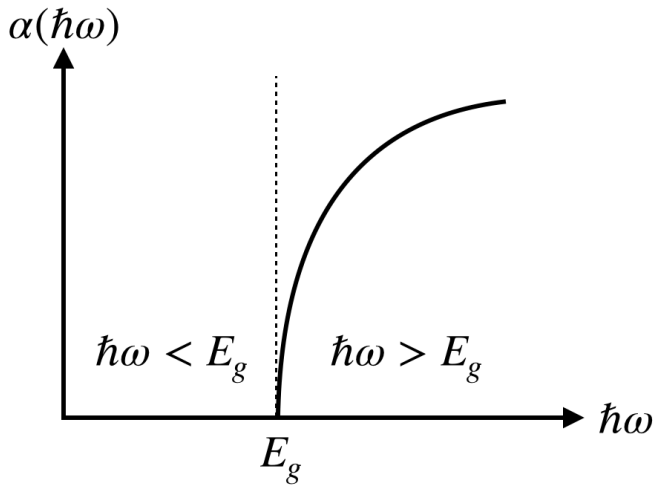

FIGURE 2.4: Absorption coefficient as a function of the photon energy $\hbar\omega$. Absorption mediated by electronic transitions is only possible if the energy of absorbed photons is larger than the energy gap.

can modify the absorption coefficient shown in Figure 2.4 in real semiconductors; there may be temperature effects that produce a blue shift in the minimum of absorption, and there may also be indirect transitions mediated by phonon absorption.

Photon absorption can produce an electronic transition from the valence band to the conduction band when the photon energy is equal to or larger than the energy bandgap. When the electronic transition occurs, the valence band lacks an electron, which is called a hole with a positive charge, forming an electron-hole pair. In this description no interaction between the electron

and the hole is considered to happen, however, due to their opposite charge, they can attract each other in a Coulomb-type interaction, forming a bound electron-hole pair, or exciton.

2.3.2 Excitons

Excitons are Coulomb bound electron-hole pairs that can be excited through photon absorption. When we consider this Coulomb interaction, the absorption coefficient is enhanced for a narrow spectrum of photon energies, which is observed as peaks of absorption. From this point on, I will focus the description of electronic transitions only on those producing excitons, i.e. when the electron-hole pair generated by photon absorption remains bound by Coulomb attraction.

Figure 2.5 shows the band diagram at the band edges to describe the excitation of excitons through photon absorption. In Figure 2.5(a) an electron at the lower band edge (blue circle) absorbs a photon of energy $\hbar\omega$; this photon energy is enough to produce an electronic transition from the lower band to the upper band, where the energy of the gap at the band edges is E_g. In Figure 2.5(b) the electron stays at the upper band edge, leaving a positive hole (empty blue circle) in the lower band edge. This electron-hole pair remains bound by Coulomb attraction due to the opposite charges. Figure 2.5(c) shows that after a short period the electron decays to the lower band, releasing its energy generating a photon of energy $\hbar\omega$. In this simple description, it is considered that the incident photon, the energy gap at the band edges, and the released photon have the same energy. However, in real semiconductor materials, these energies differ; their difference depends on the physical properties of the materials.

In a more complex crystalline system (i.e. different atoms in the one-dimensional chain) the electronic band structure may form local and global upper(lower)

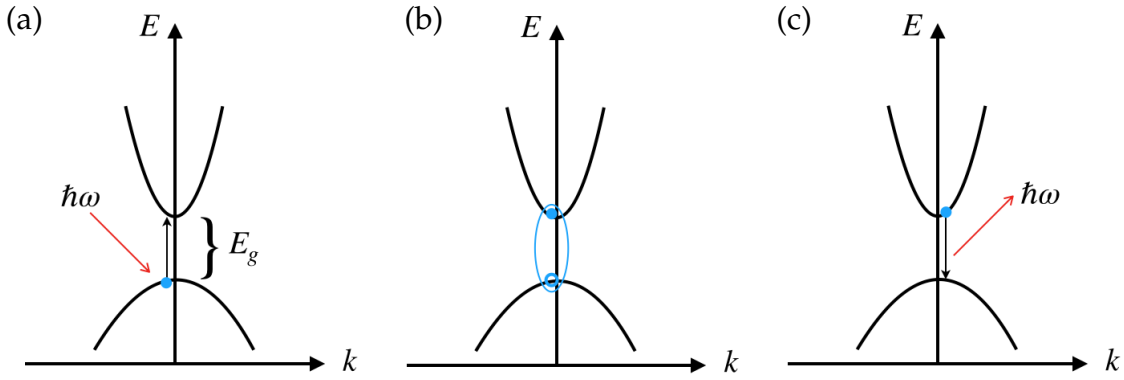

FIGURE 2.5: Energy diagram at the band edges of Figure 2.3 (b). In (a) an electron at the valence band edge absorbs a photon, and 'jumps' to the conduction band edge. In (b) an electron-hole pair is formed. In (c) the electron decays to the valence band releasing a photon.

band minima (maxima) in reciprocal space, which modifies the process for electronic transitions mediated by photon absorption. Figure 2.6 (a) shows the schematic energy gap at the band edges where an exciton is formed, as in Figure 2.5(b). This process for the generation of an exciton is a direct transition of electrons, where momentum conservation depends only on the momentum of photons and excitons: there is no horizontal component in the wave-vector for the transition. In Figure 2.6 (b) however, there is a local minimum and a global minimum in the upper band; the latter is located at a different point in reciprocal space. In this case, the excitation of an exciton through photon absorption involves two processes, and is called an indirect transition. First, a photon of energy $\hbar\omega$ excites the electron to an energy state higher than the upper band at a wave-vector corresponding to the position of the local upper band minimum, the electron then relaxes (through a non-radiative process) to the local upper band minimum, which has an energy higher than the global upper band minimum in an amount $\hbar\Omega$. This energy difference between the local and the global upper band minimum, produces the second process that consists of a relaxation by the energy difference, which generates a phonon of energy $\hbar\Omega$ in the crystal. When the electron releases the energy difference,

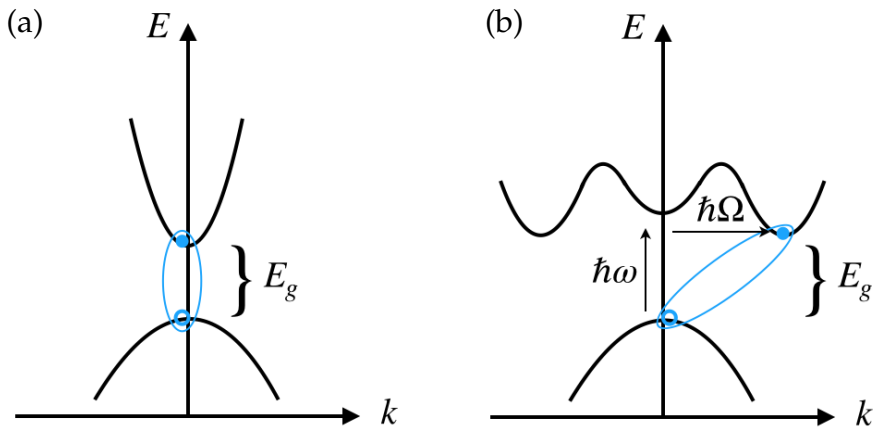

FIGURE 2.6: (a) Energy diagram at the valley point as shown in Figure 2.3(b) where an exciton is generated through a direct transition of an electron from the lower to the upper band. (b) Energy diagram of a different material, where an exciton is generated through an indirect transition of an electron from the lower to the upper band, which involves a low energy relaxation through the generation of a phonon in the crystal.

it reaches the global minimum of the upper band to form the exciton. One important condition to excite an exciton is that the electron and the hole should have the same group velocity in order to remain bound. The group velocity of electrons and holes is proportional to the slope of the energy bands at the different values of k. As we can observe in the energy diagrams shown in Figures 2.5 and 2.6 the slope is zero at the band edges, for the same value of k, so electrons in the upper band edge, and holes in the lower band edge, have the same zero group velocity; therefore they can remain bound to form an exciton. In a semiconductor material with a more complex band structure, however, this condition may be satisfied at different values of k, giving rise to more exciton transitions that have different energies.

To elucidate more about this we can describe a Coulomb bound electron-hole pair using the Bohr model as in the Hydrogen atom, where the hole and electron now replace the proton and electron of the Hydrogen atom. Similarly to the Hydrogen atom, in an exciton there is a discrete set of energies that depends on

the principal quantum number n,

$$E(n) = -\frac{R_X}{n^2},$$

where R_X is the exciton-Rydberg energy. The radius of the electron-hole pair also depends on the principal quantum number n,

$$r(n) = n^2 a_X,$$

where a_X is the exciton-Bohr radius. The exciton-Rydberg energy and the exciton-Bohr radius are directly proportional to their Hydrogen counterparts.

If we combine this discrete set of energy levels for excitons with the condition of electrons and holes having the same group velocity for the formation of an exciton (which happens at the band edges), then the energy of the exciton transitions are expected to occur close to the energy bandgap. Moreover, the set of energies E_n of excitons is the difference between the energy gap E_g, and the Coulomb attraction E_C,

$$E_n = E_g - E_C,$$

where $E_C = R_X/n^2$. Also, the Coulomb attraction enhances the photon absorption, so the absorption peaks of the different exciton energy levels are expected to be much larger than the absorption of unbound electron-hole pairs. This is illustrated in Figure 2.7, where we also observe that the lower order exciton energy transitions have larger absorption, which is due to a larger probability of transition.

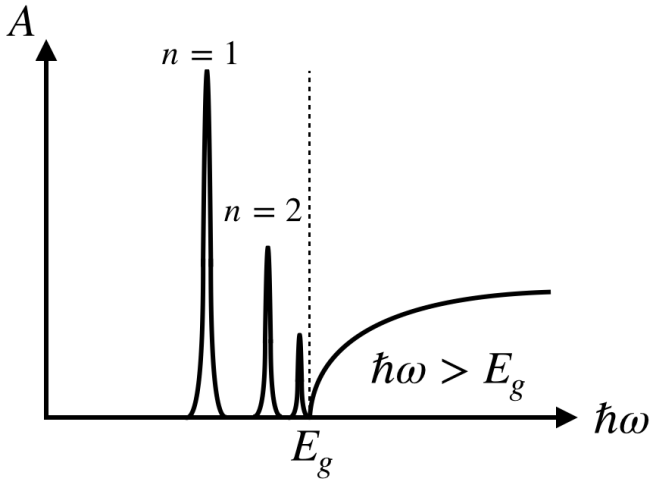

FIGURE 2.7: Absorption spectrum of a hypothetical semiconductor material that supports the excitation of excitons and unbound electron-hole pairs. Excitons have a discrete set of energy levels similar to the hydrogen atom, and the absorption of these levels is much greater than that of unbound electron-hole pairs (not to scale).

2.3.3 Optical detection of excitons

To detect excitons, either direct or indirect, we can illuminate the material with white light, which has a continuum of photon energies, and we can measure the portion of light that is absorbed by the crystalline material to generate excitons. Figure 2.8 shows a confocal optical setup for reflectance R, and transmittance T measurements, from which the absorbance can be obtained by $A = 100\% - R - T$. In this system, the white light source is collimated and focused on the sample from the illumination side (left side of the sample). A semi-transparent mirror is used to collect the light reflected by the sample. On the right side of the sample another lens collects transmitted light, which is focused on the transmission detector. On this side a second semi-transparent mirror is used to produce an image of the sample on a camera.

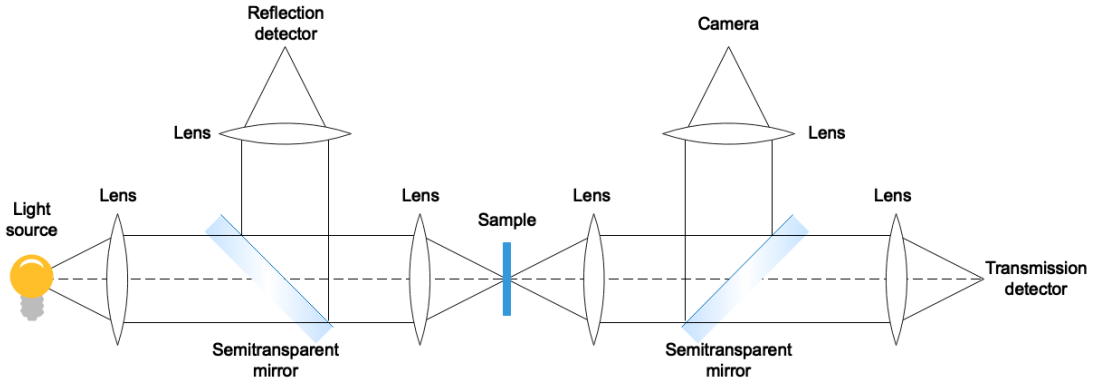

FIGURE 2.8: Confocal optical setup for white light reflection, transmission, and absorption measurements.

2.4 Exciton-polaritons

Exciton-polaritons are a type of hybrid light-matter particles formed through an efficient energy exchange between excitons and a confined light field. As mentioned in Section 2.2.1 materials for an effective energy exchange need to have a low energy-loss rate. In the case of excitonic materials, the energy-loss rate is related to the width of the absorption peak of the exciton transitions; the lower the energy-loss rate, the smaller the peak width. For this reason the effective energy exchange between a confined light field and unbound electron-hole pair is not possible, as their absorption peaks are too broad in spectral range. However, excitons often exhibit a narrow peak in the absorption spectrum, as illustrated in Figure 2.7. Therefore excitons are suitable particles for effective energy exchange with a confined light field, with low energy-loss rate, to form exciton-polaritons.

As well as vibro-polaritons described before, exciton-polaritons can be formed in optical microcavities and plasmonic arrays (among other light field confinement devices). A type of optical microcavity, the Fabry-Pérot microcavity, is composed of two semitransparent mirrors [27]. In between the mirrors the light field forms a confined standing light-wave, whose wavelength λ_m

depends on the separation between the mirrors, or the cavity length, L_c. If we consider the mirrors to be perfect reflectors (no penetration of the light field into the mirrors), the standing waves have nodes at the inner edges of the mirrors.

This relationship between the cavity length L_c and the set of wavelengths of the confined field is

$$L_c = m\frac{\lambda_m}{2n}, \tag{2.4}$$

where n is the refractive index of the dielectric medium between the cavity mirrors ($n = 1$ for air and vacuum), and m is an integer number that indicates the cavity mode number. Therefore the confined light field is composed of an infinite and discrete number of wavelengths that fulfil condition 2.4, where the cavity mode with the lowest energy is associated with the largest wavelength. Four different cavity modes are illustrated in Figure 2.9, where the wave-vector of the light is considered to have only a vertical component, normal to the surface of the microcavity mirrors. In this figure we can also observe that the confined light field is stronger, or more intense, at the antinode of the standing waves; for the fundamental mode ($m = 1$), this occurs at the centre of the microcavity [28].

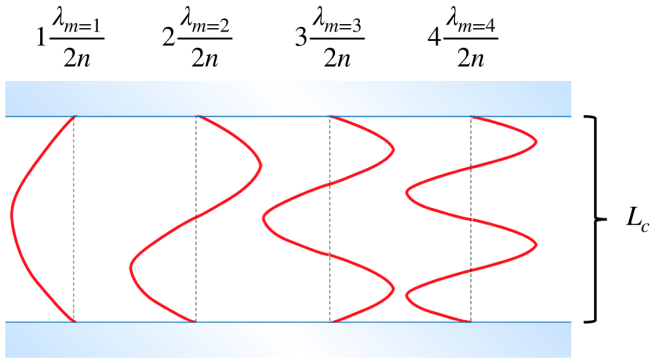

FIGURE 2.9: Schematic figure of a Fabry-Pérot microcavity identifying the cavity length L_c and the first four different modes of different wavelengths confined between the semitransparent mirrors. The wave-vector of the light is considered to have only a vertical component, normal to the surface of the microcavity mirrors.

Exciton-polaritons are formed through a dipole-dipole interaction between the dipole moment of excitons $\vec{d}$ and the electric field of the confined light field $\vec{E}$. The amplitude of the confined light field in the microcavity shown in Figure 2.9 oscillates horizontally, so the electric field associated with this light field has a horizontal vector component, parallel to the microcavity mirrors. To have a dipole interaction between excitons placed inside the microcavity and the confined light field, two conditions have to be met: first, the modulus of the electric field has to be non-zero (and ideally the largest), and second, the electric field has to be parallel to the dipole moment of the excitons. The coupling strength of exciton-polaritons is proportional to the product between the dipole moment of excitons $\vec{d}$ and the electric field $\vec{E}$ [28],

$$g \propto -\vec{d} \cdot \vec{E}. \tag{2.5}$$

If we consider the fundamental mode shown in Figure 2.9, the modulus of $\vec{E}$ is greatest in the middle of the microcavity, and so is the coupling strength of exciton-polaritons formed at that position according to Equation 2.5.

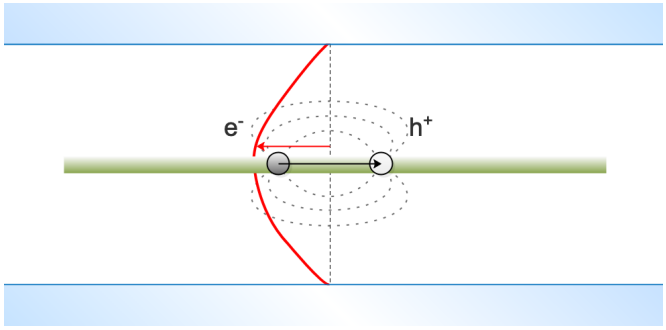

FIGURE 2.10: Schematic figure of a Fabry-Pérot microcavity where the confined light field (red line) interacts with an exciton through its dipole moment (black arrow).

Figure 2.10 illustrates the relative orientations of the light field vector (red arrow) and the dipole moment of an exciton (black arrow) supported by a semiconductor material which is thinner than the size of the exciton, so its dipole

moment is oriented in the plane of the semiconductor. The red line indicates the intensity of the fundamental mode of a confined field. The circles represent an electron e^- and a hole h^+ forming an exciton with dipole moment $\vec{d}$ indicated by the black arrow. Equipotential lines of the electric field surrounding the exciton are shown as dashed lines. This figure also illustrates the importance of positioning the excitons at the antinode of the confined field in the microcavity.

Whenever the confined light field in a microcavity, or cavity photons, enter a coupling regime with excitons embedded inside, new energy levels of the hybrid system (exciton-polaritons) are formed. Figure 2.11 shows an energy level diagram, where one cavity mode has the same energy as an exciton transition. When conditions for an efficient energy exchange are met, they form exciton-polaritons, which is observed as a splitting of the energy levels. The new energy levels of the hybrid system are called upper and lower exciton-polariton levels. The total separation of the upper and lower levels is $2g$. In the quantum mechanical description of the hybrid system $2g$ is related to the vacuum Rabi splitting, Ω_R, which corresponds to the rate at which excitons and cavity photons exchange their energy.

In Figure 2.11, the energy-loss factor of cavity photons γ_c and excitons γ_{ex} is neglected; however, in experimental observations, these factors are highly important. They determine the ability to observe a splitting of the energy levels. Also, the energy-loss factors limit the energy exchange rate, or the Rabi splitting. This leads to the definition of two regimes for the coupling between excitons and cavity photons: the strong and the weak coupling regimes. A detailed discussion on this topic is included in Chapter 4.

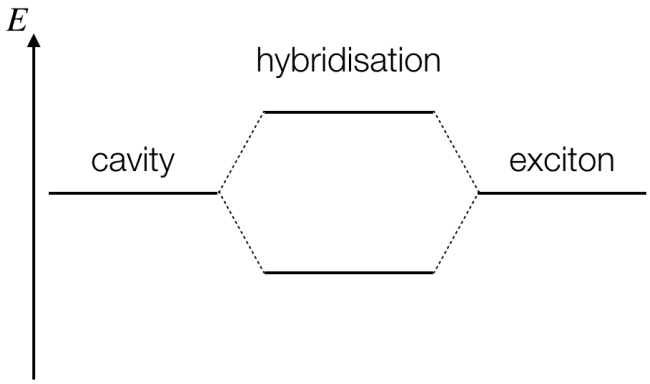

FIGURE 2.11: Energy levels in a hybrid system formed by cavity photons and excitons.

2.4.1 Number of particles for strong light-matter coupling

Since the first theoretical results reported by Pekar in 1958 [29], related to the excitation of excitons in crystalline systems by the action of an external electric field in vacuum, this topic has been widely investigated using both theoretical and experimental approaches. The theory developed by Pekar to describe light-matter interactions is, in principle, semi-classical, where an analytical function for the electric field is assumed to be known. Pekar expressed the exciton states by their polarisation dipole moment, which can be coupled to the external electromagnetic field in vacuum through a Schrödinger-like equation.

More general results were found by Jaynes and Cummings in 1963 [30]. The so-called Jaynes-Cummings model describes the interaction between an electric field and a two-level quantum system. Atoms and molecules can be modelled as two-level quantum systems. The two levels of the system correspond to the ground state and the first excited state, so the action of an electric field can excite the system from the lowest level, or ground state, to the highest, or the excited state. Jaynes and Cummings developed the quantum electrodynamic theory of the system and compared it with the semi-classical description, giving rise to the possibility of extracting material properties experimentally by using

both the quantum and the semi-classical formulation.

The fundamental difference between the Pekar and the Jaynes-Cummings models is that in Pekar's model, a crystalline system is excited by the action of an external electric field and the energy propagates through the system until eventually the energy is dissipated, i.e. the system is in the weak coupling regime. In the Jaynes-Cummings model the atom or molecule excited by the action of the external electric field can re-emit the energy by spontaneous emission and under certain conditions, the emission can feed the vacuum field back, and the same energy can be re-absorbed by the atom or molecule, i.e. the system is in the strong coupling regime. The Jaynes-Cummings model is still widely used to describe the experimental results of strong coupling.

The first experiments combining a confined light field and a two-level particle able to produce spontaneous emission led to important observations such as a modification of the spontaneous emission by the action of an external field. A two-level particle is a quantum system that remains in the ground state unless it is excited to a higher energy state. Excitons can be considered a two-level quantum system where in the ground state the electron is at the lower band of the semiconductor, and in the excited state the Coulomb bound electron-hole pair is formed through photon absorption. Spontaneous emission of excitons occurs when this particle decays from the excited state to the ground state, releasing energy as photons. The light matter interaction occurs when the two-level particle is in the excited state, and its energy is close to the energy of the light field.

The modification of the spontaneous emission of a two-level particle by the action of an external electric field was proposed by Purcell in 1946 [31, 32] for atoms placed in a microcavity. In this experiment the spontaneous emission of the excited particle can be enhanced when the frequency of the emission

matches the frequency of an external electric field confined in the microcavity. The magnitude of the enhancement, called the Purcell factor, is defined as

$$F_P = \frac{3}{4\pi^2}\frac{\lambda_c}{n}\frac{Q}{V},$$

where Q and V are the quality factor and the mode volume of the microcavity respectively.

The quality factor is defined as $Q = \frac{\omega_c}{\Delta\omega_c}$, where $\Delta\omega_c$ is the full width at half maximum (*fwhm*) of the resonant frequency ω_c of the microcavity which can be measured by transmission or reflection of white light. A high Q factor is required, at least on the order of hundreds, to observe the effects of the electric field on the spontaneous emission. However, the mode volume plays an important role as well. As the Purcell factor depends on Q/V, a low Q factor can be compensated by a small mode volume V. Important experimental observations of the Purcell effect were reported in the 1980s based on calculations by Kleppner in 1981 [33]. These calculations provided the basis of the experiments widely developed in those years. Goy *et al.* in 1983 reported the first observation of enhancement of the spontaneous emission rate in an experiment combining sodium (Na) atoms pumped into a circular microcavity [34]. These experiments were performed at low temperature, $T = 5K$, and operated at a resonant frequency close to 340 GHz.

Sanchez-Mondragon *et al.* reported in 1983 [35] the quantum formulation of the spontaneous emission of a two-level particle in a cavity with frequencies close together, near the resonant condition for the strong coupling regime. In this regime, the rate at which the two-level particle and the microcavity exchange energy through excitation and spontaneous emission is higher than the rate at which the whole system loses energy. The rate at which the system

exchanges energy is called the Rabi frequency Ω_R and (neglecting energy losses) is directly proportional to the coupling strength between the two-level system and the confined light field, $\hbar\Omega_R = 2g$. Sanchez-Mondragon also predict that the microcavity frequency ω_c splits in two, $\omega_\pm$, under the resonant condition, and the two new frequencies depend on the Rabi frequency as

$$\omega_\pm = \omega_c \pm \Omega_R/2.$$

The hybrid states with frequencies $\omega_\pm$ have energies $E_+ = \hbar\omega_+$ for the upper state, and $E_- = \hbar\omega_-$ for the lower one.

Later, in 1983 Kaluzny *et al.* [36] reported the observation of Rabi oscillations in a two-level system in a microcavity. They obtained experimentally the population of atoms in the upper state under the interaction with the microcavity for different numbers of atoms occupying the mode volume, which agrees well with the theoretical prediction that $\Omega_R \approx \sqrt{N}$. In this study it was observed that the number of particles in the upper state oscillates due to the continuous emission and re-absorption of the energy confined in the microcavity.

Haroche *et al.* in 1989 included in their conclusion an important comment [37]: 'theoretical predictions and observations were considered to this date as purely quantum effects, but as the Rabi frequency depends on the number of atoms, N, occupying the mode volume, eventually statistical fluctuations must lead to a macroscopic behaviour of the elements'. This means that classical effects should be observed under certain conditions, especially for a coherent behaviour and large values of N.

Raizen *et al.* reported in 1989 the observation of Rabi splitting in a microcavity with varying numbers of atoms occupying the mode volume, from N = 1 to N = 40 [38]. Such experiments were successful due to the high-quality factor Q,

which reached up to 26000. This proves that even with a small number of atoms, a high-quality factor can lead to remarkable observations that can eventually compensate for the effect of the temperature on the spectroscopic noise.

The controversy between the microscopic and the macroscopic descriptions, and observations, of hybrid light-matter states, or at what conditions the hybrid system behaves under purely quantum effects of classical effects, was elucidated by Zhu *et al.* in 1990 [39]. Zhu *et al.* reported the observation of Rabi splitting and these results were in excellent agreement with the entirely classical theory of beam interference. These results were carried out on large samples, with $N \approx 300$, and formed the basis for future experiments on large samples and allowed for the possibility of extracting experimental parameters using classical models.

As I mentioned before, the parameters ω_c, $\Delta\omega_c$, L_c, Q and V need to be carefully adjusted in an experiment, and now it should be clear that N also plays an essential role in the observation of the Rabi splitting under the strong coupling regime. The effects of the temperature seem to be suppressed by a coherent behaviour of the particles coupled to the confined light field and with a high-quality factor of the confining device. In 1992, Weisbuch *et al.* observed Rabi oscillations in a system which consists of a microcavity with a semiconductor film placed in between the cavity mirrors [40]. This differs from previous experiments where atoms were pumped into the microcavity either one at a time or as a continuous stream of atoms. In this study a thin semiconductor film of GaAs was placed in between the mirrors. This material supports the excitation of excitons through photon absorption. At certain conditions the photon emission frequency matches the microcavity resonant frequency, entering the strong coupling regime. These results set an important precedent for the design of devices with potential applications in microelectronics.

The realisation of microcavity exciton-polaritons by the experiments performed by Weisbuch *et al.* [40] led to important results reported by Houdré *et al.* in 1994 [41]. In this study, Rabi oscillations were observed through measurements of photoluminescence at a temperature of 77 K. These experiments make use of an improved microcavity made of distributed Bragg reflectors (DBR) which enhance the quality factor of the microcavity compared to simple semi-transparent metallic mirrors. The photoluminescence spectrum was measured for several angles of the incident beam, from which it is possible to extract the exciton-polariton dispersion relation.

From Houdre's experiments [41] is was found that slight variations of the microcavity size under the strong coupling regime with the semiconductor film lead to variations of the position of the anticrossing in the exciton-polariton dispersion curve with respect to the value of $k_{\|}$. However, the position of the semiconductor film inside the microcavity also plays an essential role in order to observe the Rabi splitting [42–44] due to the variation of the intensity of the confined light field in the cavity.

2.5 Materials for exciton-polaritons

2.5.1 Semiconductor quantum wells

Semiconductor quantum wells have been extensively used for the study of light-matter interactions. For some semiconductors, such as GaAs, GaN, and GaAl, among many others, the definition 'quantum well' arises from the property of these materials to confine excitons in a potential well with width comparable to the exciton Bohr radius. This potential well width can be well approximated by the thickness of the semiconductor, which can be fabricated by thermal evaporation methods. The confinement of excitons in these materials enhances

the ability of excitons to interact with a surrounding electric field. These materials presented a suitable platform for the study of exciton-polaritons in the 1980-90s due to their controllable thickness at the nanoscale so that they could be introduced in optical microcavities.

2.5.2 Organic semiconductors

Lidzey, in 1998 and 1999 [45, 46], reported the observation of Rabi splitting at room temperature in a microcavity containing an organic semiconductor material: 5,6-dichloro-2-[[5,6-dichloro-1-ethyl-3-(4-sulphobutyl)-benzimida-zol-2-ylidene]-propenyl]-1-ethyl-3-(4-sulphobutyl)-benzimida-zolium hydroxide (TDBC). In these experiments, a Rabi splitting was observed indicating a strong coupling regime between excitons in the organic material and cavity photons. These results opened up the possibility of studying light-matter interactions using organic semiconductor materials.

It was recently reported that the electrical conductivity of a particular molecular semiconductor could be enhanced when these molecules are strongly coupled to a confined light field in a plasmonic array [47]. These remarkable results propose a way of controlling the physical properties of semiconductors by a light field, that has also been supported by theoretical formulations [48].

2.5.3 Semiconductor transition metal dichalcogenides

Transition metal dichalcogenides (TMDs) are a group of bi-elementary molecules in which one transition metal atom is covalently bonded to two chalcogenide atoms. Some of these molecules are semiconductors that can form a single crystalline phase that may be either hexagonal or rhombohedral when they are in solid form. In either case the transition metal atom is six-fold coordinated, surrounded by six chalcogenide atoms in a trigonal prismatic structure

[49]. This coordination allows for the formation of large areas of highly crystalline atomic layers. Weak Van der Waals forces hold the atomic layers together, enabling mechanical exfoliation of atomically thin single crystalline flakes by the sticky-tape method widely used to obtain graphene [50].

Among the semiconductor TMDs: WS_2, MoS_2, WSe_2, and $MoSe_2$ exhibit similar optical properties; a direct exciton transition at the K points of the first Brillouin zone when they are in the monolayer form, and a large binding energy which results in an absorption peak associated with neutral excitons of up to 20% [51], which is remarkable for an atomically thin layer. Neutral and charged excitons (or trions) can be formed in these materials and can be controlled through charge doping. When increasing the charge concentration of electrons in the conduction band for n-type semiconductors (or holes in the valence band for p-type semiconductors) negatively charged excitons are formed, which consist of a hole bound to two electrons (positively charged excitons are formed by an electron bound to two holes). When removing the charge doping, only neutral excitons are formed. Materials in this group of TMDs also have large oscillator strengths and low energy-loss factors for neutral excitons that result in narrow white light absorption peaks, and also in narrow photoluminescence peaks of the neutral exciton emission.

Figure 2.12 shows structural and electronic properties of semiconductor TMDs. a) is the top view of the hexagonal structure of a TMD monolayer. In this figure, we observe the lack of inversion symmetry of this structure, which has important implications in the electronic band structure and in the optical properties. b) is the first Brillouin zone of a), where key points are labelled as: Γ, K, K', and M. The distinction between K and K' arises from the time-reversal symmetry maintained by opposite spin states of electrons at the K and K' valley points, which produces opposite circular polarisation of the emission through

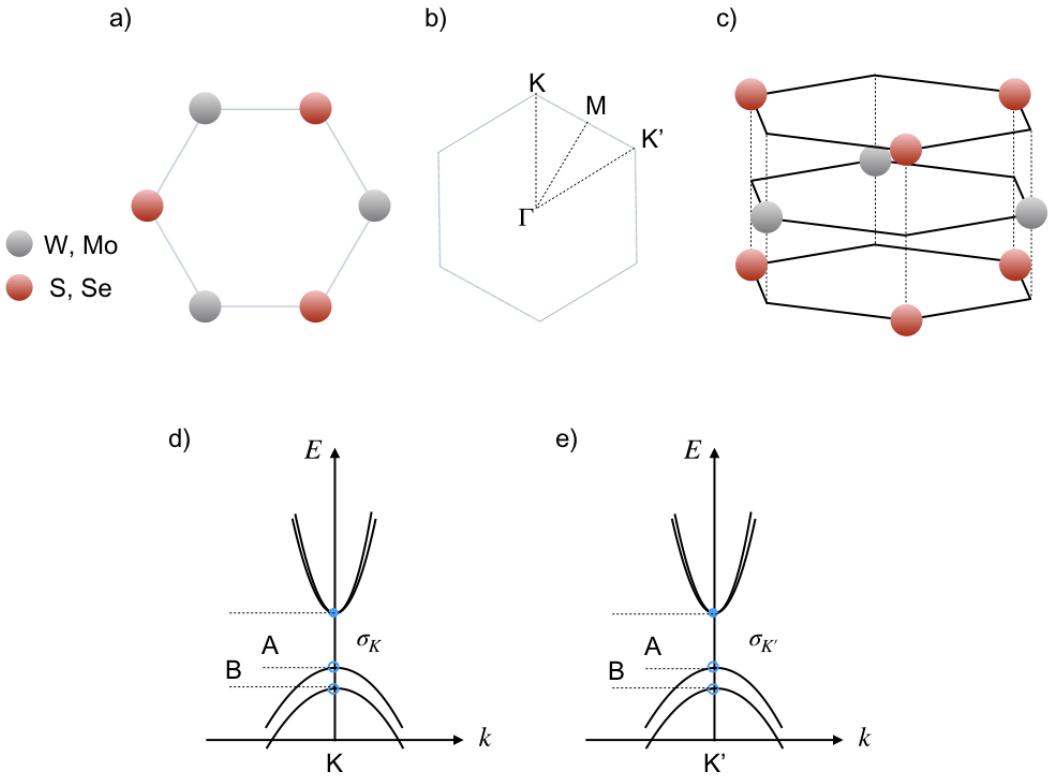

FIGURE 2.12: Schematic of the structural and electronic properties of TMDs (WS_2, MoS_2, WSe_2, and $MoSe_2$). (a) The hexagonal structure in real space and (b) in reciprocal space where symmetry points are indicated (Γ, K, K', and M). (c) Atomic structure of a TMD monolayer. (d) Direct electronic transition at the K points, where the recombination radiates circularly polarised light with polarisation σ_K, which has opposite sign to the recombination at the K' point, with polarisation $\sigma_{K'}$; this is shown in (e).

exciton recombination. c) is a schematic figure of a TMD monolayer which consists of a stack of a metal layer sandwiched between two chalcogenide layers where each metal atom is six-fold coordinated with chalcogenide atoms. Multilayer TMDs are formed by a stack of these monolayers bound by weak Van der Waals forces exerted at the interfaces of chalcogenide layers. d) and e) show the two opposite circular polarisations, σ_K and $\sigma_{K'}$, of photons produced from radiative recombination of excitons formed with electrons placed at the K or the K' valley point. This allows for interesting manipulation of the so-called K-valley degree of freedom, or valleytronics, as these valley-excitons can be

selected using circularly polarised light to excite them [52].

Figure 2.13 illustrates the origin of the A and B excitons from the spin-orbit coupling of d_m electrons of the metal atom in a TMD with trigonal prismatic coordination. TMDs of chemical formula MX_2 (M = Mo,W; X = Se,S) form molecules where the metal atom M and the chalcogenide atom X form covalent bonds through their p electronic orbitals. The metal atoms have d_m orbitals, where m is the magnetic quantum number; $m = 0, \pm 1, \pm 2$. Electrons partially fill the d_m orbitals and do not contribute to the covalent bonds. This allows for a strong spin-orbit coupling (SOC) at each metal atom. This coupling between the spin angular momentum and the orbital angular momentum of electrons in the partially filled d_m orbitals splits the d-energy levels as shown in Figure 2.13, which as a consequence produces a splitting of the valence band, and gives rise to two different direct electronic transitions at the K and K' points of the monolayer TMDs. The splitting of $d_{m=0}$ is not significant, possibly due to this sublevel being occupied by spin-up and spin-down electrons, while $d_{m=\pm 1}$ and $d_{m=\pm 2}$ are occupied by either spin-up or spin-down electrons, producing a significant splitting. The splitting of the $d_{m=0}$ sublevels have been theoretically studied in MoS_2 monolayers [53]; it has been found that the splitting in the conduction band is approximately 3 meV, which is smaller than the resolution of conventional spectroscopic methods. The $d_{m=0}$ splitting was observed experimentally through quantum transport measurements [54], and it was determined to be 0.8 meV. This discrepancy between theory and measurements is arguably due to the quality of the samples, which may have impurities and other defects.

Time reversal symmetry requires that an electron localised at a K point with a positive spin is related to an electron localised at the opposite position of the hexagonal Brillouin zone with the same spin. Maintaining this symmetry through opposite electron spin states gives rise to the K and K' valley points,

that produce optical transitions with opposite circular polarisation, enabling the study of rich valley-physics in monolayer TMDs [55, 56], including the valley-Zeeman effect [57, 58] and valley-Hall effect [59, 60]. A and B excitons occur at both the K and the K' valley points and they exhibit the same circular polarisation when the K or the K' valley point is excited [58].

The splitting of the $d_{m=\pm1}$ sublevels is not appreciable in spectroscopy experiments due to the low probability of exciton transitions involving these bands compared to bare electron-hole pairs. On the other hand, the splitting of the $d_{m=\pm2}$ sublevels is highly significant as excitons mediated by electronic transitions of electrons occupying these sublevels have a high probability for electronic transitions.

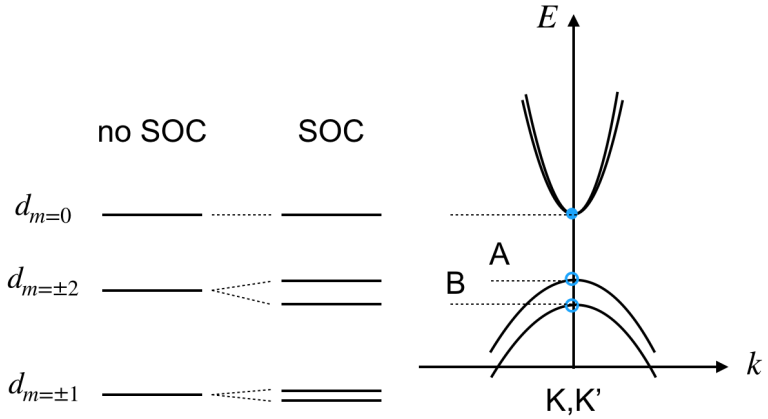

FIGURE 2.13: Illustration of the splitting of the d_m states of the metal atoms in TMDs due to spin orbit coupling (SOC), which gives rise to the A and B exciton transitions at the K and K' points, widely observed in monolayer TMDs.

Tungsten disulphide, WS_2, exhibits the largest oscillator strength among the four TMDs mentioned above, which makes it a suitable material for strong coupling investigations in optical microcavities of moderate quality factor (Q $\approx$ 100) at room temperature. Such a quality factor for optical confinement of light can be easily achieved using simple Fabry-Pérot microcavities made up of two flat silver mirrors. Exfoliated WS_2 monolayers have an energy-loss factor

of the neutral exciton transition of 35 meV, which produces a transmission peak width that is comparable to the widths of the Fabry-Pérot microcavity modes. In our measurements, we achieved a Rabi splitting of 60 meV with the third cavity mode, which is larger than both the exciton and the bare cavity mode line widths, so the system reaches the strong coupling regime [61].

Mechanically exfoliated monolayer tungsten disulphide flakes often exhibit natural negative doping which may occur by transfer of electrostatic charge from substrates or fabrication tools to the semiconductor. This natural doping can be neutralised by applying a gate voltage to remove the excess of free electrons from the conduction band. This appears to affect the excitation rate of neutral excitons; removing the excess of free electrons leads to an increase in both the white light transmittance peak associated with the neutral exciton transition and also in the emission of photons from the recombination of the neutral excitons. On the other hand, an increase of the free electrons in the conduction band of the monolayer semiconductor leads to a reduction of both the transmittance and the emission of photons from the neutral excitons, and it also leads to an increase in the excitation of negatively charged excitons, also called negative trions [62]. This phenomenon can be explained as screening of excitons due to an increase in the number density of free charge carries [63].

This dependence of the strength of the absorption peak on the free charge carrier density in the semiconductor has been studied in semiconductor quantum wells through laser excitation [64, 65]. The free charge carrier density increases as the laser power increases, leading to a decrease of the absorption peak of excitons due to a screening effect. More recently, control of the free charge carrier density in 2-dimensional semiconductors of the family of transition metal dichalcogenides has been studied through field effect gating [66]. By applying

a gate voltage to the semiconductor the charge doping can be controlled; increasing the charge carrier concentration leads to a reduction of the absorption and emission of excitons.

The first demonstration of the hybridization of excitons with the vacuum field in a monolayer semiconductor was reported in 2015 [67]. In this study, the transition metal dichalcogenide monolayer, molybdenum disulphide, was inserted in an optical microcavity structured in such a way that the TMD was placed at the antinode of the confined field, therefore supporting the excitation of exciton-polariton states in the strong coupling regime. This study opened the door to the realization of 2-dimensional light-matter hybrid systems with potential application in quantum technologies.

2.6 Optoelectronics in TMD exciton-polariton devices

Exciton-polaritons have been observed at room temperature in multiple devices that confine the light field combined with monolayer TMDs. To learn how to utilise these devices for real applications using exciton-polaritons more research is needed, especially in the control of hybrid light-matter particles. A few advances have been reported recently in the control of exciton-polaritons in optoelectronic devices through the manipulation of the charge carrier density in the semiconductor materials [68–71], which has important implications for the excitation of excitons and therefore the formation of exciton-polaritons.

A strong modulation of the absorption and photoluminescence mediated by excitons in conventional quantum wells (GaAs, AlGaAs) can be achieved by the application of a gate field [72]. A similar modulation was also observed through photoexcited charge carriers [64]. In such studies, the density of free electron-hole pairs is controlled by the pump laser power. Increasing unbound

electron-hole pairs produces a decrease of the absorption peaks associated with excitons. This is also accompanied by a decrease in the oscillator strength of excitons, which is explained by a screening of excitons due to an increase in the density of free electrons in the conduction band of the semiconductor, and holes in the valence band.

Figure 2.14(a) shows an illustration of a metal-insulator-semiconductor (MIS) capacitor which can be used to control the density of charge carriers in the conduction band for an n-type semiconductor, or in the valence band for a p-type semiconductor. The application of a bias voltage, or gate voltage, in this configuration of materials produces a displacement of charge carriers in real space that can modify the optical properties of the different materials. This effect depends strongly on the relative alignment of the band structure of the different materials. Figure 2.14(b) shows a schematic diagram of the bands of the different materials at a specific point in the wave-vector dimension, as a function of distance. For the case of monolayer TMDs, for example, this specific point in the wave-vector dimension can be the K or K' valley points. Charge carriers located at these points are mainly responsible for optical and electronic transport properties of TMD materials [62].

In Figure 2.14(b) ϕ_M is the work function of the metal with Fermi energy E_F; χ_I is the electron affinity of the insulator, χ_S is the electron affinity of the semiconductor with conduction and valence bands E_C and E_V respectively, E_i is the intrinsic Fermi energy of the semiconductor. At zero gate voltage, $V_G = 0$, in the absence of natural charge doping, the effective Fermi energy of the semiconductor E_F is the same as the intrinsic Fermi energy, and it is located in between the conduction and valence bands. E_{vac} is the vacuum energy level for free electrons, i.e. the minimum energy required to remove free electrons from the materials. Figure 2.14(b) shows the equilibrium condition of

the device.

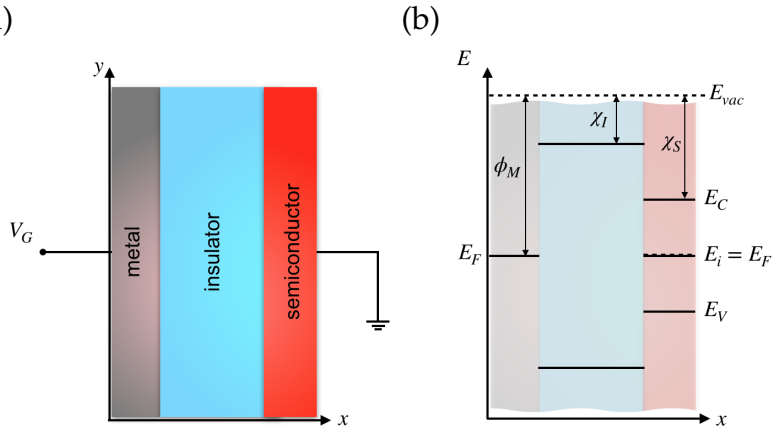

FIGURE 2.14: (a) Metal-insulator-semiconductor (MIS) capacitor in real space, where electrodes are indicated. (b) Relative band alignment of the different materials at a particular point in the reciprocal space, usually defined by the semiconductor material.

When a DC gate voltage is applied to the device, a capacitance effect occurs. For an n-type semiconductor, under positive DC gate voltage, the density of electrons increases in the conduction band, which is called the accumulation condition, as shown in Figure 2.15(a). The different bands of the semiconductor bend downwards due to an internal electric field created inside the material as a result of the charge accumulation, similar to a capacitor effect. Under negative DC gate voltage the bands of an n-type semiconductor bend upwards, with a lower effective Fermi level compared to the metal as shown in Figure 2.15(b). In this condition, called depletion, electrons flow away from the insulator-semiconductor interface. If the negative DC gate voltage increases even more, eventually the effective Fermi level reaches the intrinsic Fermi level of the semiconductor which is called an inversion condition, producing an accumulation of holes at the insulator-semiconductor interface as shown in Figure 2.5(c).

For a p-type semiconductor, Figure 2.15(d), (e), and (f) show the accumulation, depletion, and inversion conditions under the application of different DC

gate voltages. The device shown in Figure 2.14(a) with an n-type semiconductor

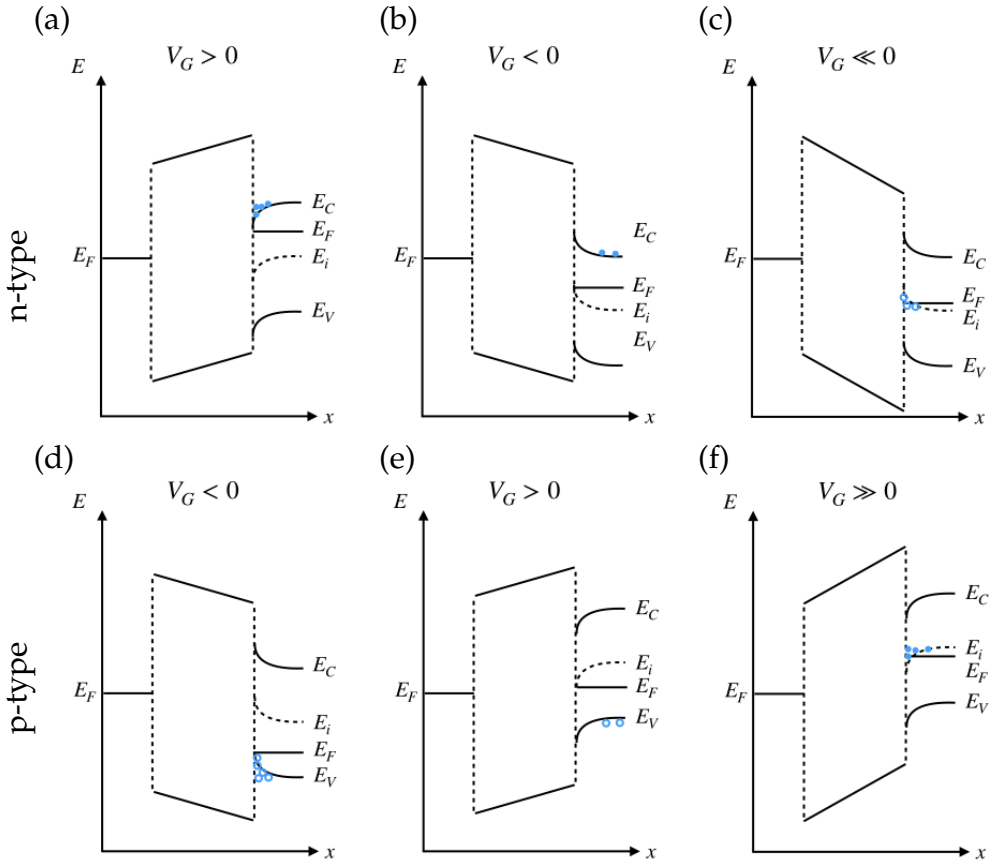

FIGURE 2.15: Band bending in a MIS capacitor under the application of a gate voltage V_G. The top row correspond to an n-type semiconductor, and the bottom to a p-type semiconductor. For reference, with $V_G = 0$, see Figure 2.14(b).

has an electrical current response to the application of a DC gate voltage as shown in Figure 2.16. This $I - V_G$ characteristic is usually observed in MIS devices combining silver as the metal electrode, with hexagonal boron nitride as an insulator, and monolayer tungsten disulphide as the semiconductor [61]. In the $I - V_G$ characteristic shown in Figure 2.16, the different device operation conditions described above are indicated. For a range of gate voltages no current is observed, the extent of this region depends on the thickness of the insulator. Above a positive threshold voltage the tunnelling current is observed in the accumulation condition. For higher values of the gate voltage the device operates as a regular Ohmic conductor. For negative values of the gate voltage

an inversion condition is observed which is associated with hole current. This

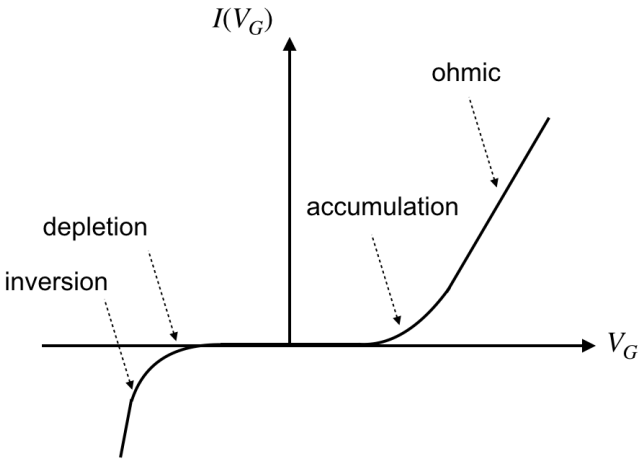

FIGURE 2.16: Current-voltage ($I - V_G$) characteristic curve for an n-type semiconductor. The different regimes that depend on the gate voltage are indicated.

accumulation of charges in the conduction or valence bands of TMDs provide a way to control the optical properties of these materials.

As discussed before, the accumulation of charge carriers reduces the excitation of excitons due to Coulomb screening, therefore reducing the coupling strength between excitons and a confined light field. This effect was observed in a MoS_2-based transistor built on a plasmonic array [68]. In this device, operating at room temperature, MoS_2 excitons are strongly coupled to plasmonic resonances, forming exciton-plasmon polaritons. In a range of bias voltages from 0 to 80 V, the coupling strength varies from a maximum value of 60 meV down to zero. Although this study presents essential details on the physics behind the control of exciton-polaritons through a DC gate voltage, other controversial observations are indicated such as negatively-charged excitons (trions) coupled to plasmon-polaritons, which is unexpected in these devices due to the relatively low value of the oscillator strength of trions. Unfortunately the data presented in this study does not allow for clarification of these conclusions.

Similar physics was observed in excitons supported by carbon nanotubes coupled to microcavity modes [70]. In this study a carbon nanotube-based transistor was built inside a monolithic microcavity to operate in the near-infrared range. The application of a gate voltage controls the coupling strength of exciton-polaritons at room temperature. This study presents remarkable results on the electrical control of exciton-polaritons in a device where exciton-polaritons can be turned on and off multiple times. A recent report shows similar results in a WS_2-based transistor built in a monolithic microcavity to operate at room temperature in the visible range [71]. These reports present essential advances for the control of exciton-polaritons at room temperature, through the manipulation of the optical properties of the excitonic materials. However, the reported devices have a low level of manipulation in terms of controlling the light field confinement.

Tuneable, also often called open-access microcavities, provide a way to control the light field confinement at room temperature [73] with the possibility of building up complex structures on one microcavity mirror [74] which is then brought closer to the second mirror, leaving a gap between them comparable to the wavelength. The electrical control over the coupling strength of WS_2 excitons with a tuneable microcavity mode has been reported in a device that also incorporates organic molecules [69]. In this report an in-plane bias voltage, which modifies the polarisability of the WS_2 monolayer, strongly affects the formation of exciton-polaritons. However, in this device there is no direct manipulation of the density of charge carriers in the conduction band of the semiconductor.

2.7 Summary

In this Chapter, the main concepts involved in the study of light-matter interactions were introduced. A historical overview highlights the intrigue of the physics behind light-matter interactions driven mainly by the curiosity of the scientists who contributed to the understanding of this field. A way to manipulate light-matter interactions is also described; this involves the confinement of a light field in order to enhance the interaction with matter. Suitable matter particles that interact with a confined light field are those that can be described as a two-level quantum system; the two levels are energy states, a ground state and an excited state that is reached by the action of the light field on the matter particle. When the two-level system decays from the excited state to the ground state electromagnetic energy is released, feeding the confined light field back. If this process occurs many times before the overall energy dissipates, the light-matter system forms a new quasi-particle with properties that combine both constituents: the light field and the matter particle.

Excitons can be approximated as a two-level quantum system, which can be observed in semiconductor materials. Two-dimensional semiconductor materials confine excitons in a narrow space, which enhances the ability of excitons to interact with a confined light field. This ability can also be manipulated, and as a consequence a light-matter quasi-particle involving excitons can be controlled; it can be turned on and off as desired, and this is the main focus in the research presented in this thesis.

Chapter 3

Experimental methods

This chapter is entirely dedicated to the description of the tuneable microcavity setup that was built and implemented during the study presented in this thesis. Moreover, this tuneable system was integrated with the ability to perform measurements of the electronic properties of semiconductors. Optical and electronic measurements were automated and performed in synchronisation, significantly improving the stability and resolution of the experimental results. I describe the design of the tuneable system and the performance at room temperature, supported by stability test measurements. Then I describe the evolution of measurements since the first manual operation until I incorporated automation, which allowed a reduction of the acquisition time and improved the resolution by at least one order of magnitude.

3.1 Tuneable microcavity setup

3.1.1 Design

Optical transmission measurements were performed in a confocal system specially designed for a tuneable microcavity. This optical setup is shown in Figure 3.1, where the different components are labelled and the system of reference is also indicated. White light propagates along the z-axis, and four objective lenses comprise the confocal system. The first lens on the left side collimates the white light beam from a $50\mu m$ core diameter optical fibre. A second X10 lens focuses the light beam on an area in between two XYZ-$\alpha\beta$ mounts. An X50 objective lens collects light from an area of $100\mu m^2$, which is achieved by focusing the collected light on an optical fibre of core diameter $50\mu m$ using a X10 objective lens. This fibre directs the light to a fibre-coupled spectrometer. Each of the two XYZ-$\alpha\beta$ mounts at the centre of the optical setup holds one mirror of the microcavity. These mounts are a combination of a tilt kinematic mount with an XYZ stage; the kinematic mount can tilt around the X (α) and Y (β) axes. One of the XYZ stages incorporates a piezo-control (piezo-stage in Figure 3.1), which allows for the positioning of one of the mirrors with nanometer precision. In Figure 3.2 a close up of the area where samples are placed is shown, as well as how white light is focused on a point between the two objective lenses. The specially designed sample holder is placed in the kinematic mounts. They support 1 cm^2 and 1 $inch^2$ glass substrates (see Figure 3.3)

3.1.2 Parallelism correction

A significant improvement in the performance of the tuneable microcavity results from the alignment of the two mirrors to make them parallel. This alignment uses Newton's rings, which consists of an interference pattern created

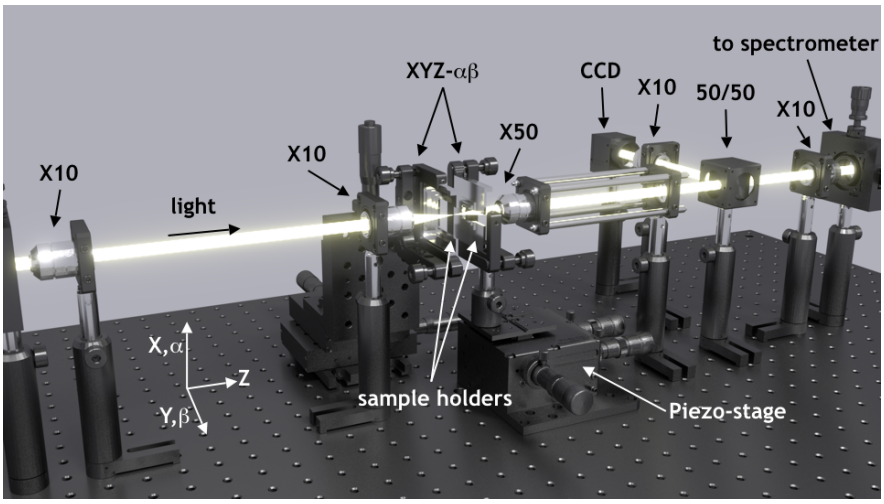

FIGURE 3.1: 3D-model of the tuneable microcavity setup. The optics comprise a fibre-coupled confocal system using four objective lenses. The area for light collection has a diameter of $10\mu m$.

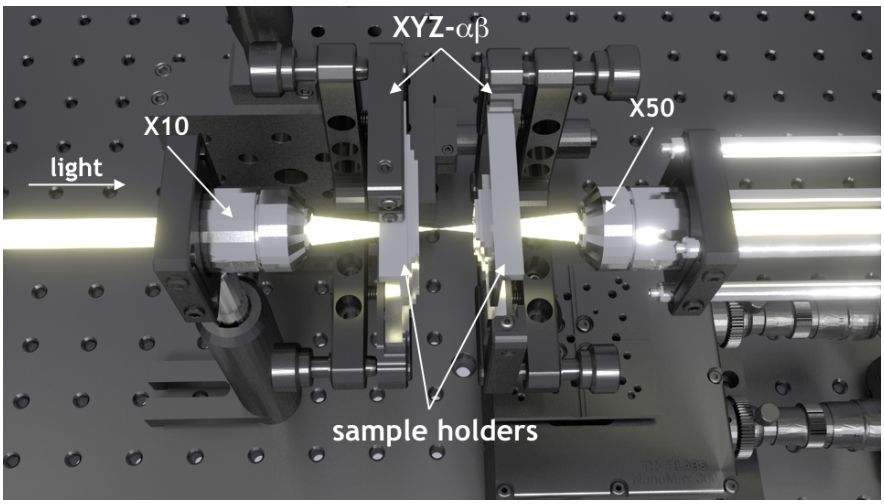

FIGURE 3.2: 3D-model of the centre of the optical setup where samples are placed. The collection area between the two objective lenses is $100\mu m^2$. Samples are held on the XYZ-$\alpha\beta$ mounts.

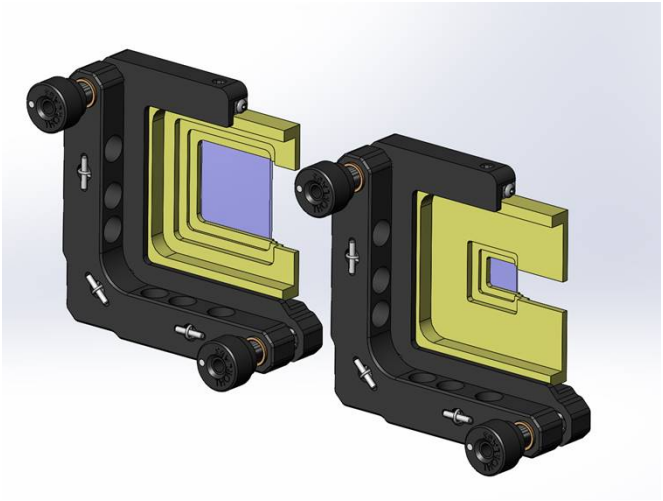

FIGURE 3.3: 3D-model of the glass substrate holders placed in the kinematic mounts: (left) holds a 1" glass substrate, (right) holds a 1 cm glass substrate. In this configuration the holders with samples can be easily removed and replaced without altering the position of the kinematic mount.

by multiple reflections between the two flat mirrors of the microcavity. When the mirrors are perfectly parallel, it is expected to have a ring pattern perfectly centred on the optical axis. If the mirrors are not entirely parallel, which is usually the case, the centre of the ring pattern is far from the optical axis. The alignment consists of bringing the centre of the ring pattern to the optical axis by tilting the mirrors using the kinematic mounts. A CCD camera which is initially well aligned with the optical axis is used for this procedure.

The following is a step-by-step procedure for the alignment, starting with two silver mirrors which are placed far apart and opposite to each other in the setup. The thickness of the silver films on glass is 40 nm. This thickness provides enough transparency to see through the two mirrors of the microcavity using a CCD camera. One silver mirror has a strip shape, and the other has a square shape (plinth mirror). First, the collection fibre has to be aligned. For this white light is sent through the fibre. The CCD camera collects an image of the collection fibre which corresponds to the area from which light is collected. This

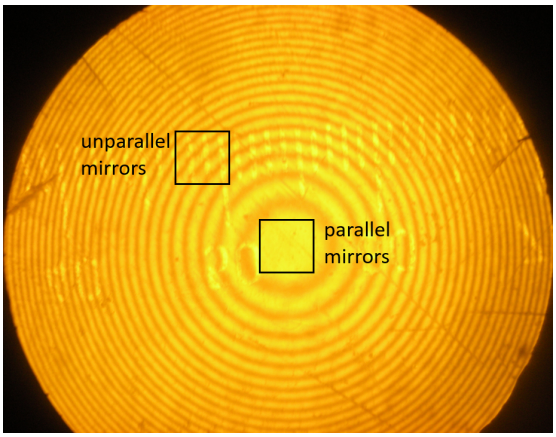

FIGURE 3.4: Example of Newton's rings [75] formed by two mirrors. Square regions indicate what would be observed with a high magnification camera depending on how parallel the mirrors are.

is shown in Figure 3.5(1). Second, white light is sent through both of the silver mirrors to identify their relative positions, as shown in Figure 3.5(2). In this step the mirrors are brought as close as possible while avoiding contact between them. Third, the plinth mirror is brought back a few micrometres. Fourth, a bandpass filter is used in the white light source to provide a monochromatic beam passing through the mirrors. An interference pattern is observed on the camera as oblique lines, which indicates that both the α and β angles of the tilt mount have to be corrected. Fifth, once the α angle is corrected horizontal lines are observed, which indicates that only the β angle is yet to be corrected. Sixth, once the β angle is also corrected, no lines are observed on the camera. The bandpass filter can be removed to start transmission measurements.

3.1.3 Stability testing

Once mirrors are parallel, they can be brought closer using the manual positioners of the piezo-stage. Several peaks are observed in the transmission spectrum in the visible range when the mirrors are separated by an air gap with thickness on the order of tens of micrometres. Figure 3.6 shows a set of transmission spectra collected every 5 minutes for 23 hours. In this figure, cavity modes

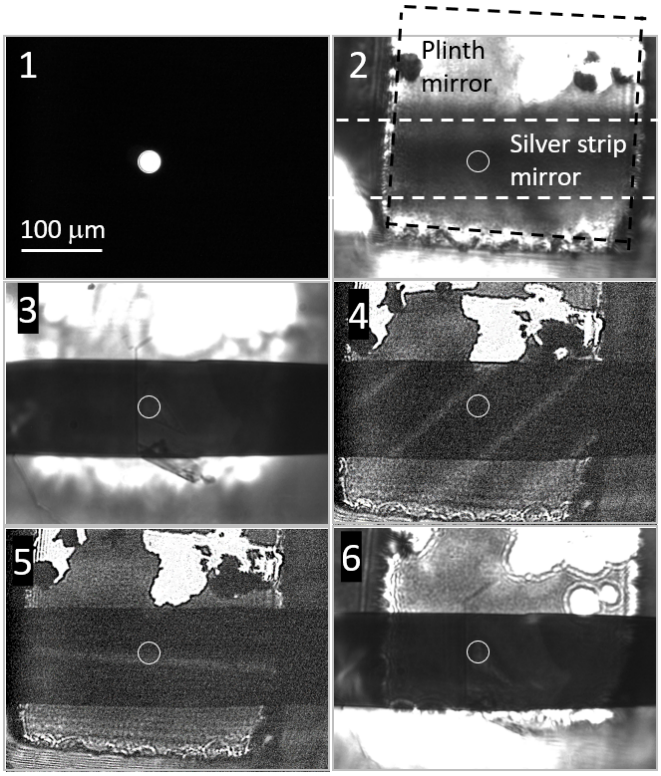

FIGURE 3.5: Steps for the tuneable microcavity alignment. (1) the spot-size for light collection is observed on the sample. (2) the top mirror (plinth mirror) is approached to the substrate with the silver strip mirror. At this point the gap between the two mirrors is ~ 20 μm. (3) the gap is increased for parallelism alignment (to avoid contact between the mirrors). (4) a red band-pass filter is inserted in the illumination optics to observe interference fringes (see Figure 3.4). (5) one tilt angle is corrected first; oblique interference fringes become horizontal. The second tilt angle can be corrected by separating the horizontal interference fringes until none is visible on the screen. (6) the band-pass filter can be removed to continue with transmission measurements.

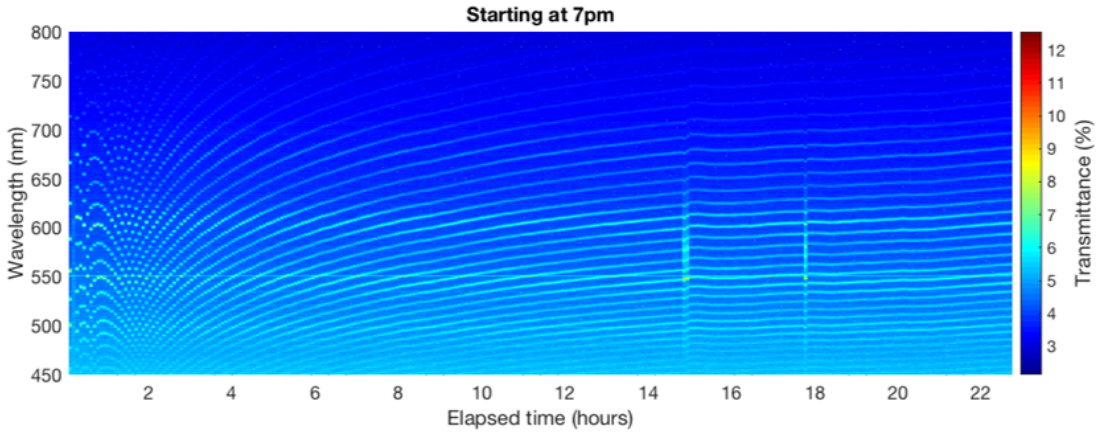

FIGURE 3.6: Stability test of the tuneable microcavity.

are observed as lines that change with time, which indicates instability of the system. These data were collected after parallelism alignment, and during collection no components were intentionally altered in the optical setup. The significant shift of the modes during the first 2 hours is associated with mechanical relaxation of the different components that were used in the parallelism alignment. After 3 hours the modes start becoming stable; between hours 3 and 5 the shift of the modes is less than 50 nm. In the last two hours the shift of the modes is only 5 nm indicating excellent stability in a reasonably long period for transmission measurements. The two vertical lines observed at 15 and 18 hours correspond to moments when the door of the microcavity-lab was opened. The tuneable system allows for high quality measurements after the system reaches excellent stability, and this happens after at least 12 hours. Samples must be mounted and aligned, and the system must be left to relax before starting to perform measurements on the next day.

3.1.4 Refining measurements: automated data collection

Once the silver mirrors are aligned transmission measurements are carried out as a function of the piezo-voltage. By applying a positive voltage, the

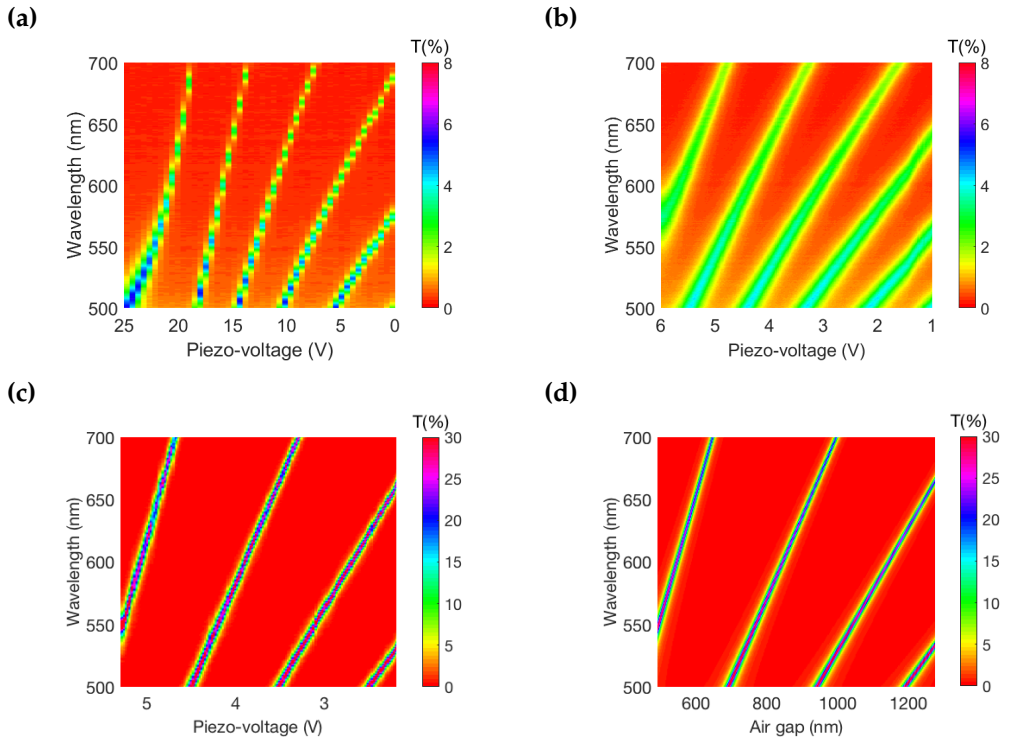

FIGURE 3.7: Refinement of transmission measurements of an empty cavity as a function of the piezo-voltage: (a) transmittance map as a function of the piezo-voltage supplied through a manually controlled power source, (b) transmittance map collected through an automated protocol using LabView, (c) improved transmission measurements filtering incident angles using a pinhole in the collimated incident light and normalising transmitted light, (d) calculated transmittance in a range of air gap thickness to match the measurements shown in (c).

piezo-stage translates the top mirror closer to the substrate mirror. Transmission spectra are recorded for every piezo-voltage step. In Figure 3.7(a) a map of the transmittance as a function of the piezo-voltage is shown. For these measurements, the piezo-voltage is supplied by a manually controlled power source; the voltage step is 0.1 V. To improve these measurements the power source was incorporated into an automated protocol in LabView, along with the spectrometer. The protocol consists of recording a transmittance spectrum for every value of the piezo-voltage, in steps of 0.01 V, which provides a resolution ten times higher than the manual control. The automated protocol also

allows for faster data collection; measurements shown in Figure 3.7(a) took ~ 60 min, while measurements shown in Figure 3.7(b) took only 10 min. Faster data collection manifests as more linear cavity modes varying as a function of wavelength, due to a less significant thermal or mechanical drift in this short period. Figure 3.7(d) shows a theoretical calculation of the transmittance of an empty microcavity as a function of the air gap thickness for a range of values from 475 to 1290 nm. An excellent agreement between data shown in Figures 3.7(c) and 3.7(d) is observed, which allows for a conversion from piezo-voltage values to air gap thickness.

Chapter 4

Theory for Modelling

In this chapter, a brief description of the relevant theory involved in the study of this thesis is given. The aim is to describe how to obtain all the results based on calculations that are included in novel studies included in Chapters 5 and 6. This chapter describes the Lorentz model of the permittivity, which can be used to calculate the permittivity of materials with multiple optical resonances due to either inter- or intra-molecular electronic transitions. Also included in this chapter is the matrix formalism for the calculation of white light transmittance and reflectance of a multilayer structure. A slab of dielectric material, as well as an empty microcavity, are used as case-studies. These calculations can be used to find the transmittance and reflectance of a device that supports exciton-polaritons, e.g. a semiconductor microcavity where a semiconductor material that supports excitons is inserted in the microcavity. This matrix approach can be used to calculate the electric field of the confined light in the microcavity system. The relevant equations for these calculations are also derived in this chapter. In later sections, a classical coupled oscillator model is presented and used to obtain the power spectrum of a coupled system. This is used to present a classical analogy to exciton-polariton states as observed in spectroscopy experiments. I show here that the concepts involved in the

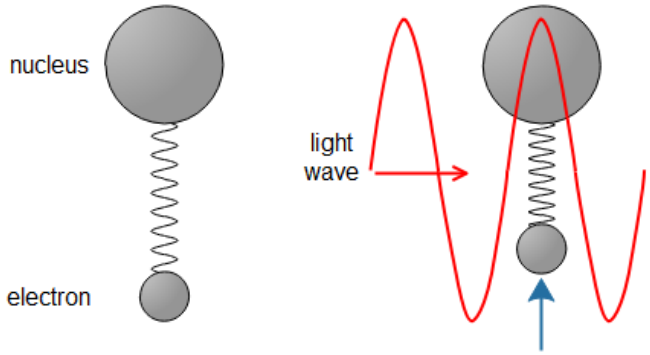

FIGURE 4.1: Electron and nucleus described as two masses attached by a spring. A light wave exerts a force over the electron that produces a displacement, which in turn produces a polarisation of the system.

formation of exciton-polaritons, such as energy exchange, can be well described with this classical analogy. Additionally, different criteria for the weak and strong coupling regimes are described. Finally, in this chapter, I include a description of the composition of the exciton-polariton bands formed in a tuneable microcavity, where the cavity length can be chosen as a variable as well as the wave-vector of the light mode. From this the so-called Hopfield coefficients in a strongly coupled semiconductor microcavity are obtained, and a description on how to use these calculations to extract experimental results is also described.

4.1 Lorentz model of the permittivity

Let us start by considering an atom as a system of a nucleus and an electron attached by a spring as shown in Figure 4.1, where the mass of the electron is much smaller than the mass of the nucleus.

In this system the interaction between a light wave propagating from left to right produces a displacement $\vec{x}(t)$ of the electron with respect to its equilibrium

position due to the electromagnetic force exerted on the electron. This displacement in turn produces a polarisation $\vec{p}(t)$ of the atom. The displacement $\vec{x}(t)$ of electrons bound to the nucleus can be described by a forced-damped harmonic oscillator, which can be modelled by the Equation 4.1,

$$m_0 \frac{d^2\vec{x}}{dt^2} + m_0\gamma\frac{d\vec{x}}{dt} + m_0\omega_0^2\vec{x} = -e\vec{\mathcal{E}}, \tag{4.1}$$

where m_0 is the electron mass, γ is the damping factor of the restoring force that keeps the electron bound to the nucleus, ω_0 is the resonant frequency of the electron displacement, e is the electron charge, and $\vec{\mathcal{E}}$ is the electric field intensity of the light wave, so $-e\vec{\mathcal{E}}$ is the force that produces the electron displacement. This displacement produces a local polarisation $\vec{p}(t) = -e\vec{x}(t)$. In a collection of N particles per unit volume, the macroscopic polarisation is

$$\vec{P}(t) = -Ne\vec{x}(t). \tag{4.2}$$

By substituting this expression into Equation 4.1 we obtain

$$\frac{d^2\vec{P}}{dt^2} + \gamma\frac{d\vec{P}}{dt} + \omega_0^2\vec{P} = \frac{Ne^2}{m_0}\vec{\mathcal{E}}. \tag{4.3}$$

If we describe the light wave as $\vec{\mathcal{E}}(t) = \vec{\mathcal{E}}_0 exp(-i\omega t)$, we can look for solutions of the form $\vec{P}(t) = \vec{P}_0 exp(-i\omega t)$. By substituting this expression into Equation 4.3 we find

$$P_0 = \mathcal{E}_0\frac{Ne^2}{m_0}\frac{1}{\omega_0^2 - \omega^2 - i\gamma\omega}. \tag{4.4}$$

The collective electric displacement depends on the electric field and the polarisation through

$$\vec{D} = \varepsilon_0\vec{\mathcal{E}} + \vec{P}. \tag{4.5}$$

In linear, isotropic media the displacement can also be related to the electric field by

$$\vec{D} = \varepsilon_0 \varepsilon_r \vec{\mathcal{E}}, \tag{4.6}$$

where ε_r is the relative permittivity. By combining these equations with Equation 4.4 we obtain

$$\varepsilon_r = 1 + \frac{Ne^2}{m_0 \varepsilon_0} \frac{1}{\omega_0^2 - \omega^2 - i\gamma\omega}. \tag{4.7}$$

Equation 4.7 is the Lorentz model of the permittivity, which is a complex number where the real and the imaginary parts account for the way the atoms absorb light. The different parameters in this equation, mainly ω_0 and γ, allow modelling of the transmission and reflection of light in metals, dielectrics, and absorbing materials.

4.1.1 Permittivity of metals

For the case of metals the electrons are free to move so there is no resonant frequency ($\omega_0 = 0$), but they still respond collectively to external excitations, so the attenuation factor is non-zero ($\gamma \neq 0$). By applying these changes to Equation 4.7 we obtain

$$\varepsilon_r = 1 - \frac{\omega_p^2}{\omega^2 + i\gamma\omega}, \tag{4.8}$$

which is know as the Drude model of the permittivity of metals, where ω_p is the plasma frequency ($\omega_p^2 = Ne^2/m\varepsilon_0$). The permittivity of silver used for calculations of optical properties utilises parameters obtained from reference [76]. Figure 4.2 shows a calculation of the real (blue line) and the imaginary (red line) components of the permittivity of silver using Equation 4.8.

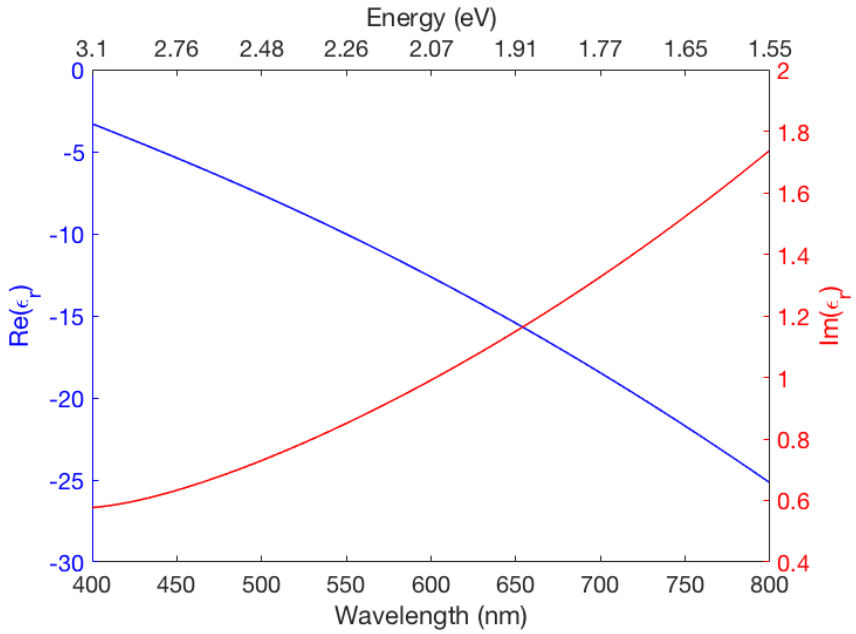

FIGURE 4.2: Real (blue) and imaginary (red) components of the relative permittivity of silver, as a function of wavelength in the visible range. The parameters used in this calculation are taken from reference [76].

4.1.2 Permittivity of excitonic materials

For the case of excitons, the resonant frequency ω_0 is associated with interband transitions mediated by light absorption. A dimensionless number must be introduced to take into account the probability of generating an exciton when photons are absorbed; this number is the oscillator strength f. The permittivity that considers multiple interband transitions is given by

$$\varepsilon_r(\omega) = 1 + \sum_{j=1}^{k} \frac{f_j \omega_{0,j}^2}{\omega_{0,j}^2 - \omega^2 - i\gamma_j \omega}. \tag{4.9}$$

Figure 4.3 shows the real (blue line) and the imaginary (red line) components of the permittivity of WS_2. In this figure, a narrow peak in the imaginary component is observed, which indicates a strong absorption at a wavelength of 622 nm. The parameters used for this calculation are shown in Table 4.1, where the three interband transitions are associated with neutral (A^0), negatively

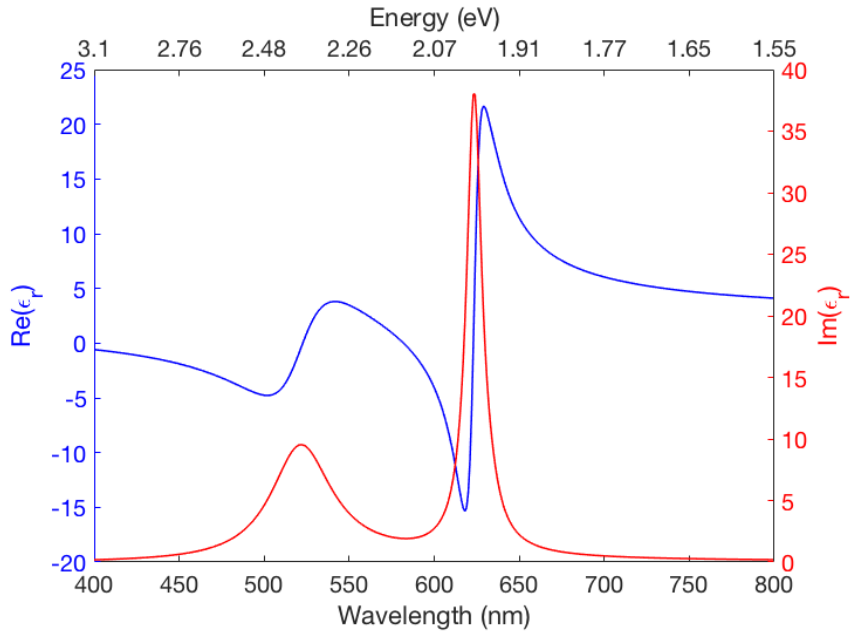

FIGURE 4.3: Real (blue) and imaginary (red) components of the relative permittivity of WS_2, as a function of wavelength in the visible range. This is a calculation using Equation 4.9 with parameters listed in Table 4.1.

j	$\hbar\omega_{0,j}$ (eV)	f_j	γ_j (eV)
1	1.995	2.70	0.035
2	1.960	0.04	0.040
3	2.350	5.00	0.200

TABLE 4.1: Parameters for the permittivity of WS_2.

charged (A^-), and B exciton transitions [67]. Following the same procedure, Figure 4.4 shows a calculation of the permittivity of MoS_2 using the parameters listed in Table 4.2.

j	$\hbar\omega_{0,j}$ (eV)	f_j	γ_j (eV)
1	1.84	1.4	0.040
2	1.80	0.3	0.080
3	1.96	2.0	0.090

TABLE 4.2: Parameters for the permittivity of MoS_2.

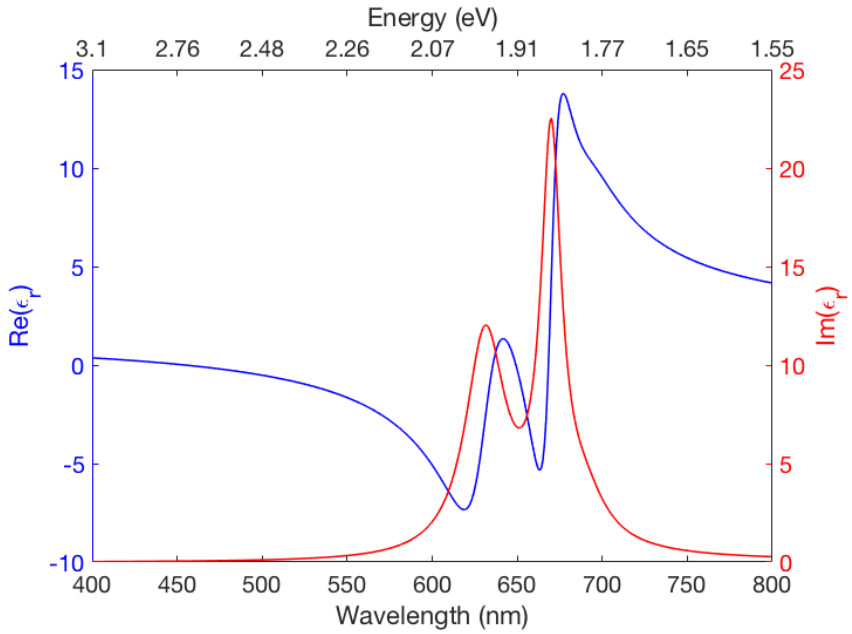

FIGURE 4.4: Real (blue) and imaginary (red) components of the relative permittivity of MoS_2, as a function of wavelength in the visible range. This is a calculation using Equation 4.9 with parameters listed in Table 4.2.

4.2 Optics of multilayer structures

In this section the calculation of the transmission and reflection coefficients of a multilayer structure composed of metals, dielectrics, and excitonic materials is described.

4.2.1 Transmission and reflection of a slab material

Let us first consider Figure 4.5, where the different wave-vectors of light propagating through a slab of material with refractive index n_1 are shown. In these systems, the slab is surrounded by two different media with refractive indices $n_0 > n_1$ and $n_2 > n_1$. This analysis considers materials with magnetic permeability equal to 1. An incident light-wave with wave-vector $\vec{k}_{0,i}$, at an angle $\theta_{0,i}$, is reflected and transmitted through the interface a_{01}. The incident light-wave has a particular wavelength λ_0. The incident wave is (initially) TM

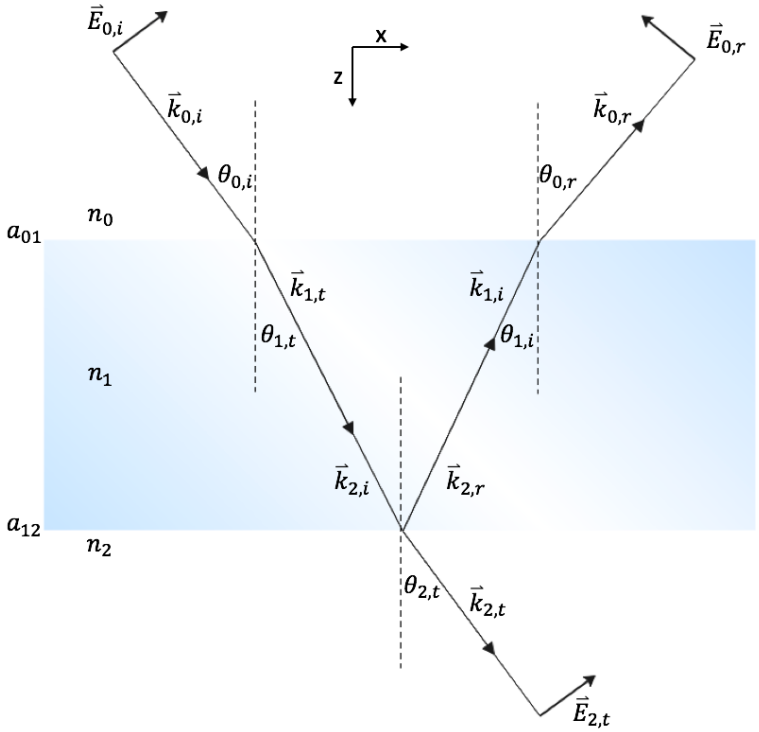

FIGURE 4.5: Schematic of a slab material surrounded by air. Wave-vectors and angles of refraction are indicated.

polarised so the electric field associated with this light wave $\vec{E}_{0,i}$ is oriented on the (x, z) plane as indicated in Figure 4.5. The reflected electric field at the interface a_{01} is $\vec{E}_{0,r}$ and the transmitted is $\vec{E}_{2,t}$. The transmitted wave-vector is subsequently reflected and transmitted at the interface a_{12}. The transmission and reflection coefficients t and r are defined in terms of the incident, the transmitted, and the reflected electric fields associated with the light wave propagating through the whole system. These coefficients are

$$\begin{aligned} t &= \frac{|\vec{E}_{2,t}|}{|\vec{E}_{0,i}|}, \\ r &= \frac{|\vec{E}_{0,r}|}{|\vec{E}_{0,i}|}. \end{aligned} \tag{4.10}$$

These coefficients can be determined by calculating $|\vec{E}_{2,t}|$, and $|\vec{E}_{0,r}|$, while

setting $|\vec{E}_{0,i}| = 1$. We now have to impose boundary conditions at the two different interfaces, a_{01}, and a_{02}. The parallel component of the incident, transmitted and reflected electric fields at the interfaces must be conserved. This means the following conditions must be satisfied,

$$|\vec{E}_{0,i}|cos(\theta_{0,i}) - |\vec{E}_{0,r}|cos(\theta_{0,r}) = |\vec{E}_{1,t}|cos(\theta_{1,t}) - |\vec{E}_{1,i}|cos(\theta_{1,i})$$
$$|\vec{E}_{1,i}|cos(\theta_{1,i}) - |\vec{E}_{1,r}|cos(\theta_{1,r}) = |\vec{E}_{2,t}|cos(\theta_{2,t}).$$

We can also write the boundary conditions for the parallel components of the magnetic field, which in the TM mode are pointing out of the plane of the figure, in the y direction:

$$|\vec{B}_{0,i}| + |\vec{B}_{0,r}| = |\vec{B}_{1,t}| + |\vec{B}_{1,i}|,$$
$$|\vec{B}_{1,i}| + |\vec{B}_{1,r}| = |\vec{B}_{2,t}|.$$

Our objective is to write these boundary conditions as a function of only $|\vec{E}_{2,t}|$, $|\vec{E}_{0,r}|$, and $|\vec{E}_{0,i}| = 1$, so we can calculate the transmission and reflection coefficients using Equation 4.10. In a medium with refractive index n, the magnitudes of the magnetic and the electric field are related by $B = n\sqrt{\varepsilon_0\mu_0}E$, where ε_0 and μ_0 are respectively the permittivity and permeability of free space. With these definitions, the boundary conditions can be reduced to

$$\begin{aligned} cos(\theta_0)(|\vec{E}_{0,i}| - |\vec{E}_{0,r}|) &= cos(\theta_1)(|\vec{E}_{1,t}| - |\vec{E}_{1,i}|), \\ cos(\theta_1)(|\vec{E}_{2,i}| - |\vec{E}_{2,r}|) &= cos(\theta_2)|\vec{E}_{2,t}|, \\ n_0(|\vec{E}_{0,i}| + |\vec{E}_{0,r}|) &= n_1(|\vec{E}_{1,t}| + |\vec{E}_{1,i}|), \\ n_1(|\vec{E}_{2,i}| + |\vec{E}_{2,r}|) &= n_2|\vec{E}_{2,t}|. \end{aligned} \tag{4.11}$$

where we assumed $cos(\theta_{0,i}) = cos(\theta_{0,r}) = cos(\theta_0)$, and $cos(\theta_{1,t}) = cos(\theta_{1,i}) = cos(\theta_1)$.

Next we need to relate the magnitudes of the electric field at each interface by a phase change, which depends on the thickness d_1 of the slab and the refractive index n_1. This phase change is $\beta = k_0 n_1 d_1 cos(\theta_{1,t})$, where $k_0 = 2\pi/\lambda_0$, thus

$$|\vec{E}_{2,i}| = |\vec{E}_{1,t}| exp(-i\beta),$$
$$|\vec{E}_{1,i}| = |\vec{E}_{2,r}| exp(-i\beta).$$

We may now remove $|\vec{E}_{2,i}|$, $|\vec{E}_{2,r}|$, $|\vec{E}_{1,i}|$, and $|\vec{E}_{1,r}|$ from the boundary conditions with some algebra, to finally obtain the boundary conditions in matrix form as follows

$$\begin{bmatrix} (|\vec{E}_{0,i}| + |\vec{E}_{0,r}|) \\ Z_0(|\vec{E}_{0,i}| - |\vec{E}_{0,r}|) \end{bmatrix} = \begin{bmatrix} cos(\beta) & -i\, sin(\beta)/Z_1 \\ -i\, sin(\beta) Z_1 & cos(\beta) \end{bmatrix} \begin{bmatrix} |\vec{E}_{2,t}| \\ Z_2 |\vec{E}_{2,t}| \end{bmatrix}, \quad (4.12)$$

where $Z_j = n_j/cos(\theta_j)$ for the TM polarisation, with $j = \{0, 1, 2\}$. For the TE polarisation $Z_j = n_j \cdot cos(\theta_j)$.

Equation 4.12 is known as the transfer matrix method (TMM), and has many applications in one dimensional light propagation through a multilayer structure. The 2×2 matrix on the right side of Equation 4.12 is the transfer matrix $\mathcal{M}$ which represents the optical properties of the slab material in our system. This matrix depends on the refractive index, and the thickness of the slab material; $\mathcal{M} = \mathcal{M}(n_1, d_1)$. We may now combine Equations 4.12 and 4.10

to find an analytical expression for the transmission and reflection coefficients,

$$t = \frac{2Z_0}{Z_0 m_{11} + Z_0 Z_2 m_{12} + m_{21} + Z_2 m_{22}},$$
$$r = \frac{Z_0 m_{11} + Z_0 Z_2 m_{12} - m_{21} + Z_2 m_{22}}{Z_0 m_{11} + Z_0 Z_2 m_{12} + m_{21} + Z_2 m_{22}}, \tag{4.13}$$

where m_{11}, m_{12}, m_{21}, and m_{22} are the coefficients of the transfer matrix in Equation 4.12. The transmission and reflection coefficients can be calculated for a range of wavelengths of the incident light wave, and also for a range of incident angles θ_0. It is also possible to calculate these coefficients for a range of thicknesses of the slab material. Now we can calculate the transmittance and reflectance by

$$T = \frac{Z_2}{Z_0}|t|^2,$$
$$R = |r|^2. \tag{4.14}$$

4.2.2 Transmittance and reflectance of an optical microcavity

For a structure with more slabs of different materials, the transfer matrix method described in the previous subsection can be extended by writing one matrix $\mathcal{M}_j$ for each material j and then calculating the total matrix $\mathcal{M}_T$ which is the multiplication of all the individual N-matrices; $\mathcal{M}_T = \Pi_{j=1}^{N} \mathcal{M}_j$.

Let us consider the multilayer structure shown in Figure 4.6. In this figure, two more slabs are added to the structure shown in Figure 4.5. The two new slabs are silver films, which are shown in grey, and have a thickness of 40 nm each. The top and the bottom silver films have refractive indices n_1 and n_3 respectively, that depend on the permittivity of silver as described by Equation 4.8, and $n = \sqrt{\varepsilon_r}$. The slab in the middle has a refractive index of $n = 1.5$, and a thickness of 160 nm. We now calculate the transmittance and reflectance of

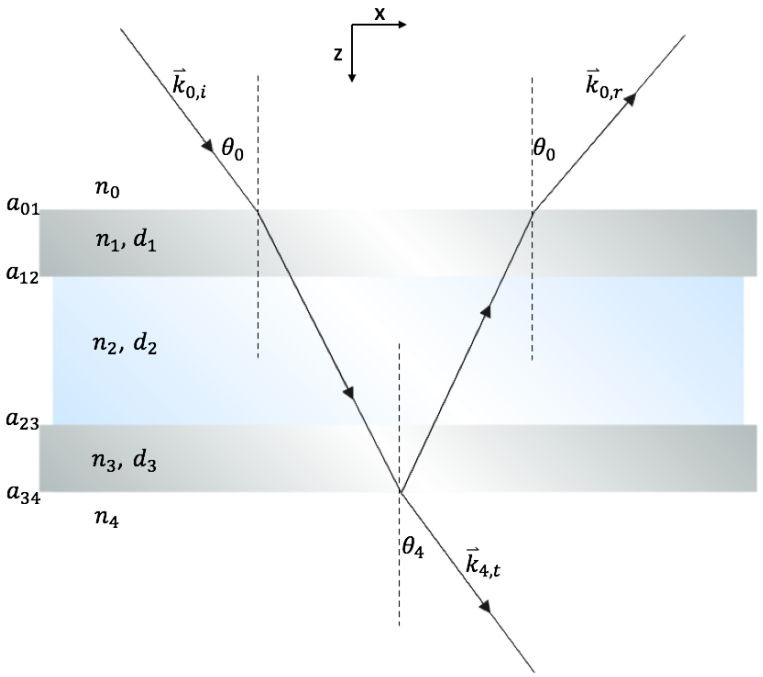

FIGURE 4.6: Schematic figure of a simple microcavity composed of two silver mirrors shown in grey, separated by a slab of refractive index $n_2 = 1.5$.

the microcavity structure by using Equation 4.14 for a range of wavelengths from 400 to 800 nm, and for a range of incident angles from -90 to +90 degrees. The result is shown in Figure 4.7. In this figure we observe a narrow band in both the transmittance and the reflectance plots which correspond to the first order cavity mode. From these results we can calculate the dispersion relation of the microcavity by calculating the energy of the propagating wave using $E = hc/\lambda$ (where h is the Planck's constant, and c the speed of light in free space), and constructing a plot of this energy as a function of the parallel component of the incident wave-vector to the surface of the microcavity, which is $k_{||} = k_0 sin(\theta_0)$. This dispersion plot is shown in Figure 4.8. In this figure we observe the first-order cavity mode with an energy of 1.9 eV at zero in-plane wave-vector, with a mode width of 35 meV. This energy corresponds to red light, so this cavity can be used as a red band-pass filter which transmits red at ~30%.

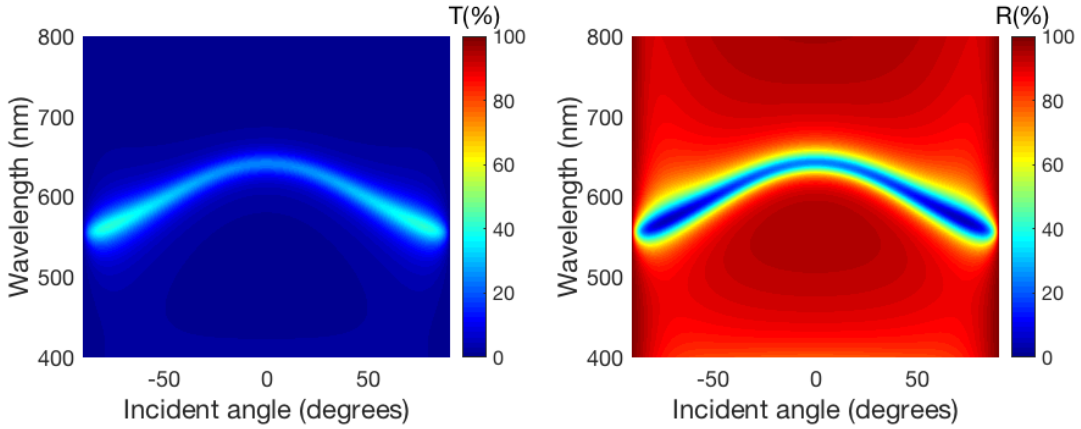

FIGURE 4.7: Transmittance (left) and reflectance (right) of the cavity structure shown in Figure 4.6. For these calculations, $n_2 = 1.5$, $d_2 = 160$ nm, the permittivity of silver is obtained from [76], and the thickness of the silver films is 40 nm.

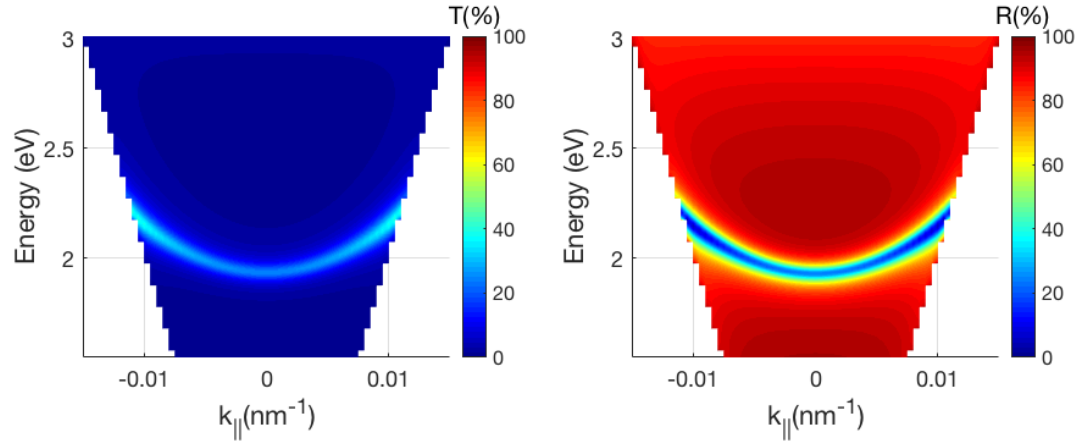

FIGURE 4.8: Dispersion diagram of the cavity structure shown in Figure 4.6. For these calculations the same parameters as in Figure 4.7 are used, however, the results are presented in the energy/wave-vector space.

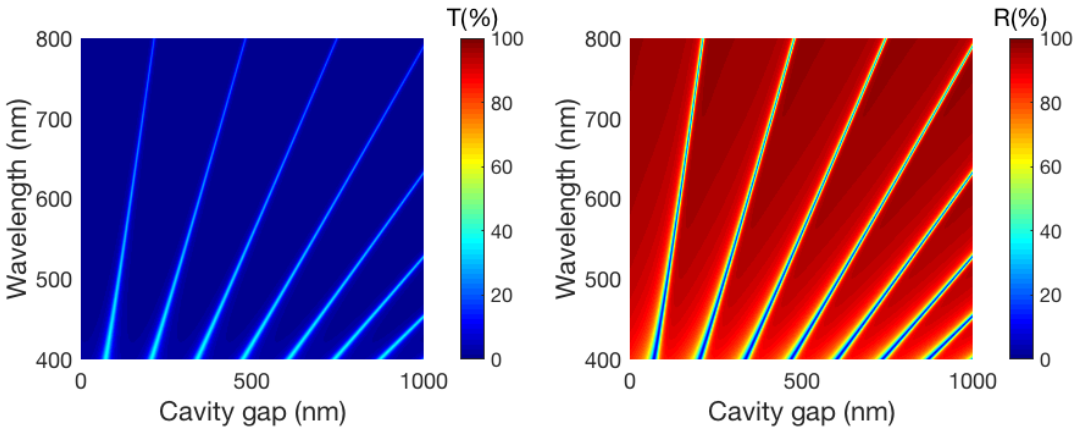

FIGURE 4.9: Cavity modes as a function of the slab material thickness of the structure shown in Figure 4.6. For this calculation the incident wave-vector is fixed at normal incidence. The other parameters are the same as those used in Figure 4.7.

A similar calculation can be performed for zero in-plane wave-vector, and varying the cavity length, or cavity gap, which can be controlled by varying the thickness of the dielectric in between the two silver mirrors. This calculation is shown in Figure 4.9. In this figure, the cavity gap varies from 0 to 1 μm, and the first seven cavity modes are observed. Their wavelengths depend linearly on the cavity gap.

4.2.3 Electric field profile of an optical microcavity

In this section the calculation of the electric field in a multilayer structure is described. In particular it is interesting to see how the electric field is distributed in the gap between the two mirrors of a microcavity, so we can design a structure where an excitonic material is placed at an antinode of the confined field to allow for light-matter interactions.

Figure 4.10 shows a multilayer structure, indicating the interfaces of the different layers as vertical lines. Multiple transmission and reflection wave-vectors are indicated as the horizontal arrows, which for simplicity are considered to

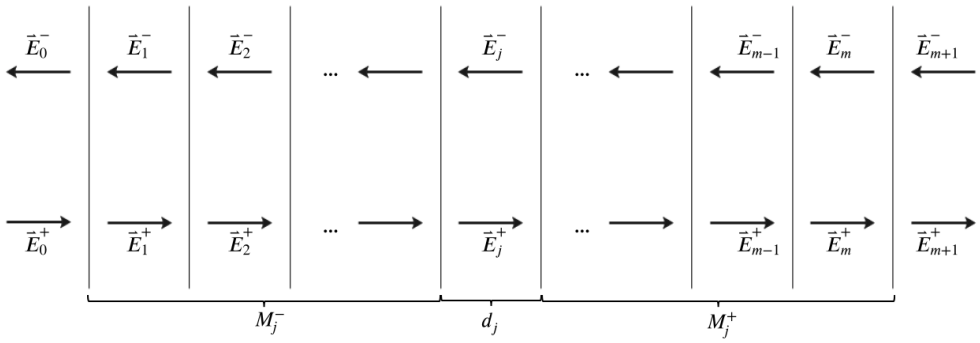

FIGURE 4.10: Multilayer structure indicating multiple normal incidence transmissions and reflections of wave-vectors.

propagate at normal incidence. The intensity of the electric field associated with light propagation at the different interfaces is indicated, and the direction of propagation is indicated by the superscript index +, for the propagation to the right, and - for the propagation to the left. The subscript index j indicates the j-th layer of the structure, which has a refractive index n_j, and a thickness d_j. Transmission and reflection coefficients are defined as in Equation 4.10, however, for clarity let us redefine these coefficients with the notation used in Figure 4.10

$$\begin{aligned} t &= \frac{|\vec{E}_{m+1}^+|}{|\vec{E}_0^+|}, \\ r &= \frac{|\vec{E}_0^-|}{|\vec{E}_0^+|}. \end{aligned} \tag{4.15}$$

To calculate the effective intensity of the electric field at any layer j, let us first define the total transfer matrix $\mathcal{M}_{tot}$ as a composition of the propagation matrix $\mathcal{P}_j$ multiplied by the transfer matrices $\mathcal{M}^-$ to the left and $\mathcal{M}^+$ to the right side of the j-th layer [77, 78],

$$\mathcal{M}_{tot} = \mathcal{M}_j^- \mathcal{P}_j \mathcal{M}_j^+, \tag{4.16}$$

where

$$\begin{bmatrix} \vec{E}_0^+ \\ \vec{E}_0^- \end{bmatrix} = \mathcal{M}_{tot} \begin{bmatrix} \vec{E}_{m+1}^+ \\ \vec{E}_{m+1}^- \end{bmatrix}. \tag{4.17}$$

The propagation matrix $\mathcal{P}_j$ is defined as

$$\mathcal{P}_j = \begin{bmatrix} exp(-i\beta_j) & 0 \\ 0 & exp(+i\beta_j) \end{bmatrix}, \tag{4.18}$$

where $\beta_j = k_0 n_j d_j cos(\theta_j)$, and $k_0 = 2\pi/\lambda_0$.

The matrices $\mathcal{M}_j^-$ and $\mathcal{M}_j^+$ are defined in terms of the interface matrix $\mathcal{I}$, and the propagation matrix $\mathcal{P}$ as follows

$$\begin{aligned} \mathcal{M}_j^- &= \left(\prod_{\nu=1}^{j-1} \mathcal{I}_{\nu-1,\nu} \mathcal{P}_\nu \right) \mathcal{I}_{j-1,j}, \\ \mathcal{M}_j^+ &= \left(\prod_{\nu=j+1}^{m} \mathcal{I}_{\nu-1,\nu} \mathcal{P}_\nu \right) \mathcal{I}_{m,m+1}, \end{aligned} \tag{4.19}$$

where

$$\mathcal{I}_{j-1,j} = \frac{1}{t_{j-1,j}} \begin{bmatrix} 1 & r_{j-1,j} \\ r_{j-1,j} & 1 \end{bmatrix}. \tag{4.20}$$

t and r are the Fresnel coefficients of transmission and reflection. By combining Equations 4.15 to 4.20 it is found that the electric field at the j-th layer can be expressed as

$$\vec{E}_j(x) = \frac{\mathcal{M}_{j,11}^+ e^{-i\beta_j(x)} + \mathcal{M}_{j,21}^+ e^{i\beta_j(x)}}{\mathcal{M}_{j,11}^- \mathcal{M}_{j,11}^+ e^{-i\beta_j} + \mathcal{M}_{j,12}^- \mathcal{M}_{j,21}^+ e^{i\beta_j}} \vec{E}_0^+, \tag{4.21}$$

which can be evaluated at any x-position inside the j-th layer. This position dependence comes from defining $\beta_j(x) = k_0 n_j (d_j - x) cos(\theta_j)$. To obtain the full

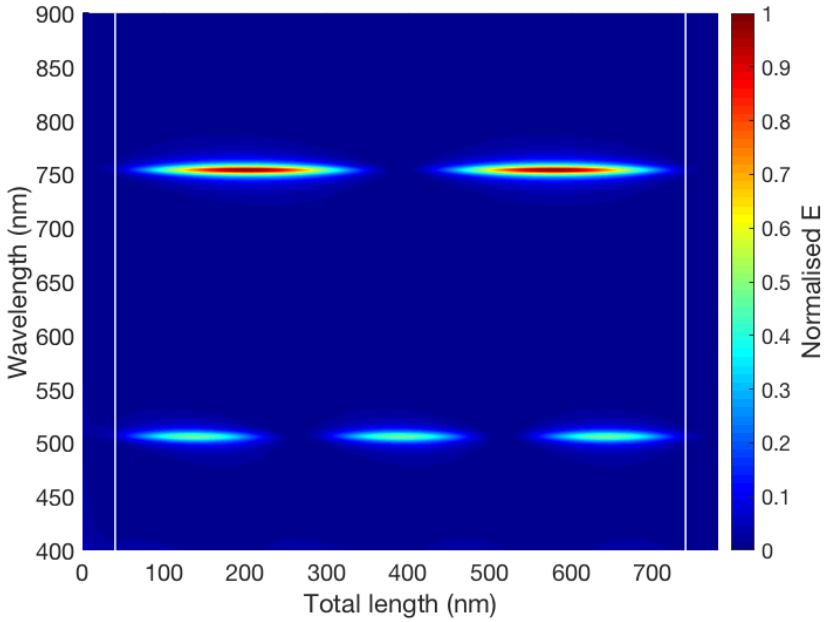

FIGURE 4.11: Electric field of the confined light in the multilayer structure shown in Figure 4.6. In this figure the second- and third-order cavity modes can be observed at wavelengths of 755 nm and 505 nm respectively.

electric field profile along the multilayer structure we can calculate Equation 4.21 for all the layers of the structure. For example, let us use the structure shown in Figure 4.6; the electric field is shown in Figure 4.11 for a range of wavelengths from 400 to 900 nm. For this calculation, a thickness of 40 nm has been used for the silver films. The dielectric slab in between the silver films is air and has a thickness of 700 nm. The total length of the structure is 780 nm. In this figure, it is observed that the field is confined at wavelengths of 755 nm and 510 nm, corresponding to the second- and third-order cavity modes. These modes can be tuned to any wavelength by modifying the thickness of the air gap between the two silver films.

The electric field profile can also be calculated for a single wavelength, as shown in Figure 4.12. In this figure, the real component of the refractive index of the different materials is also shown.

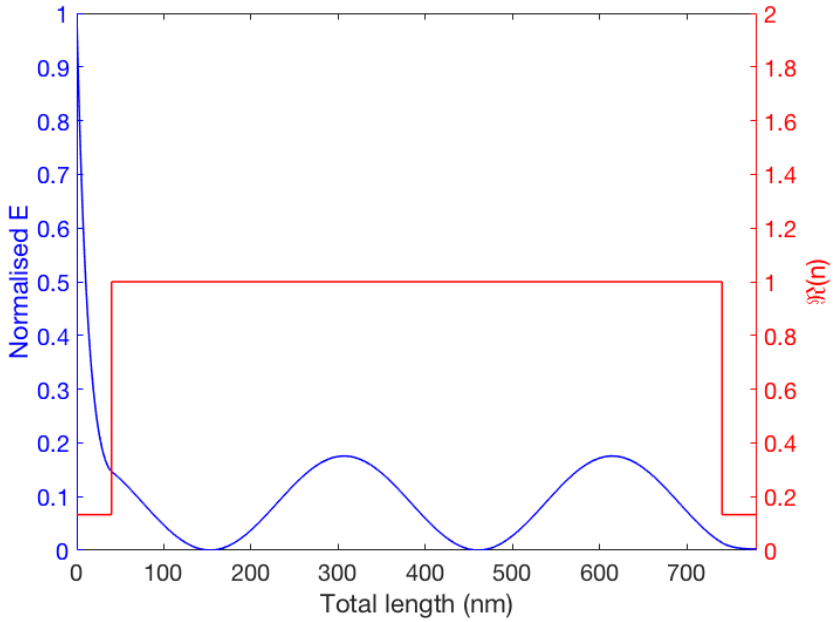

FIGURE 4.12: Electric field profile of the microcavity structure shown in Figure 4.6 calculated for a single wavelength (blue). The real component of the refractive index of the different materials in the microcavity structure is also shown (red).

From these calculations it is possible to determine the positions of the antinodes of the different cavity modes. For the second cavity mode the antinode is at a distance of 160 nm from the silver film for a wavelength of 755 nm. For example, WS_2 has an exciton transition at a wavelength of 622, so if we place this material at any position inside of the cavity there is no possibility for light-matter interaction, as there is no light field confined at that wavelength. To adjust the wavelength of the field confinement we can decrease the cavity length by 100 nm to bring the second cavity mode to a wavelength of 622 nm. Then we can place the WS_2 material at the antinode of the confined field which would allow for light-matter interaction forming exciton-polaritons. This interaction can be described classically using a coupled oscillator model.

4.3 Classical coupled oscillator model

4.3.1 Eigenmodes of the two coupled oscillators system

In this section, the dynamics of two coupled oscillators is discussed, and the concept of energy exchange is illustrated. Let us consider the system shown in Figure 4.13 in which there is friction characterised by the damping factor γ. The two blocks have, for simplicity, the same mass m. Their position functions are $y_1(t)$ for the first block on the left side, and $y_2(t)$ for the second block on the right side. The two blocks are attached to the side walls by springs of spring constant k_0, and they are coupled to each other by a spring of spring constant k. For the uncoupled system, $k = 0$, the two blocks have a natural frequency $\omega_0^2 = k_0/m$. The net force acting on each of the blocks is described in Equation (4.22):

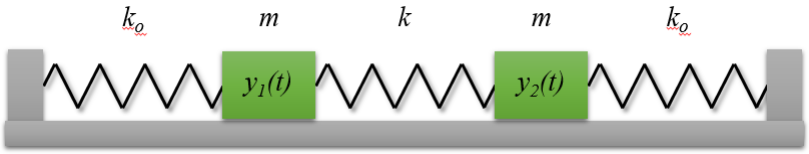

FIGURE 4.13: Two masses coupled by springs.

$$\begin{aligned} m\ddot{y}_1(t) &= -m\gamma\dot{y}_1(t) - k_0 y_1(t) + k(y_2(t) - y_1(t)), \\ m\ddot{y}_2(t) &= -m\gamma\dot{y}_2(t) - k_0 y_2(t) - k(y_2(t) - y_1(t)). \end{aligned} \tag{4.22}$$

From the latter equation we can write the equations of motion of the coupled system in matrix form as follows:

$$\begin{pmatrix} d_t^2 y_1 \\ d_t^2 y_2 \end{pmatrix} = \begin{pmatrix} -\gamma d_t - (\omega_0^2 - g^2) & g^2 \\ g^2 & -\gamma d_t - (\omega_0^2 - g^2) \end{pmatrix} \begin{pmatrix} y_1 \\ y_2 \end{pmatrix}, \tag{4.23}$$

where g is the coupling strength factor defined as $g^2 = k/m$. The operator $d_t = d/dt$ can be rewritten as $-i\omega$ for a harmonic position function of the form $y(t) = y_0 e^{-i\omega t}$, which best represents the time evolution of the blocks. In the

same way d_t^2 can be written as $-\omega^2$. Equation 4.23 then becomes

$$(M - I\omega^2)Y = 0, \tag{4.24}$$

where

$$\begin{aligned} M &= \begin{pmatrix} (\omega_0^2 + g^2) - i\gamma\omega & -g^2 \\ -g^2 & (\omega_0^2 + g^2) - i\gamma\omega \end{pmatrix}, \\ Y &= \begin{pmatrix} y_1 \\ y_2 \end{pmatrix}, \end{aligned} \tag{4.25}$$

and I is the 2×2 unitary matrix. In the coupling matrix M, the factor $i\gamma\omega$ can be approximated to a particular value of ω if γ is independent of the frequency; one particular value is $\omega = \omega_0$, therefore the complex factor becomes $i\gamma\omega_0$. Additionally, the coupling matrix M is equivalent to a matrix without the coupling factor g in the diagonal terms; the coupling matrix becomes [79, 80]

$$M = \begin{pmatrix} \omega_0^2 - i\gamma\omega_0 & -g^2 \\ -g^2 & \omega_0^2 - i\gamma\omega_0 \end{pmatrix}. \tag{4.26}$$

Equation 4.24 is an eigenvalue problem, where ω^2 are the eigenvalues of the matrix M, and Y are the eigenvectors. This equation has a solution if $det(M - I\omega^2) = 0$, from which the values of ω^2 can be calculated; these are:

$$\begin{aligned} \omega_+^2 &= \omega_0^2 - i\gamma\omega_0 + g^2, \\ \omega_-^2 &= \omega_0^2 - i\gamma\omega_0 - g^2. \end{aligned} \tag{4.27}$$

The solutions ω_- and ω_+ are new normal modes of the coupled oscillator system corresponding to a splitting of the natural frequency ω_0, where the splitting is $\Delta\omega = \omega_+ - \omega_- = 2g$.

4.3.2 Energy exchange between coupled oscillators

Another way of solving Equation 4.22 is by reducing the order of the coupled differential equation. To do this, new variables are defined: $u_1 = y_1$, $u_2 = \dot{y}_1$, $v_1 = y_2$, and $v_2 = \dot{y}_2$, so Equation 4.22 becomes

$$\begin{pmatrix} \dot{u}_1 \\ \dot{u}_2 \\ \dot{v}_1 \\ \dot{v}_2 \end{pmatrix} = \begin{pmatrix} 0 & 1 & 0 & 0 \\ -(\omega_0^2 + g^2) & -\gamma & g^2 & 0 \\ 0 & 0 & 0 & 1 \\ g^2 & 0 & -(\omega_0^2 + g^2) & -\gamma \end{pmatrix} \begin{pmatrix} u_1 \\ u_2 \\ v_1 \\ v_2 \end{pmatrix}. \tag{4.28}$$

In this method there is no need to know the form of the position functions, and these can be obtained by solving Equation 4.28. An evaluation of these position functions is shown in Figure 4.14 for different values of the coupling strength: (a) for $g = 0$, (d) for $g = 0.2\omega_0$, and (g) for $g = 0.4\omega_0$. For these calculations $\gamma = 0.01\omega_0$, and the initial positions are $y_1(t = 0) = 1$, $y_2(t = 0) = 0$, and both velocities are initially zero. The blue line corresponds to the time evolution of $y_1(t)$, and the red line to $y_2(t)$. It is observed in (a) that y_2 remains zero, while y_1 decays over time due to the damping factor γ. In (d) and (g) the oscillation of y_1 contributes to the oscillation of y_2 due to the two blocks being coupled. A similar calculation for a larger damping factor ($\gamma = 0.05\omega_0$) is shown in Figure 4.15; the values of the coupling strength are (a) $g = 0$, (d) $g = 0.2\omega_0$, and (g) $g = 0.4\omega_0$.

Equation 4.28 also represents an eigenvalue problem that can be solved in the same way as Equation 4.24. Using the new position functions $u_1(t)$ and $v_1(t)$, and their time derivatives, $u_2(t)$ and $v_2(t)$, the total energy of the system, which is the sum of the kinetic energy E_k and the potential energy E_p, can be

defined as

$$E_T(t) = E_k(t) + E_p(t), \tag{4.29}$$

where

$$E_k(t) = \frac{1}{2}mu_2^2(t) + \frac{1}{2}mv_2^2(t), \tag{4.30}$$

$$E_p(t) = \frac{1}{2}k_o u_1^2(t) + \frac{1}{2}k_o v_1^2(t) + \frac{1}{2}g^2 m(v_1(t) - u_1(t))^2. \tag{4.31}$$

Figure 4.14 shows an evaluation of the energy of the system for $\gamma = 0.01\omega_0$ and for different values of the coupling strength: (b) for $g = 0$, (e) for $g = 0.2\omega_0$, and (h) for $g = 0.4\omega_0$. In these calculations, the energy of the the first oscillator (blue lines) is obtained from $E(t) = \frac{1}{2}mu_2^2(t) + \frac{1}{2}k_o u_1^2(t)$, and for the second oscillator (red lines), $E(t) = \frac{1}{2}mv_2^2(t) + \frac{1}{2}k_o v_1^2(t)$. In (b) it is observed that the energy of the block represented by the red line, which initially has position zero, and zero speed, remains zero while the block represented by the blue line stores the total energy of the system. In (e) it is observed that in 100 seconds, the energy from the first block is completely transferred to the second one, and then it comes back to the first block. In this case $g = 0.2\omega_0$. This energy exchange happens a few times before the energy is lost due to the damping factor γ. When the coupling factor is larger, $g = 0.4\omega_0$, the energy is exchanged faster between the two blocks, as observed in (h).

A similar calculation is shown in Figure 4.15 for a larger damping factor, $\gamma = 0.05\omega_0$, and for different values of the coupling strength: (b) for $g = 0$, (e) for $g = 0.2\omega_0$, and (h) for $g = 0.4\omega_0$. By comparing the energy exchange between a system with low energy-loss factor (Figure 4.14(e)) with a system with high energy-loss factor (Figure 4.15(e)), we observe that increasing the loss factor reduces the energy exchange rate.

To compare the classical description of coupled oscillators with exciton-polaritons it is useful to look at the power spectrum of the coupled system.

4.3.3 Power spectrum from weak to strong coupling regimes

The power spectrum of the coupled system shown in Figure 4.13 can be obtained from the position functions $u_1(t)$ and $v_1(t)$, and provides information over the frequencies of the system. The power spectrum for each oscillator is defined as

$$P_u(\omega) = |F(u_1(t))|^2, \tag{4.32}$$

$$P_v(\omega) = |F(v_1(t))|^2, \tag{4.33}$$

where F is the Fourier transform of the position functions $u_1(t)$ and $v_1(t)$. The total power spectrum of the system is defined as

$$P_T(\omega) = P_u(\omega) + P_v(\omega). \tag{4.34}$$

An evaluation of the power spectrum of the coupled system is shown in Figure 4.14 for different values of the coupling strength: (c) for $g = 0$, (f) for $g = 0.2\omega_0$, and (i) for $g = 0.4\omega_0$.

In Figure 4.16 power spectrum maps for several values of g/ω_o are shown, where in (a) $\gamma = 0.01\omega_o$ and in (b) $\gamma = 0.05\omega_o$. In both cases $\omega_o = 1$Hz. The dependence of the peaks on the coupling strength g in these power spectrum maps can be well described by Equation 4.27.

The values of g that have physical meaning are $g \leq \omega_o$. The value of γ defines the broadening of the peaks in the power spectrum map. So even when the system is coupled the frequency splitting can not be observed for g/ω_o between 0 and 0.2 when $\gamma = 0.01\omega_o$. In the power spectrum we can observe the

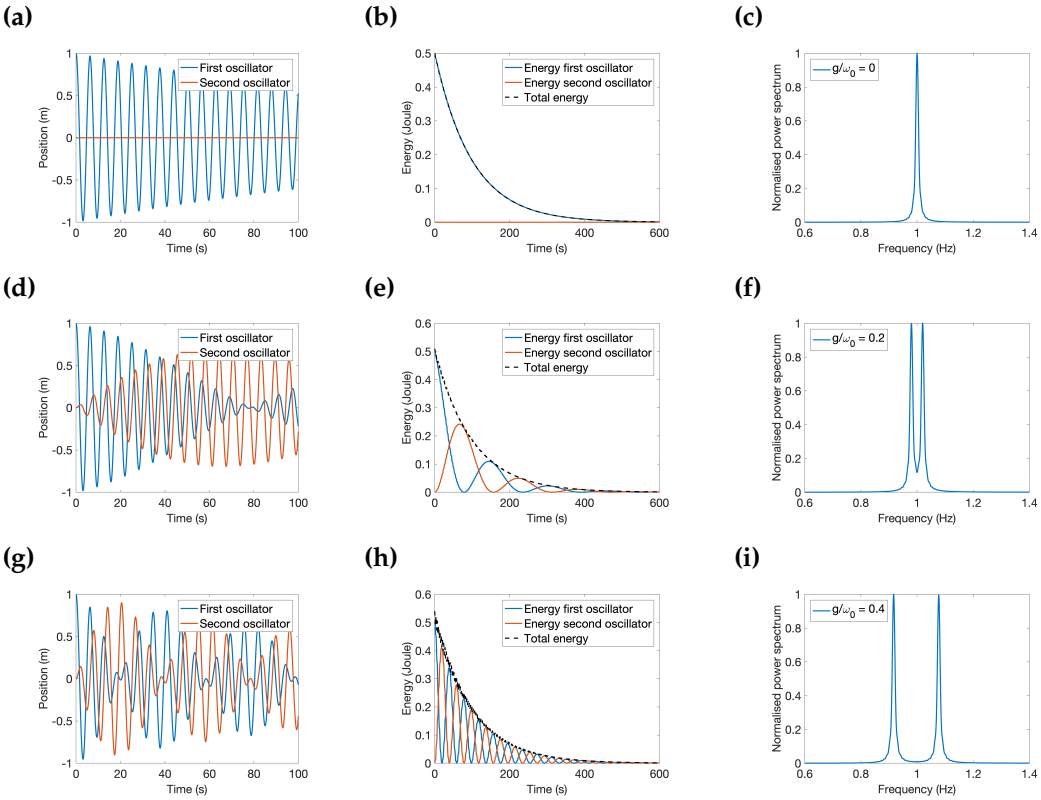

FIGURE 4.14: Evaluation of the position, energy, and power spectra of two coupled oscillators in the case of low energy losses. (a), (d), and (g) are the position functions of the two oscillators for different values of the spring constant of the spring that connects them. (b), (e), and (h) are the energies of each oscillator and the total energy, for different values of the spring constant. (c), (f), and (i) are the power spectra of the coupled oscillators for different values of the spring constant.

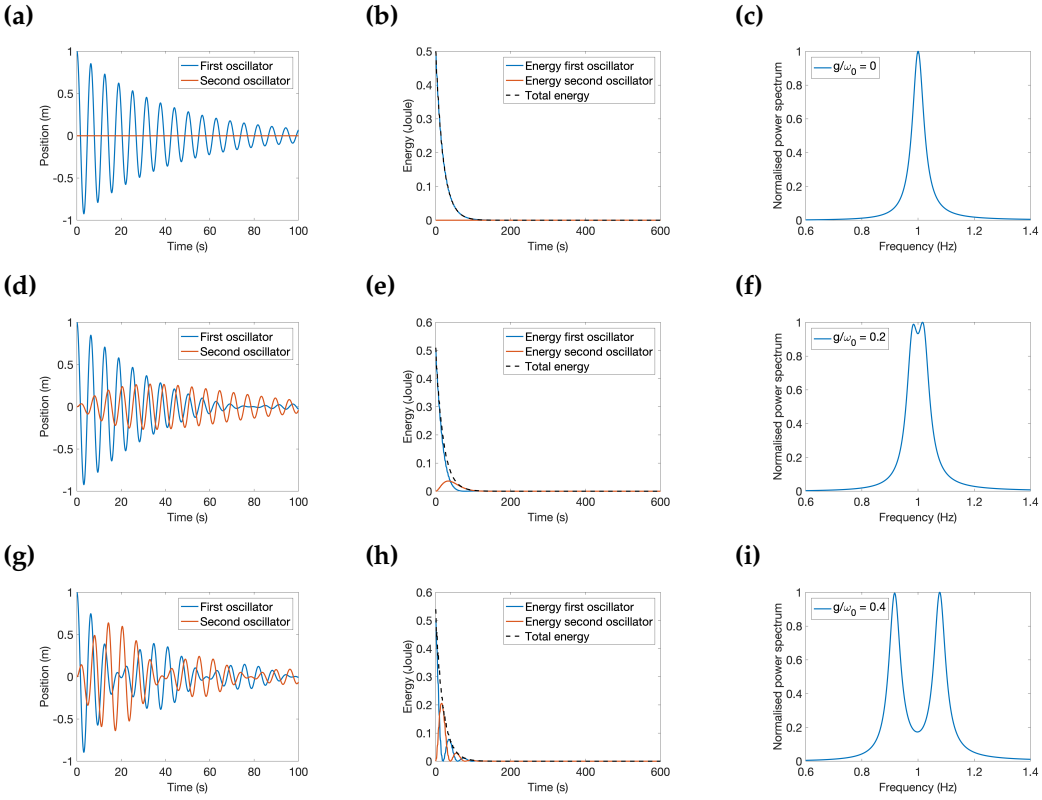

FIGURE 4.15: Evaluation of the position, energy, and power spectra of two coupled oscillators in the case of high energy losses. (a), (d), and (g) are the position function of the two oscillators for different values of the spring constant of a spring that connects them. (b), (e), and (h) are the energies of each oscillator, and both, for different values of the spring constant. (c), (f), and (i) are the power spectra of the coupled oscillator for different values of the spring constant that connects them.

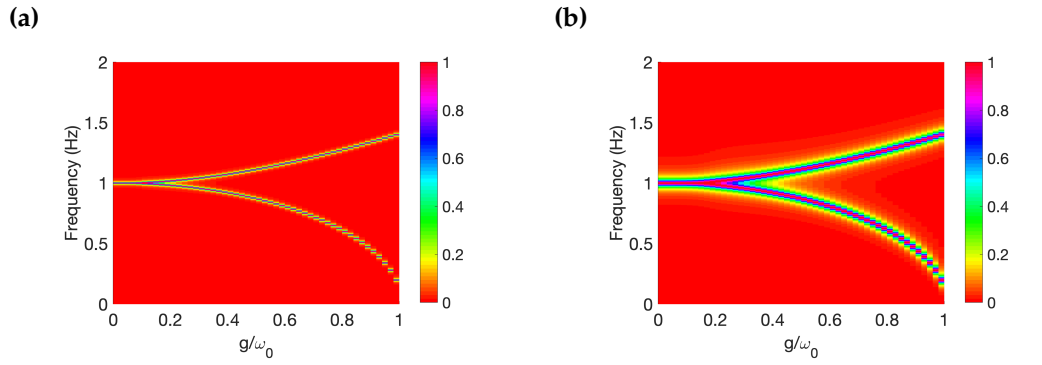

FIGURE 4.16: Calculations of the power spectrum as a function of the coupling strength for (a) an energy-loss factor of $0.01\omega_0$, and (b) an energy-loss factor of $0.05\omega_0$.

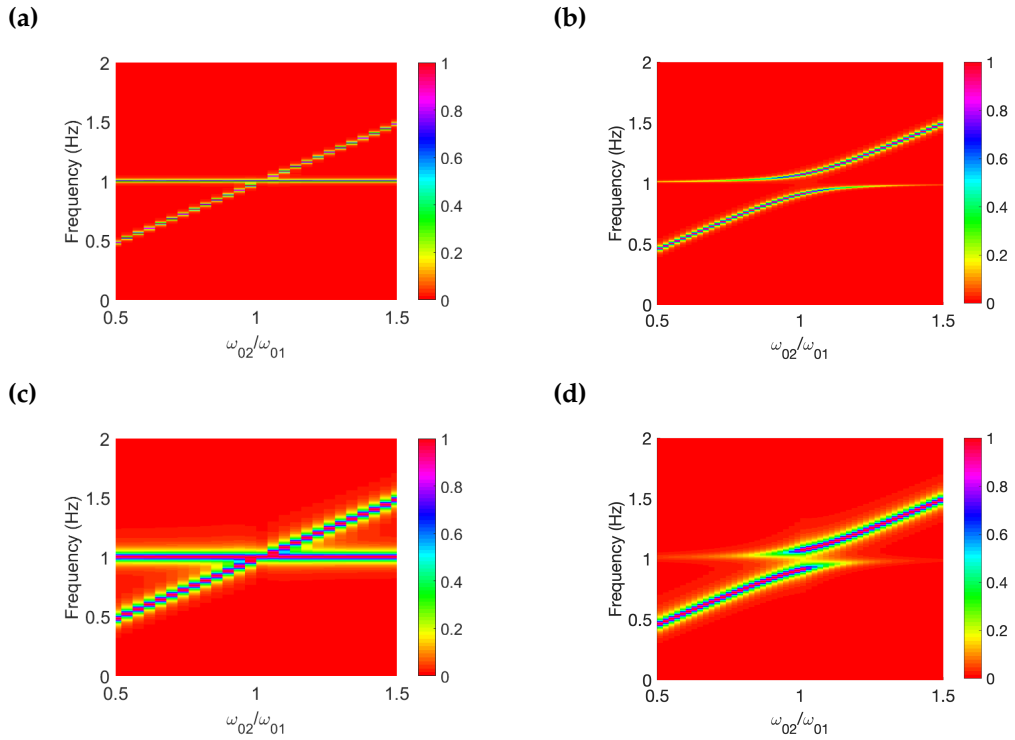

FIGURE 4.17: Calculations of the power spectrum as a function of the natural frequency of one of the oscillators in the coupled system. In (a) and (b) coupling factors of 0 and $0.5\omega_{01}$ are used respectively, with an energy-loss factor of $0.01\omega_{01}$. In (c) and (d) coupling factors of 0 and $0.5\omega_{01}$ are used respectively, with an energy-loss factor of $0.05\omega_{01}$.

splitting of the frequency of the system. The point at which the frequency splits in two defines the frontier between the weak and the strong coupling regimes. In the strong coupling regime a splitting of the normal mode is clearly resolved, while in the weak coupling regime there is no splitting of the normal mode.

In the weak coupling regime the energy loss due to the presence of damping is faster than the energy exchange between the two oscillators. On the other hand, under the strong coupling regime, the energy exchange is faster. The frequency splitting is the same effect described in the quantum formulation of the energy exchange between excitons and photons when they interact under the strong coupling regime.

In Figure 4.17, different power spectrum maps are shown where one oscillator has a fixed natural frequency while the other has a varying natural frequency. These calculations were obtained for different conditions of the coupling strength of the coupled oscillators and the energy-loss factor. Figure 4.17(a) shows the uncoupled case when the coupling strength is too small compared to the energy losses. Figure 4.17(b) shows the strongly coupled case, where a mode splitting is observed at the point where both oscillators have a similar natural frequency. Figures 4.17(c) and 4.17(d) are similar to the above mentioned cases, however, with a high energy-loss factor. In Figure 4.17(d) the mode splitting is barely visible compared to the splitting observed in Figure 4.17(b).

These calculations demonstrate that both the coupling strength and the energy-loss factor are crucial for the observation of a mode splitting. The mode splitting can be related to Rabi oscillations in an experiment with exciton-polaritons.

The applicability of the quantum mechanical equivalent to the classical coupled oscillator model described here has been under intense revision due to the eigenvalues of the coupling matrix being complex numbers. A Hamiltonian in matrix form that represents coupled harmonic oscillators with complex eigenvalues is non-Hermitian; intuitively, a complex spectrum of energies indicates that the coupled system would not be a real physical system that complies with the principles of physics such as the conservation of energy [81]. However, it has been recently found that a non-Hermitian Hamiltonian that conserves parity-time reversal ($\mathcal{PT}$) symmetry does have a real spectrum of energies [82]. Therefore the coupled oscillator model, after a few modifications to impose $\mathcal{PT}$-symmetry, is applicable to coupled quantum systems, such as exciton-polaritons.

4.4 $\mathcal{PT}$-symmetry of coupled quantum harmonic oscillators

$\mathcal{PT}$-symmetry is a composition of both the space-reversal ($\mathcal{P}$) and time-reversal ($\mathcal{T}$) symmetries. $\mathcal{P}$-symmetry applied to a matrix with momentum and position coordinates has the effect of changing the sign of the position function: $\mathbf{r} \rightarrow -\mathbf{r}$. $\mathcal{T}$-symmetry has the effect of changing the sign of the momentum function: $\mathbf{p} \rightarrow -\mathbf{p}$. Another effect of the $\mathcal{T}$-symmetry is the change of sign of i in the time-dependent Schrödinger equation $i\hbar\partial_t\Psi = \mathcal{H}\Psi$, where the time operator ∂_t is associated with the complex factor i.

A Hamiltonian of the form

$$\mathcal{H} = \begin{pmatrix} a - ib & g \\ g & a - ib \end{pmatrix}, \tag{4.35}$$

does not conserve $\mathcal{PT}$-symmetry: $(\mathcal{PT})\mathcal{H}(\mathcal{PT})^{-1} \neq \mathcal{H}$. However, if we change the sign of one of the complex numbers in the diagonal terms, the Hamiltonian $\mathcal{H}$ becomes $\mathcal{PT}$-symmetric, and yet it is non-Hermitian [83]:

$$\mathcal{H} = \begin{pmatrix} a + ib & g \\ g & a - ib \end{pmatrix}. \tag{4.36}$$

As mentioned before this non-Hermitian, $\mathcal{PT}$-symmetric Hamiltonian has a real spectrum of energies. Its eigenvalues are $E = a \pm \sqrt{g^2 - b^2}$. However, there is another condition for these eigenvalues to be real numbers; g must be larger than b. This condition defines the criteria for the weak and strong coupling regimes in the two coupled oscillators model.

4.5 Criteria for weak and strong coupling regimes

Different criteria can be found in literature for the description of the strong and the weak coupling regimes. The interpretation of the strong coupling regime relies on the energy exchange between two coupled oscillators. In this regime the energy flows from one oscillator to the other and back; this energy exchange happens many times before the total energy is dissipated. In the weak coupling regime, the energy flows from one oscillator to the other and then it is lost; the energy is dissipated before flowing back to the first oscillator. What it is not completely clear is what the limit is between the strong and the weak coupling regimes. Any criteria require some approximation to the mathematical formula, which I describe in the next paragraphs.

4.5.1 First criterion

This criterion, probably the most widely used, is the one reported by Savona *et al.* [84]. In this report, the coupling matrix for exciton-polaritons has the form of Equation 4.35, with a being the natural frequency of cavity photons and excitons ($a = \{\omega_c, \omega_{ex}\}$), and b the energy-loss factor, which is different for cavity photons and excitons ($b = \{\gamma_c, \gamma_{ex}\}$). With these changes the coupling matrix becomes

$$\mathcal{H} = \begin{pmatrix} \omega_c - i\gamma_c/2 & -g \\ -g & \omega_{ex} - i\gamma_{ex}/2 \end{pmatrix}. \tag{4.37}$$

The eigenvalues of the coupling matrix are

$$\omega_\pm = \frac{1}{2}(\omega_c + \omega_{ex}) - \frac{1}{4}i(\gamma_c + \gamma_{ex}) \pm \frac{1}{4}\sqrt{(4g)^2 - (2i(\omega_c - \omega_{ex}) + \gamma_c - \gamma_{ex})^2}, \tag{4.38}$$

which at resonance between cavity photons and excitons (i.e. $\omega_c = \omega_{ex}$) become

$$\omega_{\pm} = \omega_c - \frac{1}{4}i(\gamma_c + \gamma_{ex}) \pm \frac{1}{4}\sqrt{(4g)^2 - (\gamma_c - \gamma_{ex})^2}. \tag{4.39}$$

As discussed before, the coupling matrix in Equation 4.37 is non-Hermitian and it has broken $\mathcal{PT}$-symmetry, therefore its eigenvalues have a complex component which is independent of the value of the coupling factor g. However, the splitting $\Delta\omega$ of the modes which characterises the rate of energy exchange (or the Rabi cycle) between cavity photons and excitons can still be a real number.

In Equation 4.39 if $(4g)^2 - (\gamma_c - \gamma_{ex})^2 > 0$ then

$$\Delta\omega = \omega_+ - \omega_- = \frac{1}{2}\sqrt{(4g)^2 - (\gamma_c - \gamma_{ex})^2} \in \mathbb{R}, \tag{4.40}$$

and the splitting is purely real; in this case, this regime is called the strong coupling regime. If $(4g)^2 - (\gamma_c - \gamma_{ex})^2 < 0$ then

$$\Delta\omega = \omega_+ - \omega_- = \frac{1}{2}i\sqrt{(\gamma_c - \gamma_{ex})^2 - (4g)^2} \in \mathbb{C}. \tag{4.41}$$

In this case the splitting is purely imaginary; this is the weak coupling regime.

4.5.2 Second criterion

In this criterion we impose an unbroken $\mathcal{PT}$-symmetry on the coupling matrix in Equation 4.37. For this we change the sign of one of the energy-loss factors and we set $\gamma = \gamma_c = \gamma_{ex}$; with these changes we obtain

$$\mathcal{H} = \begin{pmatrix} \omega_c + i\gamma/2 & -g \\ -g & \omega_{ex} - i\gamma/2 \end{pmatrix}. \tag{4.42}$$

The eigenvalues of this matrix at the resonant condition, are

$$\omega_{\pm} = \omega_0 \pm \frac{1}{4}\sqrt{(4g)^2 - (2\gamma)^2}, \tag{4.43}$$

and the mode splitting is

$$\Delta\omega = \omega_+ - \omega_- = \frac{1}{2}\sqrt{(4g)^2 - (2\gamma)^2} \in \mathbb{R} \tag{4.44}$$

for the strong coupling regime when $(4g)^2 - (2\gamma)^2 > 0$, and

$$\Delta\omega = \omega_+ - \omega_- = \frac{1}{2}i\sqrt{(2\gamma)^2 - (4g)^2} \in \mathbb{C} \tag{4.45}$$

for the weak coupling regime when $(4g)^2 - (2\gamma)^2 < 0$.

4.5.3 Third criterion

In real exciton-cavity systems, the energy-loss factors for excitons and cavity photons are usually different. This means that we can not impose an unbroken $\mathcal{PT}$-symmetry to the Hamiltonian as described in Equation 4.42, however, a good approximation would be to introduce the average of the energy-loss factors in this Hamiltonian; $\gamma_{av} = (\gamma_c + \gamma_{ex})/2$, so the Hamiltonian of the coupled system becomes

$$\mathcal{H} = \begin{pmatrix} \omega_c + i\gamma_{av}/2 & -g \\ -g & \omega_{ex} - i\gamma_{av}/2 \end{pmatrix}, \tag{4.46}$$

and this Hamiltonian is $\mathcal{PT}$-symmetric. The eigenvalues of this matrix at the resonant condition are

$$\omega_{\pm} = \omega_0 \pm \frac{1}{4}\sqrt{(4g)^2 - (\gamma_c + \gamma_{ex})^2}, \tag{4.47}$$

where γ_{av} has been replaced by its constituents; $\gamma_{av} = (\gamma_c + \gamma_{ex})/2$. The mode splitting is

$$\Delta\omega = \omega_+ - \omega_- = \frac{1}{2}\sqrt{(4g)^2 - (\gamma_c + \gamma_{ex})^2} \in \mathbb{R} \tag{4.48}$$

for the strong coupling regime when $(4g)^2 - (2\gamma_{av})^2 > 0$, and

$$\Delta\omega = \omega_+ - \omega_- = \frac{1}{2}i\sqrt{(\gamma_c + \gamma_{ex})^2 - (4g)^2} \in \mathbb{C}. \tag{4.49}$$

for the weak coupling regime when $(4g)^2 - (2\gamma_{av})^2 < 0$.

This criterion is perhaps the most intuitive when performing analysis of experimental data. The mode splitting $\Delta\omega$ is related to the peak splitting in absorption spectroscopy measurements (and transmission/reflection measurements), where the energy-loss factors are related to the full-width-half-maximum (*fwhm*) of the absorption peaks of uncoupled excitons and cavity photons. Comparing the peak splitting with the average of the peak widths can be interpreted as a resolution criterion; if the peak splitting is larger than the average of the uncoupled peak widths, then the splitting is measurable, and the system is in the strong coupling regime. Otherwise, the splitting is not measurable and the system is in the weak coupling regime.

In Figure 4.18 there is an evaluation of the eigenvalues as a function of the coupling strength g for the three criteria described in Equations 4.39, 4.43, and 4.47. These correspond respectively to the red, blue, and green lines in both panels of Figure 4.18, where panel (a) is the real component of the eigenvalues, and (b) the complex component. The parameters used for these calculations are $\gamma_c = 0.01\omega_0$, and $\gamma_{ex} = 0.02\omega_0$. In this figure, the limit between the weak and strong coupling regimes occur at different values of the coupling strength g for the three different criteria. The first criterion for the strong coupling regime [84]

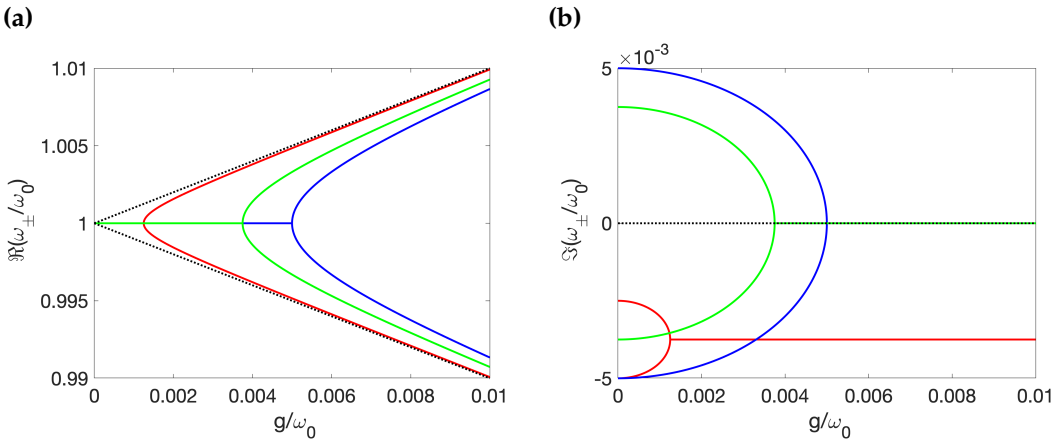

FIGURE 4.18: Evaluation of Eqs. 4.39 (red line), 4.43 (blue line), and 4.47 (green line) as a function of the coupling strength g, for $\omega_c = 1$, $\gamma_c = 0.01$, $\gamma_{ex} = 0.02$. The black line correspond to Eq. 4.39 for $\gamma_c = \gamma_{ex} = 0$. (a) is the real component of $\omega_\pm$, (b) is the imaginary component.

requires a smaller value of g than the other criteria. In this criterion it can also be observed that for any value of $g > 0$ there is always a complex component in the eigenvalues whereas for the other criteria whenever the system is in the strong coupling regime, the complex component of the eigenvalues vanishes. The black dashed lines are an evaluation of Equation 4.39 in absence of any losses, for which the system is in the strong coupling regime for any value of $g > 0$.

As the three criteria described are, to some extent, approximations of a real system used in measurements, it is still yet to be decided which criteria is best for each experiment. One important approximation made here is that any external influence is not included in the coupling matrices; in real experiments there is always an external contribution to the system. This could be, for example, the illumination setup used for optical measurements. An important open question is how is the energy exchange at the limit between weak and strong coupling regimes, and how different is this energy exchange depending on the different criteria used to determine this limit.

4.6 Exciton and photon fraction in exciton-polaritons

As described before, exciton-polaritons are a mixture of excitons and photons formed in a confined light field. In this section, I describe a method to calculate the weight factors of photons and excitons that are present in the mixture, known as the Hopfield coefficients [85], however in this case I use a $\mathcal{PT}$-symmetric coupling matrix. These weight factors range from 0 to 1 for each component, photons and excitons, such that the sum of both is equal to 1. Let us first describe a matrix approach to calculate the dispersion relation of exciton-polariton states.

$$\hat{\mathcal{H}}\psi = E\psi. \tag{4.50}$$

Equation 4.50 is the Schrödinger equation that describes the energy E of a Hamiltonian $\hat{\mathcal{H}}$ given a wave function ψ. This equation can be solved as an eigenvalue problem if we represent the Hamiltonian in matrix form, in this way ψ becomes eigenvectors of the matrix and E becomes the eigenvalues.

For exciton polaritons, we can use the interaction matrix of Equation 4.46 that describes the coupling between two resonators; using this matrix, the Schrödinger equation for exciton-polaritons becomes

$$\begin{pmatrix} E_c + i\gamma_{av} & V \\ V & E_{ex} - i\gamma_{av} \end{pmatrix} \begin{pmatrix} \psi_1 \\ \psi_2 \end{pmatrix} = E \begin{pmatrix} \psi_1 \\ \psi_2 \end{pmatrix}. \tag{4.51}$$

In this equation, E_c and E_{ex} are functions that describe the dependence of the energy of a cavity mode and an exciton transition respectively on some variable. This variable can be anything related to the energy through a causality relation: temperature, cavity length, wave-vector, etc. ψ_1 and ψ_2 are components of ψ. γ_{av} is the average of the energy-loss factors for cavity photons and excitons; $\gamma_{av} = (\gamma_c + \gamma_{ex})/2$.

The energy dispersion of the Fabry-Pérot microcavity modes is defined as

$$E_c = \frac{\hbar c}{n}\sqrt{k_{||}^2 + \left(\frac{\pi m}{L_c}\right)^2},$$

where c is the speed of light in vacuum, n the refractive index of the interior of the microcavity, $k_{||}$ is the in-plane component of the wave-vector k, m is an integer that defines the mode-order of the microcavity, and L_c is the cavity length. For a particular cavity mode (fixed m), E_c depends on $k_{||}$ and L_c. The energy of an exciton transition does not depend on either of the two variables mentioned for a cavity mode. In this case, if we solve Equation 4.51 as a function of $k_{||}$ or L_c, E_{ex} is introduced as a constant function.

The routine for solving Equation 4.51 consists of: first, finding analytical expressions for the light and the exciton modes; second, solving Equation 4.51 as an eigenvalue problem to find the eigenvectors $\psi = (\psi_1, \psi_2)$, and the eigenvalues E. This routine can be applied to any light field: plasmonic arrays, whispering gallery modes, photonic crystals, etc. And it can also be extended to any number of components, i.e. one cavity mode coupled to two different exciton transitions, which would be described as a 3×3 coupling matrix.

The last term that we need to define to solve Equation 4.51 is the coupling strength V between the two modes E_c and E_{ex}. This term, which is related to the Rabi oscillations of exciton-polaritons, can be found experimentally if it is unknown. Once V is inserted into Equation 4.51 we can find the eigenvectors and eigenvalues of the system, which provide information of the physics in the interaction between cavity photons and excitons.

The components of the eigenvectors (ψ_1, ψ_2) satisfy the normalisation relation $|\psi_1|^2 + |\psi_2|^2 = 1$. The values $|\psi_1|^2$ and $|\psi_2|^2$ are the Hopfield coefficients [85], which represent the photon and exciton fraction of the polariton bands.

Figure 4.19 shows calculations from solving Equation 4.51. (a), (c), and (e) are calculations for a cavity mode as a function of the cavity length L_c where the wave-vector is fixed at $k_{||} = 0$. (b), (d), and (f) are calculations for a cavity mode as a function of the in-plane wave-vector $k_{||}$ for a fixed cavity length. Figure 4.19(a) shows the eigenvalues of the coupling matrix in Equation 4.51. In this figure we can identify the exciton mode as a constant value, the cavity mode, which is a function of the cavity length, and the eigenvalues labelled as upper and lower bands. These bands are the exciton-polariton bands, where upper and lower refer to the energy values at the anti-crossing point between the bare exciton and cavity modes. Figure 4.19(c) shows the Hopfield coefficients of the lower polariton band, where it can be seen that for small values of the cavity length, the lower polariton band is mostly composed of excitons. At the anti-crossing point between the exciton and the cavity mode the lower polariton band is composed equally of excitons and photons. For large values of the cavity length the lower polariton band is mostly composed of cavity photons. Figure 4.19(e) shows the exciton and photon fraction of the upper polariton band where for small values of the cavity length this band is mostly composed of cavity photons. At the anti-crossing point there is the same photon/exciton fraction as in the lower polariton band. For large values of the cavity length the upper polariton band is mostly composed of excitons.

It can be proven that at the anticrossing point, the value of γ_{av} does not modify the Hopfield coefficients, but it does modify them away from the anti-crossing point.

Figure 4.19(b) shows the dispersion diagram of exciton-polaritons as a function of the in-plane wave-vector for a fixed cavity length. As in Figure 4.19(a), two polariton bands are formed, and their exciton/photon composition follows the same analysis as in Figures 4.19(c) and (e).

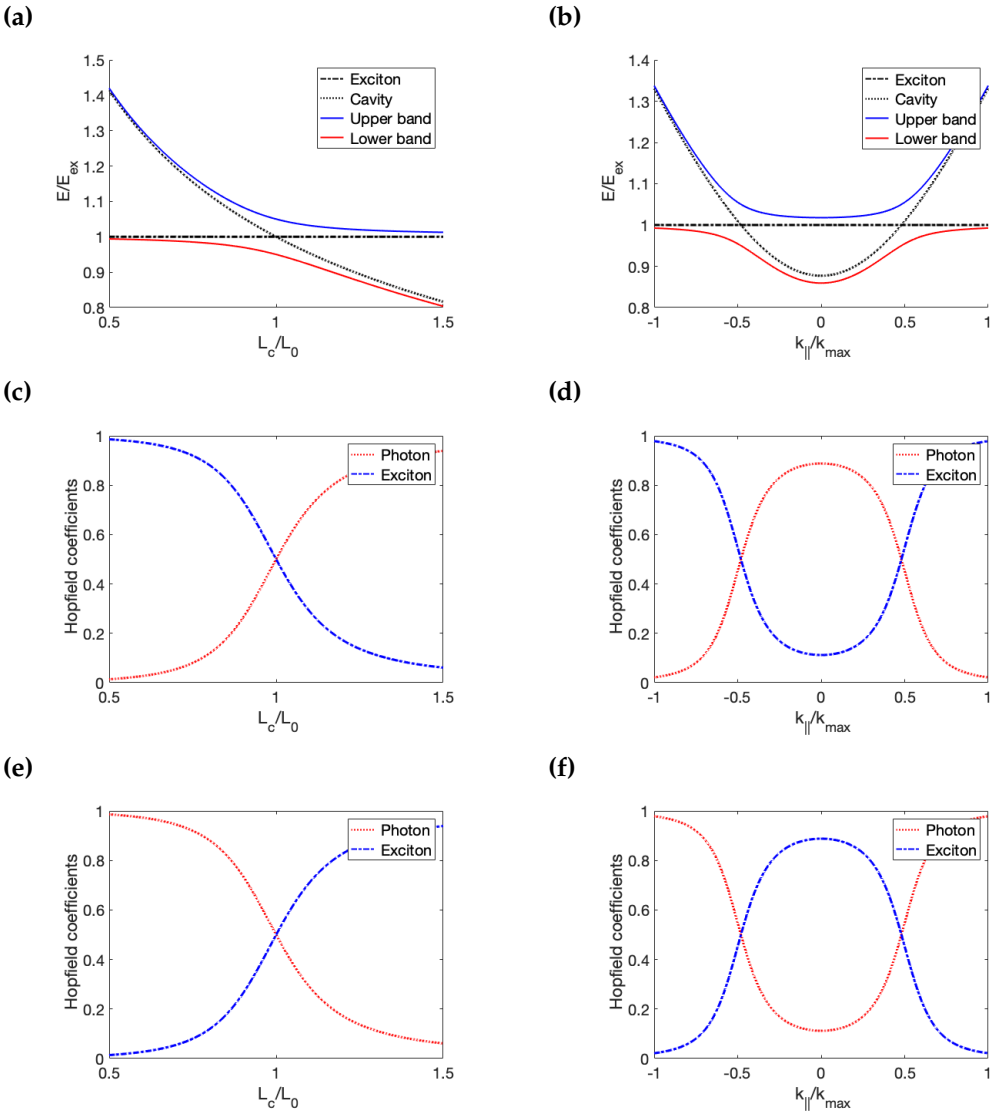

FIGURE 4.19: Solutions of Equation 4.51 for (a), (c), (e) a cavity with a tuneable cavity length and fixed normal wave-vector, and (b), (d), (f) a cavity with a fixed cavity length and a varying wave-vector. (a) and (b) show the eigenvalues of Equation 4.51, (c) to (f) show the Hopfield coefficients for (c) and (d) the lower polariton bands, and (e) and (f) the upper polariton bands.

This analysis can additionally be used to extract the Rabi splitting from experimental measurements. In an experiment consisting of transmission measurements as a function of the cavity length or the in-plane wave-vector, where an anti-crossing is observed indicating the formation of exciton-polaritons, the polariton bands obtained from Equation 4.19 can be fit to the measurements. The fitting routine can provide the coupling strength V, which should be set as a free parameter. Along with this, we can also obtain the experimental values of the Hopfield coefficients.

4.7 Summary

This chapter introduced the theory used for calculations relevant to the novel results presented in Chapters 5 and 6. The Lorentz model for the permittivity of metals, dielectrics, and excitonic materials was described. This permittivity is a fundamental parameter for the modelling of transmission/reflection of white light in a multilayer structure. The calculation of the optics of a multilayer structure was described, which is fundamental for the design of devices used in the study of exciton-polaritons. Such study is presented in Chapters 5 and 6.

An essential theory for the study of exciton-polaritons is the coupled oscillator model, which was also described in this chapter, with special attention given to the criteria for the strong and weak coupling regimes. In the strong coupling regime there is an effective energy exchange between excitons and cavity photons, and it is faster than the overall energy dissipation. In the weak coupling regime there is no energy exchange; the energy is transferred from one oscillator to the other and then it is dissipated. However, it is not clear what the limit between the strong and the weak coupling regimes is. I discussed three different criteria often found in literature to distinguish between strong

and weak coupling regimes. However, mathematical approximations must be made in any criteria which distance the theory from the results of real systems used in experiments. Also, multiple hybridisation requires a more in-depth analysis which I do not include here. Such analysis would be relevant for systems combining two different exciton species with one cavity mode, such as the one presented in Chapter 6. This system can be modelled as three coupled oscillators using a 3x3 coupling matrix. For this case, there is no coupling matrix representing the three oscillators that conserves $\mathcal{PT}$-symmetry, and any coupling matrix for three oscillators will be non-Hermitian. So it is yet to be discussed to what extent the coupled oscillator model is applicable, through what approximations, and what new physics can be found.

Chapter 5

Electrical control of exciton-polaritons

This study demonstrates control over light-matter coupling at room temperature combining a field effect transistor (FET) with a tuneable optical microcavity. The microcavity-FET comprises a monolayer tungsten disulfide WS_2 semiconductor which was transferred onto a hexagonal boron nitride flake that acts as a dielectric spacer and as an electric insulator in the FET. In the tuneable microcavity strong coupling between excitons in the monolayer WS_2 and cavity photons can be tuned by controlling the cavity length, which was achieved with excellent stability, choosing from the second to the fifth order of the cavity modes. Once the strong coupling regime is achieved the oscillator strength of excitons in the semiconductor material is modified by controlling the free electron carrier density in the conduction band of the WS_2. This enables strong Coulomb repulsion between free electrons, which reduces the oscillator strength of excitons until the Rabi splitting completely disappears. The charge carrier density was controlled from 0 up to 3.2×10^{12} cm^{-2}, and over this range the Rabi splitting varies from a maximum value that depends on the cavity mode chosen, down to zero, so the system spans the strong to weak coupling regimes.

5.1 Introduction

To investigate both tuneability and control over the light-matter coupling of exciton-polaritons a previously reported design was used [74]. This design consists of a tuneable Fabry-Pérot microcavity with a TMD-based transistor embedded within. The chosen TMD material, tungsten disulfide (WS_2), exhibits the largest oscillator strength and the smallest damping factor among TMDs of chemical composition MX_2 (M = W, Mo, X = S, Se) [51]. These properties make WS_2 the optimum semiconductor TMD for strong coupling measurements of exciton-polaritons at visible frequencies, at room temperature, and in microcavities of moderate quality factor ($Q \approx 100$). In this device, an increase of the free carrier density in the WS_2 monolayer produces a strong Coulomb screening of the free electrons that populate the conduction band [86]. This screening reduces the oscillator strength of neutral excitons, which therefore weakens the coupling strength of exciton-polaritons [63].

This study significantly extends previous investigations [71]; a saturation regime of the light-matter coupling strength, characterised by the vacuum Rabi splitting, was reached by applying sufficient gate voltages. For sufficiently negative values of the gate voltage, the Rabi splitting saturates to its maximum value, while for sufficiently positive values of the gate voltage (high electron carrier density) the Rabi splitting was eliminated. These observations allow for explaining the functional dependence of the Rabi splitting on the gate voltage and to probe the nature of the Coulomb screening process.

In this research project a WS_2 microcavity was studied in which the TMD excitons are strongly coupled to microcavity modes, and these modes can be chosen from the third-order to the fifth-order by controlling the cavity length

in a tuneable way. The dependence of the Rabi splitting on the electrically-controlled density of free electrons was observed; the density of free electrons ranges from 0 up to $3\times10^{12}\ cm^{-2}$. Over this range, the Rabi splitting varies from a maximum value (which depends on the order of the chosen cavity mode) down to zero so that the hybrid system spans the strong to weak coupling regimes.

5.2 WS_2-based field effect transistor

The WS_2-based field effect transistor was studied first without a microcavity. The transistor consisted of a Van der Waals heterostructure composed of WS_2 placed on top of a hexagonal boron nitride (hBN) flake. The fabrication procedure for the heterostructure is described in detail in the supporting information of reference [50]. The WS_2/hBN heterostructure was placed on a silver (Ag) film, which acts as a microcavity mirror (bottom mirror) as well as the gate contact of the transistor, while WS_2 was kept as a ground contact (see Figure 5.1(a) and (b)).

The hBN flake plays an essential role in both the optical and the electronic performance of the transistor. For the optics hBN acts as a dielectric spacer; the thickness of hBN determines the position at which the WS_2 flake is placed in the microcavity, therefore the confined field intensity which TMD excitons interact with. For electronics hBN acts as a dielectric insulator ($\epsilon \sim 3-4$)[87], which prevents electrons from leaking between the WS_2 and the Ag gate electrode. Transmission measurements were performed through this device, and the evolution of the minimum in transmission associated with the WS_2 exciton was studied for different values of the gate voltage. Figure 5.1(a) shows a microscope image of the top view of the WS_2 transistor; coloured lines are

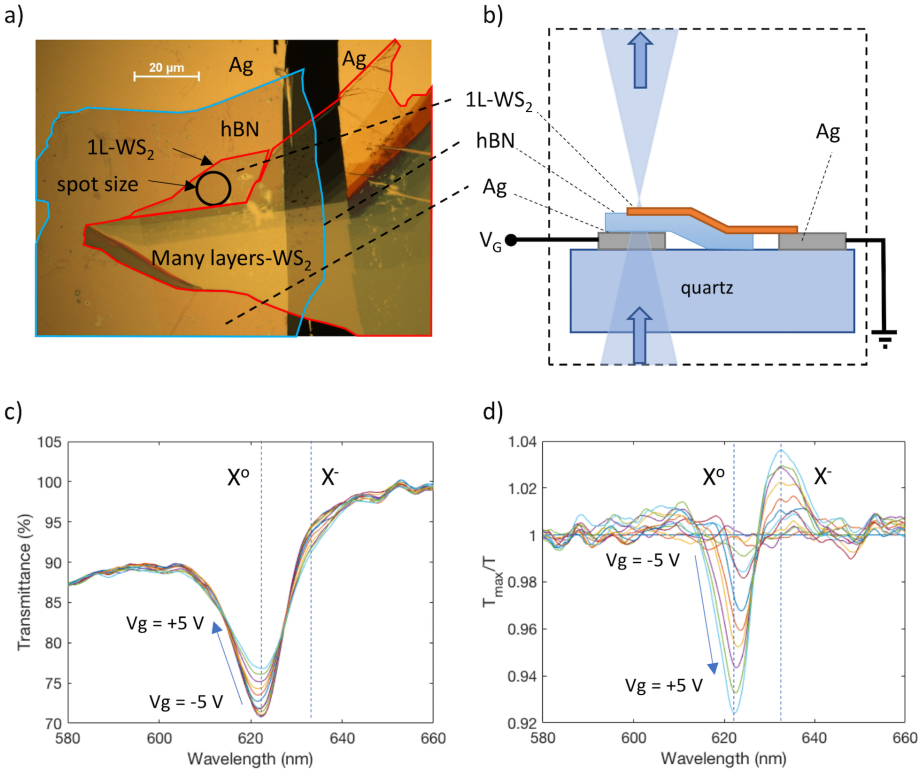

FIGURE 5.1: (a) Top view microscope image of the WS_2/hBN/Ag heterostructure on quartz. Coloured lines indicate flake edges: blue for hBN, and red for WS_2. (b) Schematic cross-section of the WS_2-based transistor. Arrows indicate the propagation direction of the white light. (c) White light transmittance of the 1L-WS_2 for different gate voltages from -5 to +5 V. The positions of neutral excitons X^0 and negatively charged excitons, or negative trions X^-, are indicated. (d) Data shown in (c) normalised to the transmittance spectrum for $V_G = -5$ V, which is the reference T_{max}. This plot shows how the transmission for both the neutral excitons and the negative trions change for the different values of gate voltage.

drawn to indicate the edges of the different materials of the heterostructure, red for WS_2, and blue for hBN. The spot size for light collection is also indicated on the figure, which has a diameter of 10 μm. The area of interest is a monolayer WS_2 (1L-WS_2) electrically in contact with a multilayer flake (see figure 5.1(a)) allowing for a minimised contact barrier height between the monolayer and the multilayer TMD. The monolayer and the multilayer WS_2 are in contact side-by-side. The gate voltage is applied to one Ag electrode (bottom mirror) while keeping the WS_2 grounded through a second Ag electrode. In this configuration the application of a positive voltage between the two Ag electrodes increases the density of free charge carriers that populate the conduction band of the WS_2 monolayer, while the application of a negative voltage removes any doping of free charge carriers, leaving the sample electrically neutral in the range of negative voltages applied. Because of the n-type character of the WS_2 hole doping was not possible at the maximum range of gate voltages.

In Figure 5.1(b) a schematic side view of the sample is shown in which arrows indicate the direction of propagation of the transmitted light, and the position of the electrical contacts is also indicated. White light transmission spectra were collected for different values of the gate voltage V_G, as shown in Figure 5.1(c). In this figure a transmittance minimum is observed at a wavelength of 622 nm, and it is associated with the neutral exciton transition of the 1L-WS_2, labelled X^0. In this figure, the appearance of an asymmetric broadening is also observed, and this is associated with the weak transmittance of negatively charged excitons [62], or negative trions, at a wavelength of 632 nm, which is labelled as X^-. A weakening in the transmission minimum associated with the neutral excitons is observed as the gate voltage sweeps from -5 V to +5 V. The feature associated with the negative trions strengthens in the range of voltages applied. To clarify this observation, the change in the transmission

associated with X^o and X^- as a function of V_G was extracted. These data are shown in Figure 5.1(d), where values below one indicate how much the transmission is reduced in strength, while values above one indicate how much the transmission increases in strength.

Photoluminescence (PL) measurements for this device are shown in Figure 5.2. In panel (a) different PL curves are shown corresponding to different gate voltages from -0.8 V to +0.8 V. In this range of voltages the PL intensity associated with neutral excitons, labelled X^o, decreases rapidly. Normalised PL curves are shown in panel (b). In this panel, the PL curves shown in (a) were normalised from 0 to 1 to observe the shoulder associated with negative trions, labelled X^-. Although the appearance of signals from negative trions observed in transmission and in PL measurements are clearly visible, the oscillator strength of this signal is still too weak to observe any coupling with the light field, therefore the discussion in the following paragraphs focuses only on neutral excitons coupled to cavity photons.

No significant electrical current through the hBN barrier in this range of voltages was observed, which suggests that the free electrons are being accumulated on the WS_2 which then leads to a reduction in the excitation rate of neutral excitons through Coulomb screening [88].

5.3 Tuneable microcavity

A tuneable microcavity was completed by adding a second silver mirror (top mirror) close to the top of the WS_2 transistor, as shown in Figure 5.3(b). Transmission spectra were collected for the microcavity as a function of the thickness of the air gap between the hBN spacer and the top silver mirror in a region

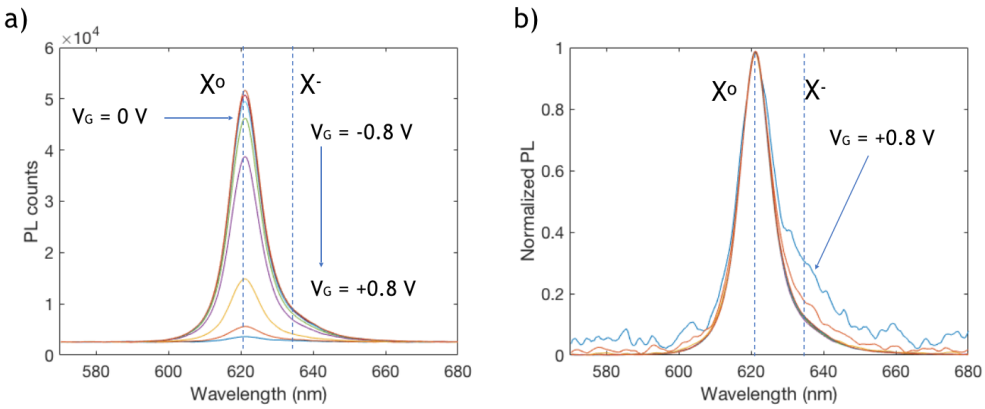

FIGURE 5.2: (a) Photoluminescence (PL) measurements of the device shown in Figure 5.1(b) for different values of the gate voltage. A significant decrease of the PL intensity of neutral excitons (X^0) is observed for positive values of the gate voltage. (b) is the data shown in (a) normalised from 0 to 1. A weak shoulder in the PL curves for the most positive voltages is observed, and is associated with emission from radiative recombination of negative trions (X^-).

where there is no WS_2. To reach this region the bottom mirror was translated perpendicularly to the optical axis. These transmission spectra are then compared to the modelled spectra from which the experimental value for the thickness of the air gap was extracted, as shown in the left panels of Figure 5.3(a). Here the second-, third-, and fourth-order cavity modes can be identified. It is observed the excellent stability of the tuneable system, and excellent quality of the microcavity modes compared to modelling. These measurements were repeated in a region of the microcavity where the 1L-WS_2 was present, keeping the gate voltage fixed at 0 V. These measurements were compared to the model and are shown in the panels on the right side of Figure 5.3(a).

To identify the position of the WS_2 flake with respect to the intensity of the field confinement, a calculation of the electric field in the microcavity structure was performed. These calculations are shown in Figure 5.4. For these calculations the thicknesses of the different materials are: Ag 40 nm, hBN 46 nm, WS_2 0.7 nm, and air gap 787 nm. Figure 5.4 (a) shows the electric field map

as a function of wavelength, where vertical white lines identify material interfaces. The third- and fourth-order cavity modes can be identified, where the third-order mode is split in two suggesting the formation of exciton-polaritons. Figure 5.4 (b) shows the intensity of the confined field (blue line) for a particular wavelength of 622 nm, and the real component of the refractive index of the different materials (red line). In this figure it is observed that the WS_2 flake is placed close to an antinode of the confined field. As mentioned before, the WS_2 can be better positioned in the microcavity by controlling the thickness of the hBN flake. The optimum thickness for the hBN flake is 60 nm. If this thickness is realised, the third-order mode splitting would be ~ 66 nm. So the splitting measured of 60 nm, is approximately 90% of the largest splitting that would be achieved with an optimum hBN thickness.

In Figure 5.3(a), a splitting of the cavity modes is observed at a wavelength of 622 nm, associated with the neutral exciton transition of WS_2. The mode splitting of the three cavity modes observed is greater than that of both the empty cavity mode and the exciton line widths (36 and 35 meV respectively), demonstrating that the system is in the strong coupling regime. The calculated transmittance of a strongly coupled 1L-WS_2-microcavity with an air gap of 787 nm is fit to the experimental values as shown in Figure 5.3(c), where the free parameter was the oscillator strength of WS_2; it was found that the best fit was achieved for an oscillator strength of $f = 2.6$. The air gap thickness of 787 nm reaches the third-order cavity mode. The oscillator strength estimated in these experiments are significantly larger than values reported for WS_2 on SiO_2 or Al_2O_3 substrates[71, 89]. The origin of this discrepancy could be the difference in the dielectric environment provided by the hBN flake in the devices used in this study, and also to the fact that hBN provides an atomically smooth surface (roughness lower than 0.5 nm as measured by atomic force microscopy) which

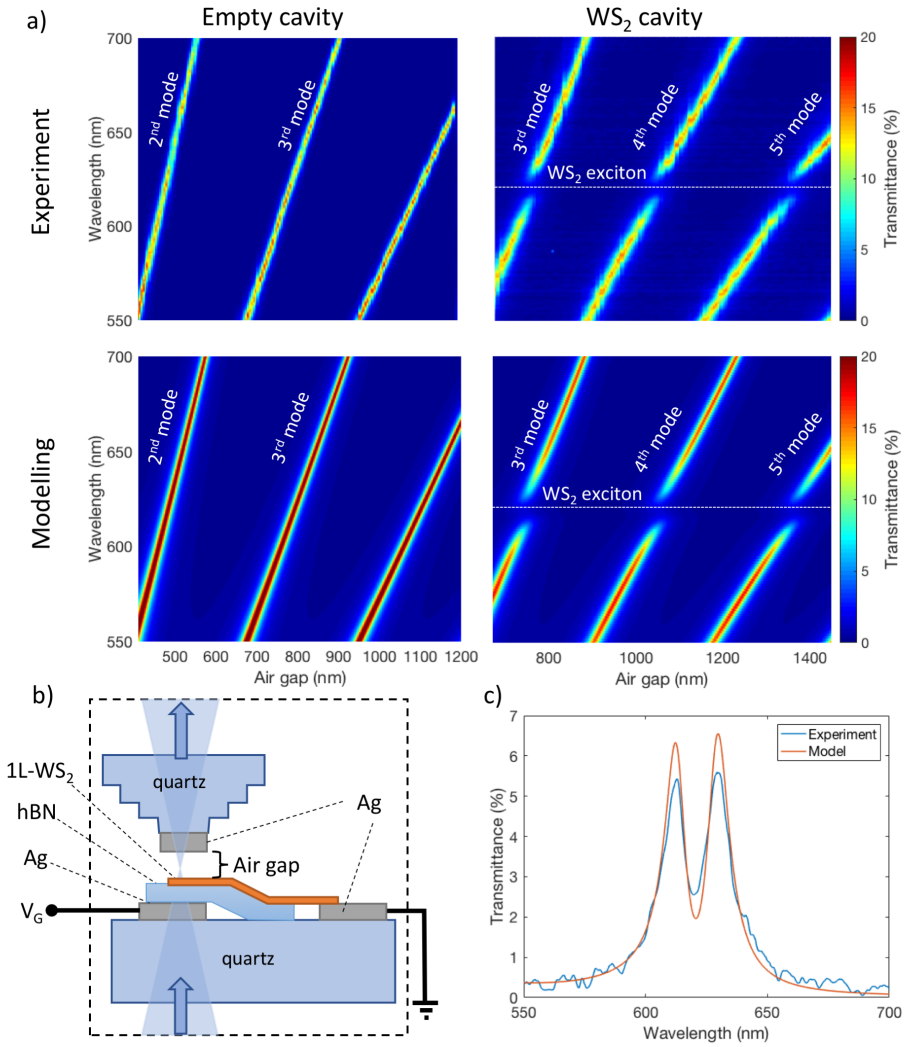

FIGURE 5.3: a) Experimental data and modelling of the empty cavity modes and the WS_2-cavity modes as a function of the air gap between the WS_2 flake and the top silver mirror. b) Schematic of the tuneable microcavity, which consists of the same sample shown in Figure 5.1(b) but with a top mirror added leaving a small gap between the bottom and top mirrors. c) Experimental and calculated transmittance of a strongly coupled WS_2 microcavity. Strong coupling was achieved for a cavity air gap of 787±3 nm, which corresponds to the third-order cavity mode.

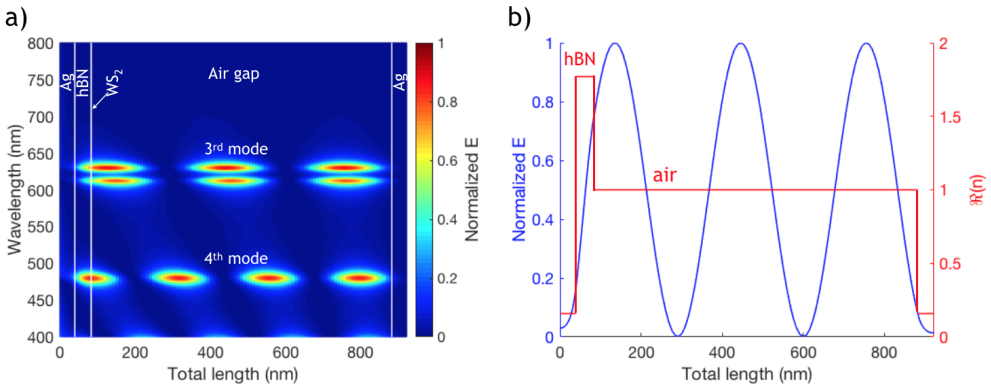

FIGURE 5.4: (a) Calculation of the electric field in the structure shown in Figure 5.3(b). A splitting of the third-order cavity mode is observed. (b) Electric field profiled of the third-order cavity mode (blue line) for a wavelength of 622 nm. The red line is the real component of the refractive index of the different materials in the microcavity structure.

may reduce surface scattering and trapping effects in the WS_2/hBN interface.

The second- and first-order cavity modes were not possible to achieve due to the presence of thick WS_2 flakes nearby the semiconductor monolayer. Those thick flakes are estimated to be hundreds of nanometres thick, so the air gap can not be reduced below 400 nm.

5.4 Electrical control of the light-matter coupling

The evolution of the cavity mode splitting in the strong coupling regime for different gate voltages ranging from -8 V up to +8 V is discussed next. To study the exciton and photon nature of the polariton bands, a two coupled oscillator model analysis of the experimental data was performed, from which the Hopfield coefficients are found as described in Section 4.3. This analysis was focused on the splitting of the third-order cavity mode, for four values of the gate voltage: -8 V, +3V, +5 V, and +6 V. These results are shown in Figure 5.5(a), in which the four values of the gate voltage are indicated.

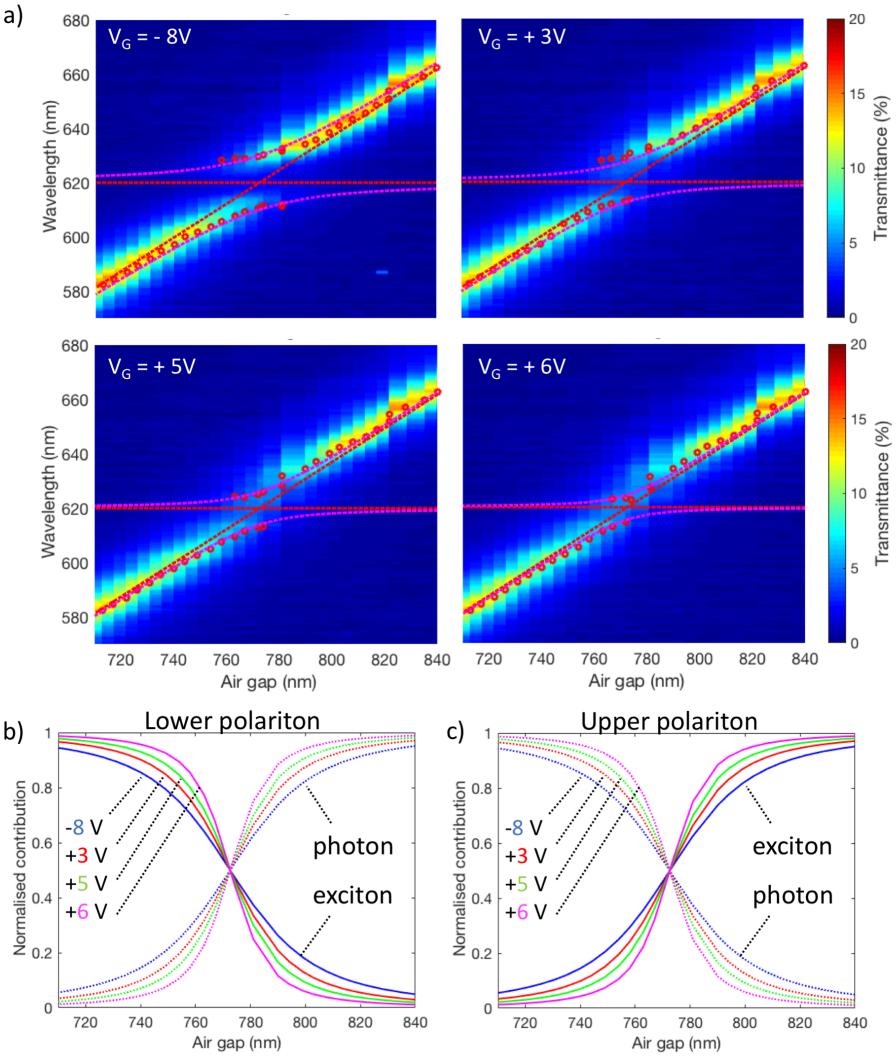

FIGURE 5.5: (a) Analysis of the transmittance spectra of the third-order cavity mode of the WS_2 microcavity for different values of the gate voltage. Dashed oblique lines are the uncoupled cavity modes obtained from modelling an empty microcavity (see Figure 5.3(a)), horizontal dashed lines indicate the neutral exciton transition of WS_2, and curved dashed lines are the lower and upper polariton bands obtained from the coupled oscillator model. Circles are the experimental peak centres of the transmission data. (b) And (c) are the Hopfield coefficients of the lower and upper polariton bands, respectively. The different colours correspond to different values of the gate voltage. Continuous lines correspond to the exciton contribution to the polariton bands. Dashed lines correspond to the cavity photon contribution.

On each plot are shown the position of the neutral exciton transition of WS_2 as a horizontal dashed line, and the third-order cavity mode as an oblique dashed line. The circles are the peak maxima obtained by fitting Pseudo-Voigt functions to the experimental data, for each value of the air gap. The coupled oscillator model is then fit to the positions of the peak maxima. The input parameter in this analysis is the experimental value of the Rabi splitting, which corresponds to the transmission peak splitting at the point where the neutral exciton transition crosses the bare cavity mode. From the coupled oscillator model the Hopfield coefficients were obtained which are shown in Figure 5.5(b) for the lower polariton band, and (c) for the upper polariton band. It is observed in this figure that the lower polariton band becomes more photon-like for the most positive values of the gate voltage, and therefore less exciton-like. The upper polariton band becomes more exciton-like for the most positive values of the gate voltage. The behaviour of both of the polariton bands suggests a decoupling between excitons and cavity photons that occurs when a positive gate voltage is applied. A decoupling between excitons and cavity photons can also be observed as a reduction of the Rabi splitting as a function of the gate voltage, as shown in Figure 5.6.

In Figure 5.6 the transmittance peak splitting is shown for (a) the third, (b) the fourth, and (c) the fifth-order cavity modes as a function of the gate voltage. These modes correspond to fixed air gaps, being 787 $\pm$ 3 nm, 1097 $\pm$ 3 nm, and 1408 $\pm$ 3 nm respectively. For the three modes, a dependence of the Rabi splitting on the gate voltage is observed; the Rabi splitting reaches a saturation value when sufficiently negative voltages are applied to the transistor. In addition, the maximum splitting is lower for higher order cavity modes, as expected due to the weaker fields associated with the higher-order modes. From these measurements the Rabi splitting as a function of the gate voltage is

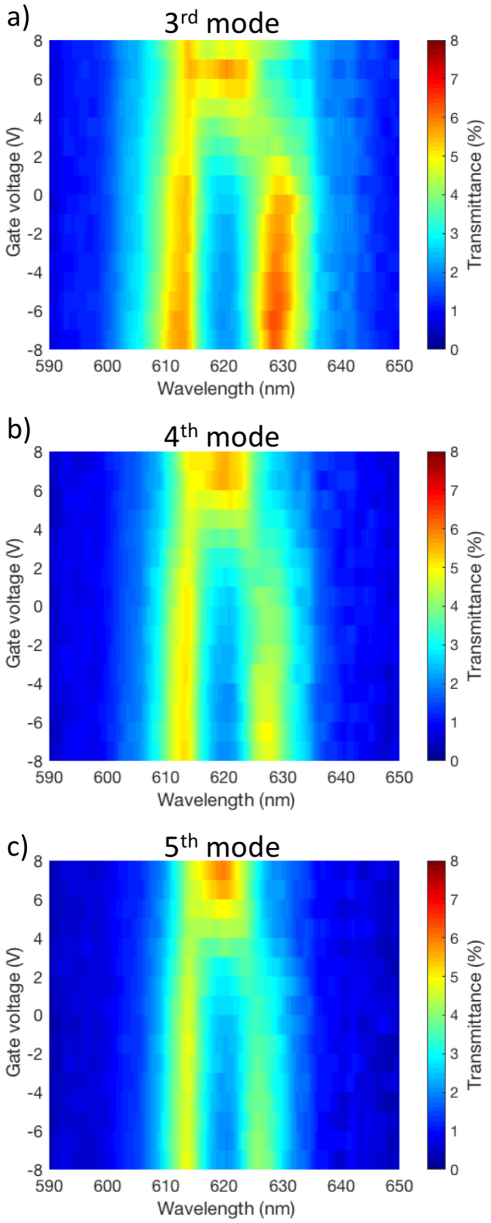

FIGURE 5.6: Transmittance spectra of a WS_2 microcavity for different values of the gate voltage and for a fixed air gap: (a) 787 $\pm$ 3 nm, (b) 1097 $\pm$ 3 nm, and (c) 1408 $\pm$ 3 nm, which correspond to the third-, fourth-, and fifth-order cavity modes, respectively.

obtained for the three cavity modes, as shown in Figure 5.7(a). In this figure the exciton line width is indicated indicated, which is equal to or larger than any of the three cavity mode widths, indicating that the system is in the strong coupling regime when the Rabi splitting is greater than the exciton line width.

5.5 Rabi splitting and density of free electrons

The dependence of the oscillator strength of WS_2 on the gate voltage was obtained; this dependence is related to an increase of the density of free electrons in the WS_2. To do this, the splitting of the third-order cavity mode was analysed. First the transmittance spectrum, shown in Figure 5.3(c) was calculated using an oscillator strength of $f_0 = 2.6$ (see Equations 4.14 and 4.9), which results in a Rabi splitting of 60 meV that corresponds to the splitting of the third-order mode for a gate voltage of 0 V. Before these measurements a sufficiently positive gate voltage was applied to the transistor to remove any excess of free electrons in WS_2, so f_0 is the initial oscillator strength for zero density of free electrons in the TMD. Next, the oscillator strength was varied in the calculations to reproduce the values of the Rabi splitting shown in Figure 5.7(a) for the different values of the gate voltage. The density of free electrons N can be obtained by inserting the obtained values of the oscillator strength, f, into Equation 5.1 [63, 65];

$$f(N) = \frac{f_0}{1 + \frac{N}{N_s}}, \tag{5.1}$$

where the saturation number N_s is defined as the number density of carriers per unit area at which the oscillator strength is reduced to half of the initial value f_0. The value of N_s can be estimated for any 2-dimensional system that allows for the excitation of excitons and free carriers either in the conduction or the valence band. The value N is given in units of πa_{EB}^2. In this analysis,

the saturation number N_S defined as $N_s = 1/8.3\pi a_{EB}^2$ was extracted from [65], where a_{EB} is the effective exciton-Bohr radius of WS_2, which has been taken from reference [90] to have a value of 2 nm corresponding to the X^0 exciton transition.

These results are shown in Figure 5.7(b), where the saturation function as described in Equation 5.1 is also included . The density of free electrons N found in this way agrees well with what is expected in a TMD-based transistor that operates below the level of the Mott transition (a transition from semiconductor to metal due to a high concentration of charge carriers) [86, 91]. This transition has been estimated to occur at a density above $10^{13}\ cm^{-2}$. In the system studied here the saturation density was found to be $9.6 \times 10^{11}\ cm^{-2}$, and in the range of voltages applied, the density of free electrons in the WS_2 ranges from 0 up to $3.2 \times 10^{12}\ cm^{-2}$.

5.6 Summary and conclusions

In summary, continuous control over the light-matter coupling of exciton-polaritons was studied in a WS_2-microcavity at room temperature. This was achieved by controlling the charge carrier density in the semiconductor material. Due to a Coulomb interaction the free carriers screen the oscillator strength of excitons in WS_2. A specially designed WS_2-based field effect transistor was built on one of the mirrors of the microcavity [74], then a second mirror was placed on top of the transistor, leaving an air gap which was controlled with a precision of ± 3 nm in a tuneable system. This tuneability allows for the study of the polariton bands as a function of the thickness of the air gap and allows for access to different cavity modes ranging from the second-order to the fifth-order. For each of the cavity modes, at the resonant condition with WS_2 excitons forming

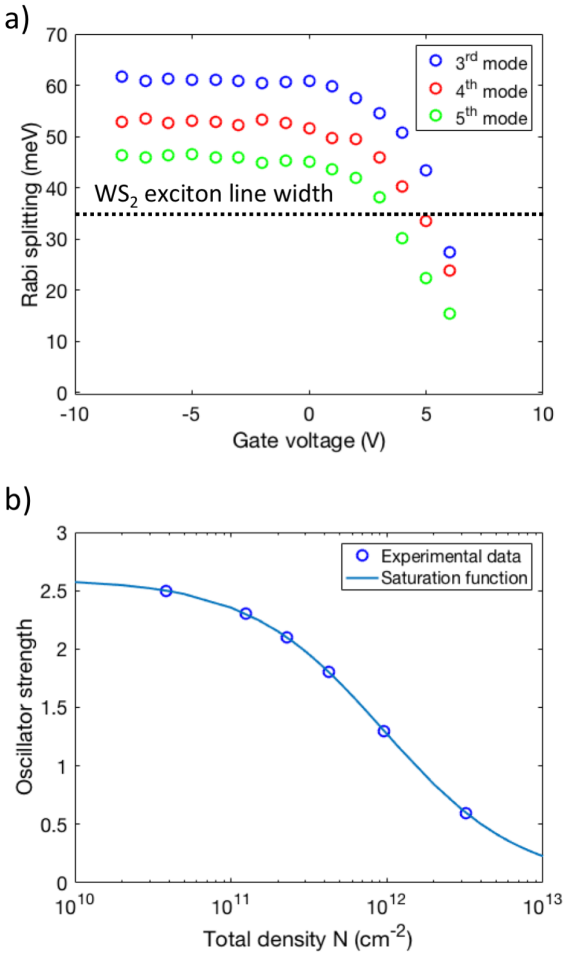

FIGURE 5.7: (a) Rabi splitting as a function of the gate voltage obtained from the data shown in Figure 5.6. The three different cavity modes are shown as different colors: blue for the 3^{rd} mode, red for the 4^{th} mode, and green for the 5^{th} mode. (b) Oscillator strength as a function of the total density of electrons N. The saturation function (Equation 5.1) is also shown.

exciton-polaritons, the transmittance spectra were recorded over a range of gate voltages from -8 V up to +8 V, observing a dependence of the Rabi splitting on the gate voltage. Over this range of voltages the variation of the oscillator strength in the TMD film was calculated by matching the transmittance spectra model to the measured values of the Rabi splitting. The change in the oscillator strength of WS_2 was attributed to the Coulomb screening by the free electrons populating the conduction band of the TMD, and the density of free carriers in the conduction band was extracted, which ranges from 0 cm^{-2}, at a gate voltage of 0 V, up to 3.2 $\times$ 10^{12} cm^{-2}, for a gate voltage of +8 V. Over this range of density of free carriers, the Rabi splitting ranges from a maximum value, which depends on the cavity mode chosen, down to zero, so the system spans the strong to weak coupling regimes. This change in the Rabi splitting could also be extended to p-type semiconductors with a strong excitonic resonance by injecting holes in the valence band of the material.

Chapter 6

Control of polariton-mediated exciton energy exchange

This study demonstrates electrical control over the energy exchange between exciton states mediated by cavity-polaritons at room temperature [92]. A field-effect device, based on a monolayer of WS_2, is built on the bottom metallic mirror of a tuneable Fabry-Pérot microcavity; on the top mirror, a monolayer of MoS_2 is placed leaving a controllable gap of ~ 1 μm between the top and bottom semiconductors. This device is specially designed for the multiple hybridization of microcavity modes with the two exciton species supported by WS_2 and MoS_2, allowing for polariton-mediated exciton energy exchange. It is further shown that the tuning of the free carrier density in the WS_2 film through field-effect gating leads to a strong modulation of the Rabi splitting that modifies the excitonic and photonic nature of exciton-polaritons. Electrical control of polaritonic devices may lead to technological applications using switchable quantum states.

6.1 Introduction

As described in Chapter 2, a confined light field can hybridise with excitons supported by semiconductor materials. Moreover, a confined light field can hybridise multiple times with different exciton species. These multiple hybridisations have been observed in organic materials that are either mixed [93–95] or spatially separated [95–97] in an optical microcavity. This multiple hybridisation allows for an efficient energy exchange between the different exciton states mediated by polaritons, and is effective for a separation between excitons that is larger than the typical length for Förster energy transfer [98, 99]. The Förster energy transfer occurs through dipole-dipole interaction; the strength of this interaction decreases as the distance between the two dipoles increases. The typical distance over which this process is significant is < 10 nm. Polariton-mediated energy transfer has been observed at distances between molecules above 100 nm [95–97]; at such distance the Förster energy transfer is not significant. Polariton-mediated exciton energy exchange has also been observed by combining a 2-dimensional material with organic molecules at room temperature [69], and with semiconductor quantum wells at low temperature [100]. However, control over such polariton mediated exciton energy exchange has not been observed in two spatially-separated atomically-thin excitonic materials at room temperature, which would represent an interesting way to provide remote control over optical and physical properties of materials through the manipulation of light-matter states.

In this study a WS_2-based field-effect device (FED) and a MoS_2 monolayer were combined in a tuneable Fabry-Pérot microcavity. The microcavity is made using 40 nm thick silver mirrors evaporated on quartz glass. A hBN flake is used as a dielectric spacer between the silver film and the TMD. Each TMD/hBN heterostructure is placed on one mirror of the tuneable system, and

the air gap thickness that separates the two excitonic materials is controlled with a precision of 3 nm. In this system, normal-incidence optical transmission measurements were performed as a function of the air gap thickness ranging from 800 to 1100 nm, which allows for the observation of the fourth-order cavity mode. The angular dispersion of the illumination beam in the optical setup is $< \pm 5^o$. The exciton states of both materials hybridise with the confined light field of the microcavity allowing for the formation of exciton-polaritons that combine the properties of the three constituents; the cavity photons, and the two exciton species supported by WS_2 and MoS_2 at wavelengths of 622 and 669 nm respectively. The oscillator strength of one exciton species was then manipulated through field-effect gating [61, 71, 101] and it is shown that this gating alters the nature of the multiple hybridisation of exciton-polariton states.

6.2 Device design

The design of a tuneable microcavity with two spatially-separated monolayer TMDs embedded inside is shown in Figure 6.1(a). On the bottom mirror of the microcavity a FED was built and was based on a monolayer of WS_2. The FED consists of a stack of monolayer WS_2 placed on a hBN flake and this heterostructure is placed onto a silver film that acts as a microcavity mirror as well as a gate electrode. A gate voltage is applied to the silver electrode while the TMD flake is kept grounded. The hBN flake acts as an electric insulator for the FED, and also as a dielectric spacer for the microcavity. According to calculations the optimum position for the WS_2 to interact with the antinode of the confined field in the microcavity requires a thickness of the hBN flake of 60 nm, and for MoS_2 the required thickness is 80 nm. In the sample used in this study the thickness of the hBN flakes were 46 ± 2 nm for the WS_2/hBN heterostructure, and 88 ± 2 nm for the MoS_2/hBN heterostructure, as measured

by atomic force microscopy (AFM). These experimental thicknesses result in an effective Rabi splitting that is at least 90% of the largest Rabi splitting that would be achieved with an optimum hBN thickness.

6.3 Transmission measurements and calculations

The transmittance of the WS_2-based FED for values of the gate voltage between -5 and +5 V was measured first. These results are shown in Figure 6.1(b), where a decrease in strength of the transmittance dip of the A-exciton transition is observed at a wavelength of 622 nm that is significant only for positive values of the gate voltage. No change is observed in the B-exciton transition at a wavelength of 527 nm for the same range of gate voltages. The change in transmittance of the WS_2 monolayer is attributed to an induced Coulomb screening that reduces the oscillator strength of WS_2 excitons due to an increase in the free charge carriers populating the conduction band of the TMD when positive voltages are applied [61, 71]. Additionally, the leakage current through the hBN barrier is negligible, which confirms that the charge carriers are being accumulated in the WS_2 flake.

The transmittance of the microcavity structure was measured as a function of the air gap thickness for different values of the gate voltage applied to the WS_2-based FED. Figure 6.2 shows results of these measurements for two different values of V_G; (a) 0 V, and (b) +5.5 V, as indicated in the figures. It is also observed in this figure that the cavity mode, which varies linearly in spectral position with the air gap, is split at the values of wavelength corresponding to the WS_2 and the MoS_2 exciton transitions. These values of the wavelength are indicated by the horizontal white dashed lines; at 624 nm for the WS_2 exciton transition, and at 669 nm for the MoS_2 exciton transition. The oblique white dashed line

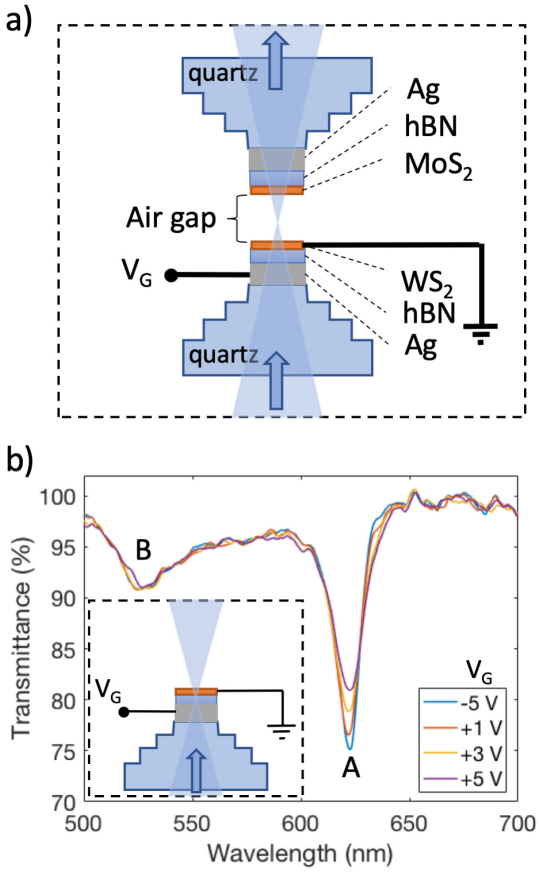

FIGURE 6.1: (a) Schematic of the tuneable microcavity with the two TMD/hBN heterostructures embedded inside. A MoS_2/hBN heterostructure is placed on the top mirror of the microcavity. On the bottom mirror, a field-effect device based on WS_2 is constructed. (b) Transmittance of the WS_2 monolayer for different gate voltages V_G, from -5 to +5 V. The sample for these measurements is shown in the inset of this figure. The transmittance dips at 622 nm and 525 nm are associated with the A and B exciton transitions of WS_2 respectively.

indicates the bare cavity mode, and the black dashed lines are the results of the three coupled oscillator model as shown in Equation 6.1.

$$\mathcal{M} = \begin{pmatrix} \hbar\omega_c - i\hbar\gamma_c/2 & -g & -g' \\ -g & \hbar\omega_{0,1} - i\hbar\gamma_1/2 & 0 \\ -g' & 0 & \hbar\omega'_{0,1} - i\hbar\gamma'_1/2 \end{pmatrix}, \tag{6.1}$$

where in the diagonal terms: ω_c, $\omega_{0,1}$, and $\omega'_{0,1}$ are the frequencies of the fourth-order cavity mode, the WS_2 A-excitons, and the MoS_2 A-excitons respectively. Their respective energy-loss rates are γ_c, γ_1, and γ'_1. The energy-loss rates were obtained experimentally from the full-width-half-maximum (*fwhm*) of the transmission peaks of the bare cavity mode and the exciton transitions [102].

For the cavity mode $\hbar\gamma_c = 36$ meV, and for the exciton transitions these parameters are listed in Chapter 4 in Tables 4.1 and 4.2 with $j = 1$ corresponding to A-excitons. In the non-diagonal terms of Equation 6.1, g is the coupling strength between cavity photons and WS_2 excitons, and g' is the coupling strength between cavity photons and MoS_2 excitons. WS_2 excitons, as well as MoS_2 excitons, hybridise with the confined field in the strong coupling regime according the criteria described by Savona *et al.* [84], since their coupling strengths fulfill the condition $4g > |\gamma_1 - \gamma_c|$ and $4g' > |\gamma'_1 - \gamma_c|$ [84], where $2g = 57.1$ meV and $2g' = 27.3$ meV. In the strong coupling regime, the Rabi splitting Ω can be obtained from the coupling strength and the energy-loss factors at resonant condition between cavity photons and excitons [84, 102, 103]: $\Omega = 2\sqrt{g^2 - (\hbar\gamma/2 - \hbar\gamma_c/2)^2}$. For WS_2 exciton-polaritons the Rabi splitting is $\Omega = 57$ meV, and for MoS_2 exciton-polaritons, $\Omega = 27$ meV.

However, for the criteria described in Chapter 4, section 4.5.3, MoS_2 is weakly coupled to cavity photons. This discrepancy presents an interesting platform for a more in-depth study of exciton-photon coupling at the limit between the

weak and the strong coupling regimes. To continue the study presented in this chapter, I use Savona's criterion for the strong coupling regime.

Additionally, the second and third criteria for the strong coupling regime, described in Chapter 4, can not be applied in this system as the coupling matrix of Equation 6.1 is non-Hermitian and does not conserve $\mathcal{PT}$-symmetry for any value of the energy loss factors.

To calculate the transmittance of the structure shown in Figure 6.1(a) as a function of the air gap thickness the experimental permittivities of the TMDs were determined first. The procedure involved measuring the transmittance of a bare monolayer TMD that was compared with the calculated transmittance. The calculation of the transmittance was produced after fitting the optical parameters for the Lorentz model of the permittivity of the TMDs, as shown in Equation 6.2.

$$\varepsilon_r(\omega) = 1 + \sum_{j=1}^{3} \frac{f_j \omega_{0,j}^2}{\omega_{0,j}^2 - \omega^2 - i\gamma_j \omega}, \tag{6.2}$$

where f_j, $\omega_{0,j}$, and γ_j are the oscillator strength, the resonant frequency, and the energy-loss rate of the j-th electronic transition respectively.

The optical parameters are shown Chapter 4, in Tables 4.1 and 4.2. For each TMD three resonances were fit; $j = 1$ is associated with the A exciton transition, $j = 2$ with the negatively charged trion (A^-), and $j = 3$ with the B exciton transition. The oscillator strength f_j used in Equation 6.2 is a phenomenological quantity that accounts for the strength of the transmittance dip associated with exciton transitions.

Then, the transfer matrix approach was used to calculate the transmittance of the multilayer structure as a function of the air gap thickness. The result of these calculations is shown in Figure 6.2(c). The calculation shown in Figure 6.2(c) agrees very well with measurements for V_G = 0 V. To observe the dependence

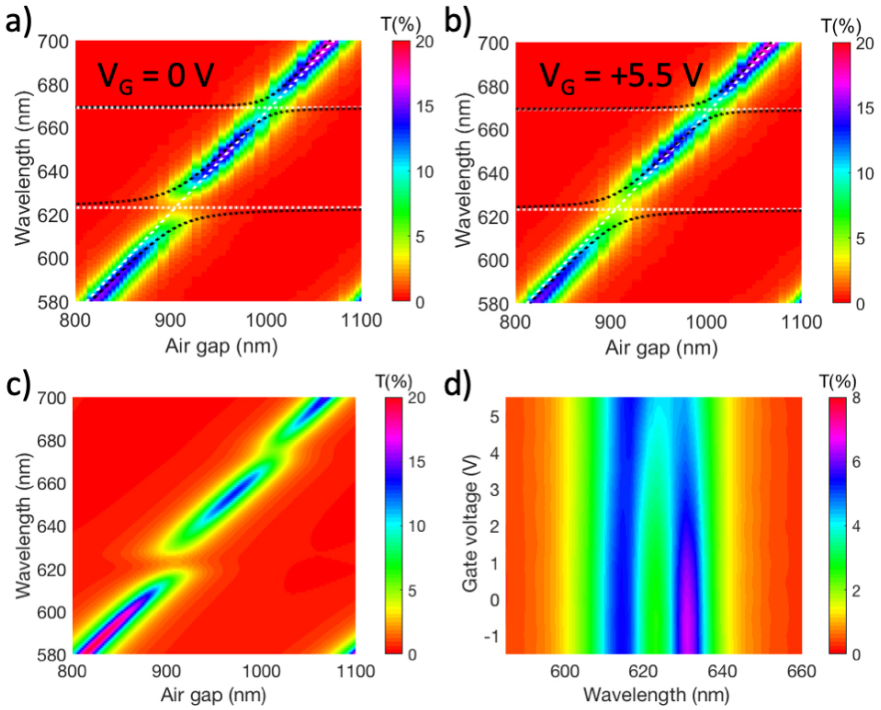

FIGURE 6.2: Measurements and modelling of the tuneable microcavity with the two TMD/hBN heterostructures embedded inside. (a) is the transmittance as a function of the air gap between the two TMDs for a gate voltage of 0 V in the WS_2-based FED. (b) is the same as (a) with a gate voltage of +5.5 V. The white dashed horizontal lines indicate the wavelengths of the A-exciton transitions at 669 nm for MoS_2 and at 622 nm for WS_2. (c) Calculated transmittance as a function of the air gap. (d) Experimental transmittance peak splitting as a function of V_G for a fixed air gap of 905 ± 3 nm, for which the anticrossing between the WS_2 excitons and the cavity mode occurs.

of WS_2 exciton-polaritons on the gate voltage, the cavity length was fixed to 967 ± 3 nm, and the transmittance was measured for different values of V_G, ranging from -1.5 V up to +5.5 V. These results are shown in Figure 6.2(d). The transmittance peak splitting associated with WS_2 exciton-polaritons decreases as positive voltages are applied. This change is a result of the decrease of the oscillator strength of WS_2 excitons due to Coulomb screening as a result of an increase of the free charge carriers populating the conduction band of the TMD [61, 71].

6.4 Electrical control over the multiple hybridisation

To elucidate the photonic and excitonic nature of the hybrid system, the contribution of the cavity photons and the WS_2 and MoS_2 excitons to the middle polariton band of the microcavity structure was studied using the Hopfield coefficients [85]. Figure 6.3 shows the Hopfield coefficients of the middle polariton band of the microcavity structure for different values of V_G as a function of the air gap thickness. In these figures, the blue lines correspond to the WS_2 exciton contribution, the green lines to the MoS_2 exciton contribution, and the red lines to the cavity photon contribution. The vertical dashed line indicates the value of the air gap for which WS_2 and MoS_2 excitons contribute the same amount to the middle polariton band for V_G = -1.5 V. The double lines in Figure 6.3(a) for the three contributions are results of two different values of the Rabi splitting Ω, for gate voltages of the WS_2-based FED of -1.5 V and +5.5 V.

To elucidate this dependence of the Hopfield coefficients on Ω, these measurements were analysed for a range of different values of V_G, from -1.5 V up to +5.5 V in steps of 0.5 V. These results are shown in Figure 6.3(b) for the cavity photon contribution, and in Figure 6.3(c) for the two exciton contributions. In Figure 6.3(b) it is observed that the cavity photon contribution increases as a more positive voltage is applied, while the WS_2 exciton contribution decreases, as shown in Figure 6.3(c). A minimal decrease is also observed in the MoS_2 exciton contribution compared to the change in the WS_2 exciton contribution.

To comprise the observations, Figure 6.4(a) shows the Rabi splitting of WS_2 exciton-polaritons normalised to the maximum Rabi splitting, which is achieved for V_G = -1.5 V. A saturation function (Equation 6.3) was fit to these data, which

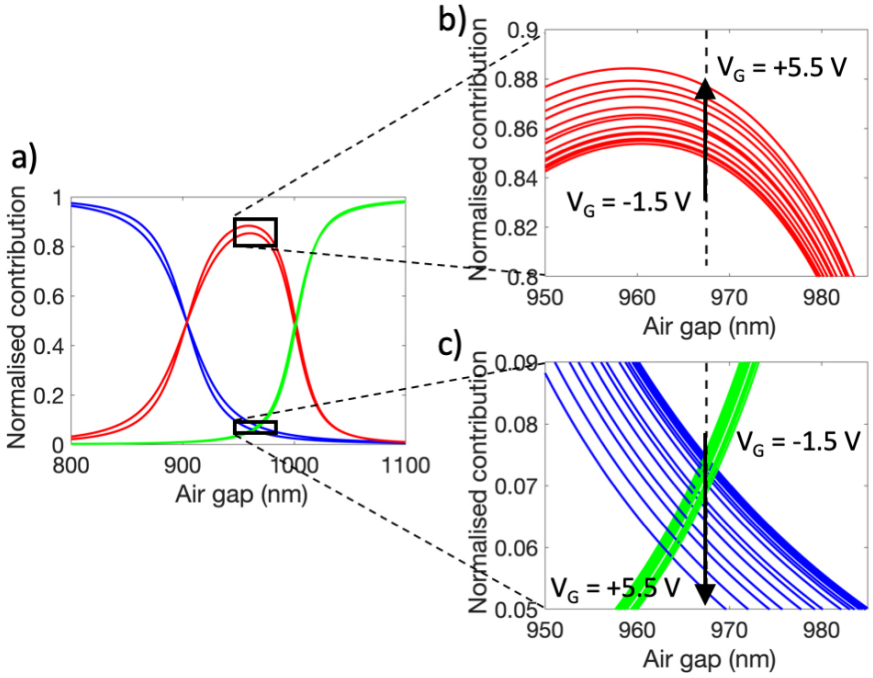

FIGURE 6.3: (a) Hopfield coefficients of the middle polariton band for two values of the Rabi splitting as a result of two values of V_G, which are -1.5 V V and +5.5 V. The blue and green lines indicate the WS_2 and the MoS_2 exciton contribution to the middle polariton band respectively, and the red lines indicate the photon contribution. The vertical dashed line indicates the value of the air gap at which the WS_2 and the MoS_2 excitons have the same contribution to the middle polariton band for V_G = -1.5 V. (b) Zoom-in to the cavity photon contribution to the middle polariton band for a range of V_G between -1.5 V and +5.5 V. (c) Zoom-in to the WS_2 and MoS_2 exciton contributions to the middle polariton band for a range of V_G between -1.5 V and +5.5 V.

is shown as a blue line in Figure 6.4(a);

$$\frac{\Omega(V_G)}{\Omega_0} = \frac{1}{1+\left(\frac{V_G}{V_G^s}\right)^2}, \tag{6.3}$$

where V_G^s is the saturation value of the gate voltage, at which $\Omega = \Omega_0/2$. From the curve-fitting procedure, a saturation voltage of $V_G^s = 11.2$ V was obtained. Equation 6.3 is a phenomenological expression based on the study of the saturation of excitons reported in references [65] and the saturation of exciton-polaritons reported in [63].

Figure 6.4(b) shows the WS_2 and MoS_2 exciton contributions, and the cavity photon contribution to the middle polariton band as a function of the gate voltage applied to the WS_2-based FED. These data are obtained from Figure 6.3(b,c) at a fixed cavity length of 967 ± 3 nm, indicated by the vertical dashed line. A clear dependence on the gate voltage is observed in the WS_2 exciton contribution to the middle polariton band. A clear dependence is also observed in the cavity photon contribution. As the WS_2 exciton contribution decreases, the cavity photon contribution increases. There is also a small change in the MoS_2 exciton contribution to the middle polariton band.

6.5 Summary and conclusions

In summary, an electrical control over the photonic and excitonic composition of the polariton bands in a microcavity system that combines two different excitonic materials was demonstrated. A WS_2-based field-effect device and a MoS_2 monolayer were incorporated in the microcavity, in a way that both excitonic materials hybridise with the confined light field.

The cavity mode was split at wavelengths of 624 and 669 nm, corresponding

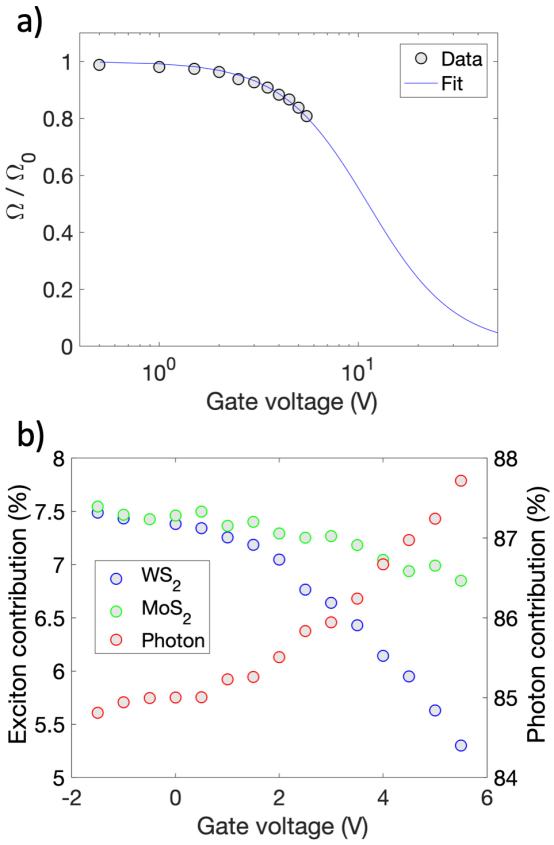

FIGURE 6.4: (a) Normalized Rabi splitting of the WS_2 exciton-polaritons as a function of V_G. Circles are experimental data obtained from Figure 6.2(c). The blue line is a non-linear fit of the saturation function to the experimental data. (b) Exciton and photon contributions to the middle polariton band as a function of V_G. These data are obtained from Figure 6.3 (b) and (c), at a value of the air gap of 967 nm. As the gate voltage increases the WS_2 exciton contribution decreases rapidly and the cavity photon contribution increases in the same way.

to the neutral exciton transitions of WS_2 and MoS_2 respectively, providing evidence for the formation of three polariton states observed as the upper, middle, and lower polariton bands. A splitting of 57 meV was achieved for WS_2 exciton-polaritons, and 27 meV for MoS_2 exciton-polaritons, both formed with the fourth-order cavity mode in the strong coupling regime. Then, the photonic and excitonic composition of the polaritons bands was quantified using a three coupled oscillators model, which allowed for the extraction of the Hopfield coefficients. Through this analysis it was found that, initially, the middle polariton band is composed of cavity photons 85% and 7.5% WS_2 and MoS_2 excitons, for a fixed value of the air gap thickness of 967 ± 3 nm. Then, control of the exciton composition of the polariton bands was demonstrated by altering the coupling strength of WS_2 exciton-polaritons through field effect gating. By applying a positive gate voltage the free charge carrier density in the WS_2 monolayer was increased, which led to a decrease of the exciton oscillator strength. This allowed for the control over the WS_2 exciton composition of the polaritons bands. By increasing the gate voltage, the WS_2 exciton composition decreased while the cavity photon composition increased.

The results presented here are evidence of control over the multiple hybridisation of the confined field in a microcavity with different spatially-separated 2-dimensional semiconductors at room temperature, and may lead to technological applications through switchable quantum states in optoelectronic devices.

Chapter 7

Future work

7.1 Electrical transport in the strong coupling regime

It has been recently reported that the electrical conductivity of an organic semiconductor material can be enhanced up to ten times when strongly coupled to plasmonic modes [47]. The results presented in this report are, to some extent, remarkable for finding new physics, especially for the manipulation of physical properties of materials through strong coupling with a confined light field. The results reported by Orgiu *et al.* have been supported by theoretical modelling using different approaches [48, 104]. However, the tuning of the density of excitons in a semiconductor material through a gate-field is not considered in these reports.

For future work I propose a study of the conductivity of a 2-dimensional semiconductor-based field-effect transistor (FET) strongly coupled to a microcavity. A device for this study has been previously reported in a conference paper [74]. This device consists of a WS_2- (or Rubrene-) based FET embedded in a tuneable microcavity as shown in Figure 7.1. In this device the bottom mirror of the microcavity acts as a gate electrode, which tunes the free charge density in the semiconductor material, in the same way as in the device shown

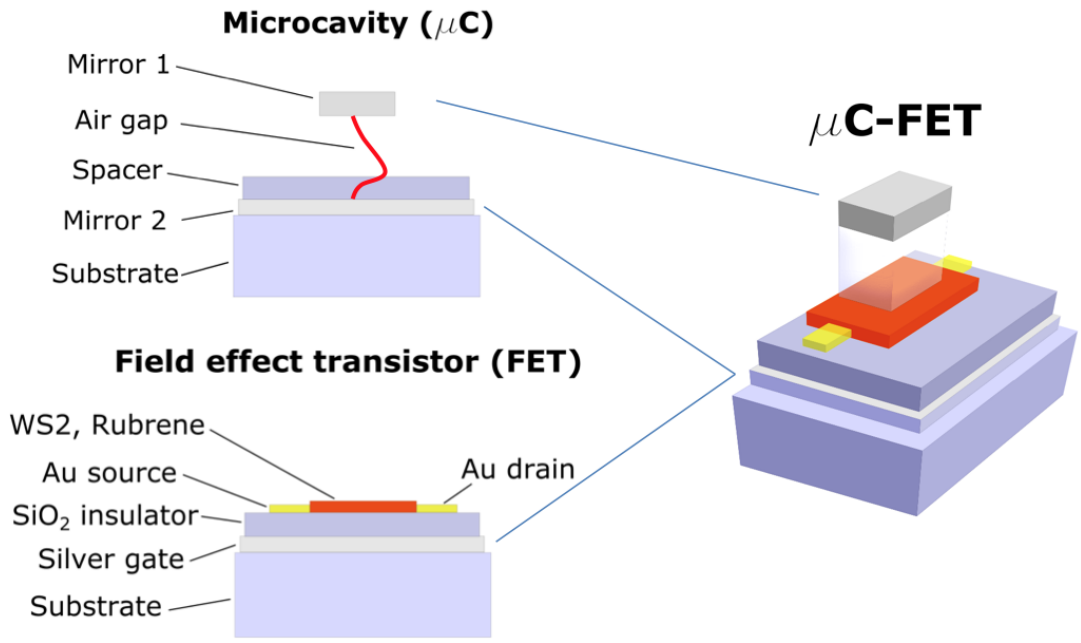

FIGURE 7.1: Semiconductor field effect transistor embedded in a tuneable microcavity.

in Chapter 6. Source and drain electrodes are added to test the charge mobility for the different charge densities, from which the conductivity can be extracted. It would be interesting to measure the conductivity σ of this device when excitons in the semiconductor material are strongly coupled to cavity photons. In a tuneable cavity it is possible to switch the resonance on and off, while conductivity measurements are performed, so a relation between the Rabi splitting Ω and σ can be found.

7.2 Polariton mediated transfer of valley properties

As mentioned in Chapter 2, 2-dimensional semiconductor materials form the family of transition metal dichalcogenides (TMDs) have rich valley properties that can be probed with circularly polarised light at room temperature [105]. It has also been reported that exciton-polaritons formed with these materials at the monolayer limit retain the valley properties when one valley-exciton is

excited using circularly polarised light [106]. It should be possible, in principle, to use the device shown in Figure 6.1 in Chapter 6 to excite one type of valley excitons (for example K-valley excitons) using circularly polarised light on resonance with A-excitons in WS_2, and to measure white light absorption from MoS_2 and its polarisation. As shown in Chapter 6, WS_2 excitons and MoS_2 excitons exchange energy due to strong coupling with a microcavity mode. The open question for this research is: are the WS_2 valley properties transferred to MoS_2 through the formation of exciton-polaritons when combining the two semiconductors in a microcavity? Moreover, it would be interesting to observe valley-polarisation of the MoS_2 excitons mediated by polaritons when the two excitonic materials are spatially separated, as described in Chapter 6. If there is any polarisation information transferred from WS_2 to MoS_2 through polaritons (and none in absence of polaritons), this would be a remote transfer of valley properties, or in some way, a remote manipulation of valley properties using confined light fields, which has not yet been observed to date.

Chapter 8

Summary

In this research thesis I described an original study on control over exciton-polaritons in optoelectronic devices operating at room temperature. These devices consist of a tuneable optical microcavity in which a monolayer WS_2-based field effect device and a monolayer of MoS_2 were embedded to study, first, the electrical control of exciton-polaritons, and second, the electrical control of polariton-mediated exciton energy exchange between the two semiconductor materials. These results provide an important precedent for future investigations on control of exciton-polaritons using 2-dimensional semiconductor materials.

I initially introduced the main concepts involved in this research for understanding a light field confinement device, and how these devices can be designed, controlling important parameters such as mode volume, quality factor, energy-loss factor, and number of resonators. Controlling these parameters allows for designs that can enhance the confinement of a light field, which is crucial for an efficient light-matter interaction. Designing devices for light confinement can be supported by theoretical calculations which I also described in this thesis. I focused this description on a multilayer structure consisting of flat silver mirrors separated by a dielectric slab; the light field can be confined

in between the silver mirrors. I included a comparison between calculations and measurements, showing an excellent agreement between them. These calculations can also be extended to include excitonic materials in the multilayer structure, and the energy dispersion diagram of the device can be calculated and compared with experiments to determine whether exciton-polaritons can be formed in the structured device. From these calculations one can determine precisely the thicknesses of the different layers in the structure to have a strong coupling between excitons in semiconductor materials and photons that form the confined light field. However the strength of the coupling has to be carefully analysed. A two coupled oscillator model can be used to determine the coupling strength between excitons and photons, and to determine if the system is in the weak coupling regime, i.e. no exciton-polaritons are formed, or in the strong coupling regime, i.e. there are indeed exciton-polaritons in the device. Different approximations can be made to the coupled oscillator model which lead to different criteria for determining the limit between the weak and the strong coupling regimes; three different criteria often found in literature are described and compared with each other in Chapter four.

I also described original experimental research on controlling the coupling strength between excitons in 2-dimensional semiconductors and microcavity photons. For this research I implemented a tuneable optical microcavity that allows for tuning and sweeping the cavity length, which determines the resonant frequency of the confined light field, and which can be tuned to the resonant frequency of excitons in a 2-dimensional semiconductor embedded inside to allow for exciton-photon coupling. Once exciton-polaritons were formed, the coupling strength was controlled by doping the semiconductor material with charge carriers. This was achieved by applying a gate voltage to the semiconductor material.

A second research project was described, and it consisted of the electrical control over the exciton energy exchange between two different 2-dimensional semiconductor materials. First, the exciton energy exchange was allowed by coupling the two different exciton species to one microcavity mode. This was done by inserting the two materials in the microcavity structure. Then, by doping one semiconductor with charge carriers, its coupling strength was modified. Therefore the exciton energy exchange with the second semiconductor was also modified.

Finally, I proposed two ideas for future research; the first one is a study of the dependence of the electrical conductivity of a semiconductor material on the coupling strength between excitons supported by the semiconductor and cavity photons. Previous reports have shown that an enhancement of the conductivity can be achieved by strong coupling between excitons and photons, and these observations have been supported by theoretical formulations. However the previous experimental results have not proven to be reproducible. A second idea for future research is the remote control of valley properties of a 2-dimensional semiconductor material. It has been demonstrated that exciton-polaritons retain polarisation properties of excitons, for example K-valley excitons recombine and radiate with one circular polarisation, and K'-valley excitons radiate with the opposite circular polarisation. Now, if two different excitonic materials are coupled to a microcavity mode, such that exciton energy exchange is allowed, the open question is how is the polarisation of exciton-polaritons of the second semiconductor material if one circular polarisation is selected for exciton-polaritons in the first semiconductor material. It would be interesting to see if exciton valley properties are transferred from one material to another through exciton energy exchange mediated by a confined light field.

List of publications

Journal articles

- **Henry A. Fernandez**, Freddie Withers, Saverio Russo, and William L. Barnes, *Electrically tuneable exciton energy exchange between spatially separated 2-dimensional semiconductors in a microcavity*, Applied Physics Letters 115, 071103 (2019).
- **Henry A. Fernandez**, Freddie Withers, Saverio Russo, and William L. Barnes, *Electrically tuneable exciton-polaritons through free electron doping in monolayer WS_2 microcavities*, Advanced Optical Materials 1900484 (2019).
- Kishan S. Menghrajani, **Henry A. Fernandez**, Geoffrey R. Nash, and William L. Barnes, *Hybridization of multiple vibrational modes via strong coupling using confined light fields*, Advanced Optical Materials 1900403 (2019).
- Janire Escolar, Namphung Peimyoo, **Henry A. Fernandez**, and Freddie Withers, *Anisotropic magnetoresistance and Coulomb blockade in defect engineered $Cr_2Ge_2Te_6$ van der Waals heterostructures*, Physical Review B 100, 054420 (2019).

Conference proceedings

- **Henry A. Fernandez**, Saverio Russo, and William L. Barnes, *Modification of Charge Carrier Mobility by Strong Light-Matter Coupling in Organic and Inorganic Semiconductors*, Laser Science, JW3A. 59 (2017).
- **Henry A. Fernandez**, Saverio Russo, and William L. Barnes, *Design of strong-coupling microcavities for optoelectronic applications*, Conference on Lasers and Electro-Optics Europe & European Quantum Electronics Conference (CLEO/Europe-EQEC 2017).

Conference participation

- Invited talk titled “Electrical control of exciton energy exchange between two monolayer semiconductors in an optical microcavity" at The Rank Prize Funds symposium on 2-dimensional Semiconductors for Optoelectronics. Lake District, England. April, 2019.
- Talk titled “Electrical control of the Rabi splitting in a strongly coupled semiconductor microcavity" at Nanometa. Seefeld, Austria. January, 2019.
- Poster titled “Strong-Coupling in a Fabry-Perot Microcavity" at Recent Appointees in Materials Science. Exeter, UK. September, 2017.
- Poster titled “Modification of charge mobility by strong coupling in organic and inorganic semiconductor microcavities" at Frontiers in Optics. Washington DC, USA. September, 2017.
- Talk titled “Incorporating a field effect transistor based on 2D materials inside an optical microcavity" at Nanophotonics in 2D materials. San Sebastian, Spain. July, 2017.
- Talk titled “Design of strong coupling microcavities for optoelectronic applications" at CLEO Europe. Munich, Germany. June, 2017.
- Poster titled “Structured Organic Layers and Strong-Coupling in a Fabry-Perot Microcavity" at Strong Coupling in Organic Semiconductors. San Sebastian, Spain. October, 2016.

Appendix A

Matlab codes

A.1 Transmittance and reflectance of multilayer structures

```
%% Constants
clearvars
clc
hbar = 6.582*10^-16; % Planck constant, eV*s
ehbar = 1.51926751447914e+015; % e/hbar where hbar=h/(2*pi) ...
    and e=1.6e-19
eps0 = 1; % vacuum
mu0 = 1; % magnetic permeability nonmagnetic materials
eps_b_surrounding = 1;
c_speed = 3*10^17; % speed of light nm/s

%% Optical constants silver from Rakic et al.,
% Plasma frequency silver
omegap_Ag = 9.01*ehbar;%9.01*ehbar;
% Oscillators' strenght
f_Ag =     [0.845 0.065 0.124 0.011 0.840 5.646];
```

```
16 % Damping frequency of each oscillator
17 Gamma_Ag = [0.048 3.886 0.452 0.065 0.916 2.419]*ehbar;
18 % Resonant frequency of each oscillator
19 omega_Ag = [0.000 0.816 4.481 8.185 9.083 20.29]*ehbar;
20 % Number of resonances
21 order_Ag = length(omega_Ag);
22
23 n0 = 1; % surrounding medium
24 n1 = 1; % surrounding medium
25 n2 = 1; % substrate
26 n3 = 1; % substrate
27 n4 = 1; % substrate
28 n5c = 1; % air gap
29 n5d = 1; % substrate
30 n6 = 1; % surrounding medium
31
32 eps1 = n1^2; %
33 eps2 = n2^2; %
34 eps3 = n3^2; %
35 eps4 = n4^2; %
36 eps5c = n5c^2; %
37 eps5d = n5d^2; %
38 eps6 = n6^2; %
39
40 d3 = 0; % substrate thickness, nm
41 d4 = 0; % substrate thickness, nm
42 dAg_l = 40; % left silver thickness, nm
43 dAg_r = 40; % right silver thickness, nm
44 d5c = 0; % air gap thickness, nm
45 d5d = 0; % substrate thickness, nm
46 d5h = 0.7; % WS2 thickness, nm (monolayer d5h = 0.7 nm)
47
48 %% Variable
```

```
col = 1:801;
row = 1:201;
Emin = 1.64; % minimum energy, eV
Emax = 2.5; % maximum energy, eV
lambda = linspace(2*pi*c_speed*hbar/Emax,2*pi*c_speed ...
*hbar/Emin,length(row)); % wavelength, nm
w = 2*pi*c_speed./lambda; % frequency
ko = 2*pi./lambda; % incident wave-vector
E = hbar*w; % Energy from frequency

%% Permittivity
%Silver
epsilon_D_Ag = ones(size(lambda)) - ((f_Ag(1)*omegap_Ag^2) * ...
(w.^2 + 1i*Gamma_Ag(1)*w).^(-1)); % Drude model
epsilon_L_Ag = zeros(size(lambda));
for k = 2:order_Ag
    epsilon_L_Ag = epsilon_L_Ag + ...
        (f_Ag(k)*omegap_Ag^2)*(((omega_Ag(k)^2) ...
    *ones(size(lambda)) - w.^2) - 1i*Gamma_Ag(k)*w).^(-1); % ...
        Lorentz model
end
epsAg = epsilon_D_Ag + epsilon_L_Ag;
epsAg_R = real(epsAg);
epsAg_I = imag(epsAg);

% WS2

epsWS2 = 1 + 2.6./(2.008^2-E.^2-1i*0.035.*E) + ...
    0.1./(1.962^2-E.^2-1i*0.040.*E) + ...
    4.5./(2.38^2-E.^2-1i*0.200.*E); % WS2
epsWS2_R = real(epsWS2);
epsWS2_I = imag(epsWS2);
n_WS2 = epsWS2.^0.5;
```

```
78 nWS2_R = real(n_WS2);
79 nWS2_I = imag(n_WS2);
80
81 %% Refractive index
82 nAg = epsAg.^0.5;
83 nAg_R = real(nAg);
84 nAg_I = imag(nAg);
85 n5h = epsWS2.^0.5;
86 n5h_R = real(n5h);
87 n5h_I = imag(n5h);
88
89 %% Cavity length variable
90 d5c = linspace(0,2000,length(col)); % nm
91
92 %% beta factor
93 for o = 1:length(row)
94     for p = 1:length(col)
95         beta3{o,p} = ko(o).*n3*d3;
96         beta4{o,p} = ko(o).*n4*d4;
97         betaAg_l{o,p} = ko(o).*nAg(o).*dAg_l;
98         betaAg_r{o,p} = ko(o).*nAg(o).*dAg_r;
99         beta5c{o,p} = ko(o).*n5c.*d5c(p);
100        beta5d{o,p} = ko(o).*n5d.*d5d;
101        beta5h{o,p} = ko(o).*n5h(o).*d5h;
102    end
103 end
104
105 %% Z factor
106 Z1p = 1./n1;
107 Z2p = 1./n2;
108 Z3p = 1./n3;
109 Z4p = 1./n4;
110 Z5cp = 1./n5c;
```

```
111 Z5dp = 1./n5d;
112 for s = 1:length(row)
113     for t = 1:length(col)
114         ZAg_l_p_cell{s,t} = 1./nAg(s);
115         ZAg_r_p_cell{s,t} = 1./nAg(s);
116         Z5hp_cell{s,t} = 1./n5h(s);
117     end
118 end
119 Z6p = 1./n6;
120
121 %% Generating layer matrices
122 for q = 1:length(row)
123     for r = 1:length(col)
124        M3{q,r} = [cos(beta3{q,r}),-1i*sin(beta3{q,r})./ ...
125        Z3p;-1i*Z3p.*sin(beta3{q,r}),cos(beta3{q,r})];
126        M4{q,r} = [cos(beta4{q,r}),-1i*sin(beta4{q,r})./ ...
127        Z4p;-1i*Z4p.*sin(beta4{q,r}),cos(beta4{q,r})];
128        MAg_l{q,r} = ...
               [cos(betaAg_l{q,r}),-1i*sin(betaAg_l{q,r})./ ...
129        ZAg_l_p_cell{q,r};-1i*ZAg_l_p_cell{q,r} ...
130        .*sin(betaAg_l{q,r}),cos(betaAg_l{q,r})];
131        MAg_r{q,r} = [cos(betaAg_r{q,r}),-1i ...
132        *sin(betaAg_r{q,r})./ ...
133        ZAg_r_p_cell{q,r};-1i*ZAg_r_p_cell{q,r} ...
134        .*sin(betaAg_r{q,r}),cos(betaAg_r{q,r})];
135        M5c{q,r} = [cos(beta5c{q,r}),-1i*sin(beta5c{q,r})./ ...
136        Z5cp;-1i*Z5cp.*sin(beta5c{q,r}),cos(beta5c{q,r})];
137        M5d{q,r} = [cos(beta5d{q,r}),-1i*sin(beta5d{q,r})./ ...
138        Z5dp;-1i*Z5dp.*sin(beta5d{q,r}),cos(beta5d{q,r})];
139        M5h{q,r} = [cos(beta5h{q,r}),-1i*sin(beta5h{q,r})./ ...
140        Z5hp_cell{q,r};-1i*Z5hp_cell{q,r}.*sin(beta5h{q,r}) ...
141        ,cos(beta5h{q,r})];
142     end
```

```
143 end
144
145 %% Transfer matrix
146 for u = 1:length(row)
147     for v = 1:length(col)
148         M{u,v} = ...
                MAg_l{u,v}*M5d{u,v}*M5h{u,v}*M5c{u,v}*MAg_r{u,v};
149     end
150 end
151
152 for a = 1:length(row)
153     for b = 1:length(col)
154         M11cell{a,b} = M{a,b}(1,1);
155         M12cell{a,b} = M{a,b}(1,2);
156         M21cell{a,b} = M{a,b}(2,1);
157         M22cell{a,b} = M{a,b}(2,2);
158     end
159 end
160
161 %% Reflection, transmission coefficients
162 for g = 1:length(row)
163     for h = 1:length(col)
164        rr{g,h} = Z1p.*M11cell{g,h}+Z1p.*Z6p.*M12cell{g,h}- ...
165        M21cell{g,h}-Z6p.*M22cell{g,h};
166        rt{g,h} = Z1p.*M11cell{g,h}+Z1p.*Z6p.*M12cell{g,h}+ ...
167        M21cell{g,h}+Z6p.*M22cell{g,h};
168        tr{g,h} = 2*Z1p;
169        tt{g,h} = Z1p.*M11cell{g,h}+Z1p.*Z6p.*M12cell{g,h}+ ...
170        M21cell{g,h}+Z6p.*M22cell{g,h};
171        R{g,h} = abs(rr{g,h}./rt{g,h}).^2; % Reflection TM ...
              polarization
172        T{g,h} = (real(Z6p)./real(Z1p)).*abs(tr{g,h}./ ...
173        tt{g,h}).^2; % Transmission TM polarization
```

```
174     end
175 end
176 
177 R_ = cell2mat(R);
178 T_ = cell2mat(T);
179 A_ = 1-R_-T_;
180 %kx_ = cell2mat(kx);
181 
182 R_vec = R_(:);
183 T_vec = T_(:);
184 
185 %kx_vec = kx_(:);
186 w_vec = repmat(hbar*w,1,length(col))';
187 
188 %% 2D plot for a fixed cavity length
189 % d5c(102) = 252.5 nm
190 figure
191 plot(lambda,100*T_(:,102),lambda,100*R_(:,102))
192 legend('\fontsize{20}Transmittance','\fontsize{20}Reflectance')
193 set(gca,'fontsize',20)
194 xlabel('\fontsize{22}Wavelength (nm)')
195 ylabel('\fontsize{22}Intensity (%)')
196 ylim([0 100])
197 xlim([550 700])
198 
199 %% Colour plots
200 
201 size = 1;
202 figure('Position', [10 10 size*500 size*375])
203 surf(d5c,lambda,100*T_,'LineStyle','none')
204 set(gca,'fontsize',20)
205 h = colorbar;
206 set(get(h,'title'),'string','\fontsize{20}T(%)','Rotation',0.0);
```

```
207 colormap hsv
208 axis tight
209 view(0,90)
210 ylim([550 700])
211 xlim([0 1000])
212 caxis([0 30])
213 xlabel('\fontsize{22}Air gap (nm)')
214 ylabel('\fontsize{22}Wavelength (nm)')
215
216 size = 1;
217 figure('Position', [10 10 size*500 size*375])
218 surf(d5c,lambda,100*R_,'LineStyle','none')
219 set(gca,'fontsize',20)
220 h = colorbar;
221 set(get(h,'title'),'string','\fontsize{20}T(%)','Rotation',0.0);
222 colormap hsv
223 axis tight
224 view(0,90)
225 ylim([550 700])
226 xlim([0 1000])
227 caxis([30 100])
228 xlabel('\fontsize{22}Air gap (nm)')
229 ylabel('\fontsize{22}Wavelength (nm)')
```

A.2 Electric field profile of multilayer structures

```
1 %% constants
2 clearvars
3 clc;
4 hbar        =   6.582e-16; % Planck constant, eV*s
```

```
h_planck    =   4.135667516e-15; % eV*s
ehbar = 1.51926751447914e15; % e/hbar where hbar=h/(2*pi) and ...
    e=1.6e-19
c_speed = 3*10^17; % speed of light nm/s

lambda = linspace(500,750,601);

n = [1,1,1,1,1,1,1,1,1,1,1,1,1,1,1,1,1,1,1,1,1];
n_air = 1*ones(1,length(lambda));
n_hBN = 1.77*ones(1,length(lambda));
w = 2*pi*c_speed./lambda;

%% permittivities
% Plasma frequency of Silver
omegap_Ag = 9.01*ehbar;
% Oscillators' strenght
f_Ag =     [0.845 0.065 0.124 0.011 0.840 5.646];
% Damping frequency of each oscillator
Gamma_Ag = [0.048 3.886 0.452 0.065 0.916 2.419]*ehbar;
% Resonant frequency of each oscillator
omega_Ag = [0.000 0.816 4.481 8.185 9.083 20.29]*ehbar;
% Number of resonances
order_Ag = length(omega_Ag);

epsilon_D_Ag = 1*ones(size(lambda)) - ((f_Ag(1)*omegap_Ag^2)...
    * (w.^2 + 1i*Gamma_Ag(1)*w).^(-1)); % Drude model
epsilon_L_Ag = zeros(size(lambda));
for k = 2:order_Ag
    epsilon_L_Ag = epsilon_L_Ag + (f_Ag(k)*omegap_Ag^2)...
        *(((omega_Ag(k)^2)*ones(size(lambda)) - w.^2)...
        - 1i*Gamma_Ag(k)*w).^(-1); % Lorentz model
end

```

```
37 epsAg = epsilon_D_Ag + epsilon_L_Ag; % silver
38
39 epsAg_R = real(epsAg);
40 epsAg_I = imag(epsAg);
41 n_Ag = epsAg.^0.5;
42 nAg_R = real(n_Ag);
43 nAg_I = imag(n_Ag);
44
45 % WS2
46 En = hbar*w;
47 epsWS2 = 1 + 2.7./(1.995^2-En.^2-1i*0.035.*En)...
48     + 0.04./(1.96^2-En.^2-1i*0.04.*En) + ...
          5./(2.38^2-En.^2-1i*0.2.*En);
49 eps_WS2_G = 31*exp(-((En-2.4).^2)./(2*0.3^2));
50 epsWS2_R = real(epsWS2);
51 epsWS2_I = imag(epsWS2);
52 n_WS2 = (epsWS2_R + 1i*epsWS2_I).^0.5;
53 nWS2_R = real(n_WS2);
54 nWS2_I = imag(n_WS2);
55
56 n_c = cell(length(n),1);
57
58 n_c{1,1} = n_air;
59 n_c{2,1} = n_Ag;
60 n_c{3,1} = n_hBN;
61 n_c{4,1} = n_WS2;
62 n_c{5,1} = n_air;
63 n_c{6,1} = n_air;
64 n_c{7,1} = n_air;
65 n_c{8,1} = n_air;
66 n_c{9,1} = n_air;
67 n_c{10,1} = n_air;
68 n_c{11,1} = n_air;
```

```
n_c{12,1} = n_air;
n_c{13,1} = n_air;
n_c{14,1} = n_air;
n_c{15,1} = n_air;
n_c{16,1} = n_air;
n_c{17,1} = n_air;
n_c{18,1} = n_air;
n_c{19,1} = n_Ag;
n_c{20,1} = n_air;

l = 1;
d5cl = 442;
d5c = linspace(d5cl,d5cl,l);
d = [40 60 0.7 0 0 0 0 0 0 0 d5c 0 0 0 0 0 0 40];
dx = cumsum(d);

% permittivity
eps_c = cell(length(n),1);
for i = 2:length(n)-1
    for j = 1:length(lambda)
        eps_c{i,j} = (2*pi./lambda(j)).*n_c{i,1}(j);
    end
end
eps_c = cell2mat(eps_c);
xpos = cell(length(d),1);
for i = 1:length(d)
    for j = 1:length(lambda)
        L{i,j} = [exp(-1i*eps_c(i,j)*d(i)) 0; 0 ...
            exp(1i*eps_c(i,j)*d(i))];
        xpos{i,1} = linspace(0,d(i),100);
    end
end
for i = 1:length(d)+1
```

```
101     for j = 1:length(lambda)
102         r_rl(i,j) = (n_c{i}(:,j)-n_c{i+1}(:,j))./(n_c{i}(:,j) ...
103             +n_c{i+1}(:,j));
104         t_rl(i,j) = 2*n_c{i}(:,j)./(n_c{i}(:,j)+n_c{i+1}(:,j));
105         I_rl{i,j} = [1, r_rl(i,j);r_rl(i,j), 1]./t_rl(i,j);
106     end
107 end
108 M = cell(length(d),length(lambda));
109 for j = 1:length(lambda)
110 M{1,j} = I_rl{1,j}*L{1,j};
111 end
112 for i = 2:length(d)
113     for j = 1:length(lambda)
114     M{i,j} = M{i-1,j}*I_rl{i,j}*L{i,j};
115     end
116 end
117     for j = 1:length(lambda)
118     M{length(d),j} = M{length(d),j}*I_rl{length(d)+1,j};
119     end
120 M_minus = cell(length(d),length(lambda));
121 M_plus = cell(length(d),length(lambda));
122 for j = 1:length(lambda)
123 M_minus{1,j} = I_rl{1,j};
124 M_plus{length(d),j} = I_rl{length(d)+1,j};
125 end
126 for i = 2:length(d)
127     for j = 1:length(lambda)
128         M_minus{i,j}= M_minus{i-1,j}*L{i-1,j}*I_rl{i,j};%
129         M_plus{length(d)+1-i,j} = ...
                I_rl{length(d)+2-i,j}*L{length(d)...
130              +2-i,j}*M_plus{length(d)+2-i,j};
131     end
132 end
```

```
133 E = cell(length(d),length(lambda),length(d5c));
134 for i = 1:length(d)
135     for j = 1:length(lambda)
136         E{i,j} = (M_plus{i,j}(1,1)*exp(-1i*eps_c(i,j)*(d(i) ...
137             -xpos{i,1}))...
138             +M_plus{i,j}(2,1)*exp(1i*eps_c(i,j)*(d(i) ...
139             -xpos{i,1})))...
140             ./(M_minus{i,j}(1,1)*M_plus{i,j}(1,1) ...
141             *exp(-1i*eps_c(i,j)...
142             *d(i))+M_minus{i,j}(1,2)*M_plus{i,j}(2,1) ...
143             *exp(1i*eps_c(i,j)*d(i)));
144     end
145 end
146 dx = [0,dx];
147 n_cell = cell(length(d),1);
148 Eabs2 = abs(cell2mat(E(:,:)')).^2;
149 Enorm = (Eabs2-min(Eabs2(:)))/(max(Eabs2(:))-min(Eabs2(:)));
150 max_E = max(Enorm(:));
151 Efield{l} = Enorm;
152 f=1.5;
153 fig = figure('Position', [10 10 f*500 f*375]);
154 left_color = [0 0 1];
155 right_color = [1 0 0];
156 set(fig,'defaultAxesColorOrder',[left_color; right_color]);
157
158 set(gca,'fontsize',20)
159 for i = 1:length(d)
160     xpos{i,1} = dx(i)+xpos{i,1};
161     n_cell{i,1} = ...
          n_c{i+1,1}(1,296)*ones(length(xpos{i,1}),1); % ...
          refractive index at 600 nm
162     yyaxis right
163     ylabel('\fontsize{22}\Re(n)')
```

```
164     plot(xpos{i},real(n_cell{i}),'r-','LineWidth',1.5) % ...
            horizontal red lines
165     hold on
166     ylim([0,2])
167     yyaxis left
168     ylabel('\fontsize{22}Normalised E')
169     xlim([0,max(xpos{i})])
170 end
171   xlabel('\fontsize{22}Total length (nm)')
172 for i = 2:length(d)
173 ypoints{i-1,1} = [real(n_cell{i-1,1}(end)),real(n_cell{i,1}(1))];
174 xpoints{i-1,1} = [dx(i),dx(i)];
175 yyaxis right
176 plot(xpoints{i-1,1},ypoints{i-1,1},'r-','LineWidth',1.5)
177 hold on
178
179 end
180 hold off
181
182 xx = cell2mat(xpos');
183 yyaxis left
184 plot(xx,Enorm(296,:)./max(Enorm(296,:)),'LineWidth',1.5)
185 ylabel('\fontsize{22}Normalised E')
186 xlabel('\fontsize{22}Total length (nm)')
187
188 f = 1.5;
189 figure('Position', [10 10 f*500 f*375])
190 surf(xx,lambda,Efield{1},'LineStyle','none','FaceColor','interp')
191 set(gca,'fontsize',20)
192 hcb=colorbar;
193 ylabel(hcb,'\fontsize{22}Normalised E')
194 xlabel('\fontsize{22}Total length (nm)')
195 ylabel('\fontsize{22}Wavelength (nm)')
```

```
xlim([dx(1),dx(end)])
ylim([500 750])
colormap jet
for i = 2:length(d)
    ypoints{i-1,1} = [max(lambda),min(lambda)];
    xpoints{i-1,1} = [dx(i),dx(i)];
    hold on
    line(xpoints{i-1,1},ypoints{i-1,1},max_E*ones(2,1)...
        ,'Color','w','LineWidth',1.5)
end
view(0,90)
%end
% Transmittance and reflectance calculation
for i = 1:length(d)
    for j = 1:length(lambda)
        R(i,j) = abs(M{i,j}(2,1)./M{i,j}(1,1)).^2;
        T(i,j) = ...
            (n_c{end,1}(j)/n_c{1,1}(j))*abs(1./M{i,j}(1,1)).^2;
    end
end

%% 2D Transmission or Reflection plots
T_1 = 100*T(length(d),:);
R_1 = 100*R(length(d),:);
x = lambda(1:length(lambda));
y = T_1(1:length(lambda));

figure
plot(x,y,'LineWidth',2)
set(gca,'fontsize',20)
legend('\fontsize{18}Model')
xlabel('\fontsize{22}Wavelength (nm)')
ylabel('\fontsize{22}Transmittance (%)')
```

```
xlim([500 750])
```

A.3 Exciton/photon fraction of exciton-polaritons

A.3.1 Varying the cavity length L_c

```
clc;
clearvars -except
hbar = 1; % Planck constant, eV*s
c_speed = 1; % speed of light nm/s
n = 1; % refractive index
m=1; % order mode of microcavity
L_c = linspace(0.5,1.5,1001); % cavity length nm
k_x = 0; % in-plane wave-vector
E_exciton = ones(1,length(L_c));
E_cavity = (hbar*c_speed/n)*sqrt(k_x^2+(m./L_c)); % cavity mode
V = 0.1;
gc=0.02;
ge=0.01;
gav = (gc+ge)/2;

for j=1:length(L_c)
    A = [E_cavity(j)+1i*gav/2, V;V, E_exciton(j)-1i*gav/2];
    [e_vec,e_val] = eig(A);
    vec_a1{j} = e_vec(1,1);
    vec_b1{j} = e_vec(1,2);
    vec_a2{j} = e_vec(2,1);
    vec_b2{j} = e_vec(2,2);
    val_lp{j} = e_val(1,1);
    val_up{j} = e_val(2,2);
```

```
end
    vec_a1 = (cell2mat(vec_a1)).^2;
    vec_b1 = (cell2mat(vec_b1)).^2;
    vec_a2 = (cell2mat(vec_a2)).^2;
    vec_b2 = (cell2mat(vec_b2)).^2;
    val_lp = cell2mat(val_lp);
    val_up = cell2mat(val_up);


%%
figure
line(L_c,E_exciton,'LineStyle','-.','Color','k','LineWidth',2);
line(L_c,E_cavity,'LineStyle',':','Color','k','LineWidth',2);
line(L_c,val_up,'LineStyle','-','Color','b','LineWidth',2);
line(L_c,val_lp,'LineStyle','-','Color','r','LineWidth',2);
set(gca,'FontSize',20);
legend('\fontsize{20} Exciton','\fontsize{20} ...
    Cavity','\fontsize{20} Upper band','\fontsize{20} Lower ...
    band','Location','northeast')
ylabel('\fontsize{22} E/E_{ex}')
xlabel('\fontsize{22} L_c/L_0')

figure
plot(L_c,vec_a1,'r:',L_c,vec_b1,'b-.','LineWidth',2)
set(gca,'FontSize',20);
legend('\fontsize{20} Photon','\fontsize{20} Exciton')
ylabel('\fontsize{22} Hopfield coefficients')
xlabel('\fontsize{22} L_c/L_0')

figure
plot(L_c,vec_a2,'r:',L_c,vec_b2,'b-.','LineWidth',2)
set(gca,'FontSize',20);
legend('\fontsize{20} Photon','\fontsize{20} Exciton')
```

```
ylabel('\fontsize{22} Hopfield coefficients')
xlabel('\fontsize{22} L_c/L_0')
```

A.3.2 Varying the in-plane wave-vector $k_{||}$

```
c_speed = 1; % speed of light nm/s
n = 1; % refractive index
m=1; % order mode of microcavity
L_c = 1.3; % cavity length nm
k_x = linspace(-1,1,1001); % in-plane wave-vector
E_exciton = ones(1,length(k_x));
E_cavity = (hbar*c_speed/n)*sqrt(k_x.^2+(m/L_c)); % cavity mode
V = 0.1;
gc=0.02;
ge=0.01;
gav=(gc+ge)/2;

for i=1:length(k_x)
    A = [E_cavity(i)+1i*gav/2, V;V, E_exciton(i)-1i*gav/2];
    [e_vec,e_val] = eig(A);
    vec_a1{i} = e_vec(1,1);
    vec_b1{i} = e_vec(1,2);
    vec_a2{i} = e_vec(2,1);
    vec_b2{i} = e_vec(2,2);
    val_lp{i} = e_val(1,1);
    val_up{i} = e_val(2,2);
end
    vec_a1 = (cell2mat(vec_a1)).^2;
    vec_b1 = (cell2mat(vec_b1)).^2;
    vec_a2 = (cell2mat(vec_a2)).^2;
    vec_b2 = (cell2mat(vec_b2)).^2;
```

```
27      val_lp = cell2mat(val_lp);
28      val_up = cell2mat(val_up);
29
30
31  %%
32  figure
33  line(k_x,E_exciton,'LineStyle','-.','Color','k','LineWidth',2);
34  line(k_x,E_cavity,'LineStyle',':','Color','k','LineWidth',2);
35  line(k_x,val_up,'LineStyle','-','Color','b','LineWidth',2);
36  line(k_x,val_lp,'LineStyle','-','Color','r','LineWidth',2);
37  set(gca,'FontSize',20);
38  legend('\fontsize{20} Exciton','\fontsize{20} ...
       Cavity','\fontsize{20} Upper band','\fontsize{20} Lower ...
       band','Location','northeast')
39  ylabel('\fontsize{22} E/E_{ex}')
40  xlabel('\fontsize{22} k_{||}/k_{max}')
41
42  figure
43  plot(k_x,vec_a1,'r:',k_x,vec_b1,'b-.','LineWidth',2)
44  set(gca,'FontSize',20);
45  legend('\fontsize{20} Photon','\fontsize{20} Exciton')
46  ylabel('\fontsize{22} Hopfield coefficients')
47  xlabel('\fontsize{22} k_{||}/k_{max}')
48
49  figure
50  plot(k_x,vec_a2,'r:',k_x,vec_b2,'b-.','LineWidth',2)
51  set(gca,'FontSize',20);
52  legend('\fontsize{20} Photon','\fontsize{20} Exciton')
53  ylabel('\fontsize{22} Hopfield coefficients')
54  xlabel('\fontsize{22} k_{||}/k_{max}')
```

Bibliography

1. Plumhof, J. D. *et al.* Room-temperature Bose–Einstein condensation of cavity exciton–polaritons in a polymer. *Nature Materials* **13,** 247–252 (2014).
2. Kasprzak, J. *et al.* Bose–Einstein condensation of exciton polaritons. *Nature* **443,** 409–414 (2006).
3. Amo, A. *et al.* Collective fluid dynamics of a polariton condensate in a semiconductor microcavity. *Nature* **457,** 291–295 (2009).
4. Amo, A. *et al.* Superfluidity of polaritons in semiconductor microcavities. *Nature Physics* **5,** 805–810 (2009).
5. Lerario, G. *et al.* Room-temperature superfluidity in a polariton condensate. *Nature Physics* **13,** 837–841 (2017).
6. Karzig, T. *et al.* Topological Polaritons. *Physical Review X* **5,** 031001 (2015).
7. Reiserer, A. *et al.* Cavity-based quantum networks with single atoms and optical photons. *Reviews of Modern Physics* **87,** 1379–1418 (2015).
8. Guthrie, W. K. C. *A History of Greek Philosophy: Volume 2, the Presocratic Tradition From Parmenides to Democritus* (Cambridge University Press, 1979).
9. Burton, H. E. The Optics of Euclid. *Journal of the Optical Society of America* **35,** 357 (1945).
10. Russell, G. A. Ptolemy's Theory of Visual Perception: An English Translation of the Optics with Introduction and Commentary. A. Mark Smith. *Isis* **89,** 719–720 (1998).

11. Al-Khalili, J. In retrospect: Book of Optics. *Nature* **518,** 164–165 (2015).
12. Al-Haytham [965-1039], I. *et al. Opticae thesaurus* (Basileae : per Episcopios, ETH-Bibliothek Zürich, 1572).
13. Commons, W. *File:Thesaurus opticus Titelblatt.jpg — Wikimedia Commons, the free media repository* [Online; accessed 5-June-2019]. 2018. \url{https://commons.wikimedia.org/w/index.php?title=File:Thesaurus_opticus_Titelblatt.jpg&oldid=322674883}.
14. Newton, I. *Opticks* (Dover Press, 1704).
15. Hooke, R. *Micrographia, or, Some physiological descriptions of minute bodies made by magnifying glasses: with observations and inquiries thereupon* (London: Printed by J. Martyn and J. Allestry, 1665).
16. Huygens, C. *Traite de la Lumiere* (chez Pierre Vander Aa marchand libraire, 1690).
17. Feynman, R. *QED: the strange theory of light and matter* (Princeton University Press, 1985).
18. Maxwell, J. C. A dynamical theory of the electromagnetic field. *Philosophical Transactions of the Royal Society of London* **155,** 459–512 (1865).
19. Stefan, J. Über die Beziehung zwischen der Wärmestrahlung und der Temperatur [On the relationship between heat radiation and temperature]. *Sitzungsberichte der Mathematisch-naturwissenschaftlichen Classe der Kaiserlichen Akademie der Wissenschaften (in German)* **79,** 391–428 (1879).
20. Boltzmann, L. Ableitung des Stefan'schen Gesetzes, betreffend die Abhängigkeit der Wärmestrahlung von der Temperatur aus der electromagnetischen Lichttheorie [Derivation of Stefan's law concerning the dependence of thermal radiation on the temperature of the electro-magnetic theory of light]. *Annalen der Physik und Chemie (in German)* **258,** 291–294 (1884).

21. Wien, W. Temperatur und Entropie der Strahlung [Temperature and entropy of radiation]. *Annalen der Physik (in German)* **288,** 132–165 (1894).
22. Planck, M. Über eine Verbesserung der Wien'schen Spectralgleichung [On an Improvement of Wien's Equation for the Spectrum]. *Verhandlungen der Deutschen Physikalischen Gesellschaft (in German)* **2,** 202–204 (1900).
23. Planck, M. *Vorlesungen über die Theorie der Wärmestrahlung [Lectures on the theory of heat radiation]* (JA Barth, 1906).
24. Einstein, A. Über einen die Erzeugung und Verwandlung des Lichtes betreffenden heuristischen Gesichtspunkt [On a Heuristic Point of View about the Creation and Conversion of Light]. *Annalen der Physik (in German)* **322,** 132–148 (1905).
25. Menghrajani, K. S. *et al.* Hybridization of Multiple Vibrational Modes via Strong Coupling Using Confined Light Fields. *Advanced Optical Materials* **1900403,** 1900403 (2019).
26. Fox, M. *Optical Properties of Solids* (OUP Oxford, 2010).
27. Perot, A *et al.* On the Application of Interference Phenomena to the Solution of Various Problems of Spectroscopy and Metrology. *The Astrophysical Journal* **9,** 87 (1899).
28. Kavokin, A. *et al. Microcavities* (Oxford University Press, Inc., New York, NY, USA, 2008).
29. Pekar, S. Theory of electromagnetic waves in a crystal with excitons. *Journal of Physics and Chemistry of Solids* **5,** 11–22 (1958).
30. Jaynes, E. T. *et al.* Comparison of Quantum and Semiclassical Radiation Theories with Application to the Beam Maser. *Proceedings of the IEEE* **51,** 89–109 (1963).
31. Purcell, E. M. *et al.* Resonance absorption by nuclear magnetic moments in a solid. *Physical Review* **69,** 37–38 (1946).

32. Purcell, E. M. Proceedings of the American Physical Society. *Physical Review* **69,** 681 (1946).
33. Kleppner, D. Inhibited spontaneous emission. *Physical Review Letters* **47,** 233–236 (1981).
34. Goy, P. *et al.* Observation of cavity-enhanced single-atom spontaneous emission. *Physical Review Letters* **50,** 1903–1906 (1983).
35. Sanchez-Mondragon, J. J. *et al.* Theory of spontaneous-emission line shape in an ideal cavity. *Physical Review Letters* **51,** 550–553 (1983).
36. Kaluzny, Y. *et al.* Observation of self-induced Rabi oscillations in two-level atoms excited inside a resonant cavity: The ringing regime of superradiance. *Physical Review Letters* **51,** 1175–1178 (1983).
37. Haroche, S. *et al.* Cavity quantum electrodynamics. *Physics Today* **42,** 24–30 (1989).
38. Raizen, M. G. *et al.* Normal-mode splitting and linewidth averaging for two-state atoms in an optical cavity. *Physical Review Letters* **63,** 240–243 (1989).
39. Zhu, Y. *et al.* Vacuum Rabi splitting as a feature of linear-dispersion theory: Analysis and experimental observations. *Physical Review Letters* **64,** 2499–2502 (1990).
40. Weisbuch, C. *et al.* Observation of the coupled exciton-photon mode splitting in a semiconductor quantum microcavity. *Physical Review Letters* **69,** 3314–3317 (1992).
41. Houdré, R. *et al.* Measurement of cavity-polariton dispersion curve from angle-resolved photoluminescence experiments. *Physical Review Letters* **73,** 2043–2046 (1994).
42. Frey, A. *et al.* Position-dependent exciton-photon mode splitting in a microcavity. *Applied Physics Letters* **64,** 2214–2216 (1994).

43. Schouwink, P. *et al.* Dependence of Rabi-splitting on the spatial position of the optically active layer in organic microcavities in the strong coupling regime. *Chemical Physics* **285,** 113–120 (2002).
44. Wang, S. *et al.* Quantum Yield of Polariton Emission from Hybrid Light-Matter States. *The Journal of Physical Chemistry Letters* **5,** 1433–1439 (2014).
45. Lidzey, D. G. *et al.* Strong exciton-photon coupling in an organic semiconductor microcavity. *Nature* **395,** 53–55 (1998).
46. Lidzey, D. G. *et al.* Observation of strong exciton-photon coupling in semiconductor microcavities containing organic dyes and J-aggregates. *Optical Materials* **12,** 243–247 (1999).
47. Orgiu, E. *et al.* Conductivity in organic semiconductors hybridized with the vacuum field. *Nature Materials* **14,** 1123–1129 (2015).
48. Feist, J. *et al.* Extraordinary Exciton Conductance Induced by Strong Coupling. *Physical Review Letters* **114,** 1–5 (2015).
49. Sung, S. H. *et al.* Stacking, strain, and twist in 2D materials quantified by 3D electron diffraction. *Physical Review Materials* **3,** 064003 (2019).
50. Withers, F *et al.* Light-emitting diodes by band-structure engineering in van der Waals heterostructures. *Nature Materials* **14,** 301 (2015).
51. Li, Y. *et al.* Measurement of the optical dielectric function of monolayer transition-metal dichalcogenides: MoS_2, $MoSe_2$, WS_2, and WSe_2. *Physical Review B* **90,** 205422 (2014).
52. Yu, H. *et al.* in *2D Materials* (eds Avouris, P. *et al.*) 279–294 (Cambridge University Press, 2017).
53. Kormányos, A. *et al.* Monolayer MoS_2: Trigonal warping, the Γ valley, and spin-orbit coupling effects. *Physical Review B* **88,** 045416 (2013).
54. Marinov, K. *et al.* Resolving the spin splitting in the conduction band of monolayer MoS_2. *Nature Communications* **8,** 1938 (2017).

55. Cao, T. *et al.* Valley-selective circular dichroism of monolayer molybdenum disulphide. *Nature Communications* **3,** 887 (2012).

56. Jones, A. M. *et al.* Optical generation of excitonic valley coherence in monolayer WSe2. *Nature Nanotechnology* **8,** 634–638 (2013).

57. Srivastava, A. *et al.* Valley Zeeman effect in elementary optical excitations of monolayer WSe2. *Nature Physics* **11,** 141–147 (2015).

58. Stier, A. V. *et al.* Exciton diamagnetic shifts and valley Zeeman effects in monolayer WS_2 and MoS_2 to 65 Tesla. *Nature Communications* **7,** 10643 (2016).

59. Mak, K. F. *et al.* The valley Hall effect in MoS_2 transistors. *Science* **344,** 1489–1492 (2014).

60. Yu, T. *et al.* Valley depolarization dynamics and valley Hall effect of excitons in monolayer and bilayer MoS_2. *Physical Review B* **93,** 045414 (2016).

61. Fernandez, H. A. *et al.* Electrically tuneable exciton-polaritons through free electron doping in monolayer WS_2 microcavities. *Advanced Optical Materials* **1900484** (2019).

62. Shang, J. *et al.* Observation of Excitonic Fine Structure in a 2D Transition-Metal Dichalcogenide Semiconductor. *ACS Nano* **9,** 647–655 (2015).

63. Houdré, R. *et al.* Saturation of the strong-coupling regime in a semiconductor microcavity: Free-carrier bleaching of cavity polaritons. *Physical Review B* **52,** 7810–7813 (11 1995).

64. Cingolani, R. *et al.* Radiative recombination processes in wide-band-gap II–VI quantum wells: the interplay between excitons and free carriers. *Journal of the Optical Society of America B* **13,** 1268 (1996).

65. Schmitt-Rink, S. *et al.* Theory of transient excitonic optical nonlinearities in semiconductor quantum-well structures. *Physical Review B* **32,** 6601–6609 (1985).

66. Mak, K. F. *et al.* Tightly bound trions in monolayer MoS 2. *Nature Materials* **12,** 207–211 (2013).
67. Liu, X. *et al.* Strong light–matter coupling in two-dimensional atomic crystals. *Nature Photonics* **9,** 30–34 (2015).
68. Lee, B. *et al.* Electrical Tuning of Exciton–Plasmon Polariton Coupling in Monolayer MoS_2 Integrated with Plasmonic Nanoantenna Lattice. *Nano Letters* **17,** 4541–4547 (2017).
69. Flatten, L. C. *et al.* Electrically tunable organic–inorganic hybrid polaritons with monolayer WS_2. *Nature Communications* **8,** 14097 (2017).
70. Graf, A. *et al.* Electrical pumping and tuning of exciton-polaritons in carbon nanotube microcavities. *Nature Materials* **16,** 911–917 (2017).
71. Chakraborty, B. *et al.* Control of Strong Light-Matter Interaction in Monolayer WS_2 through Electric Field Gating. *Nano Letters* **18,** 6455–6460 (2018).
72. Finkelstein, G. *et al.* Optical Spectroscopy of a Two-Dimensional Electron Gas near the Metal-Insulator Transition. *Physical Review Letters* **74,** 976–979 (1995).
73. Flatten, L. *et al.* Spectral engineering of coupled open-access microcavities. *Laser & Photonics Reviews* **10,** 257–263 (2016).
74. Fernandez, H. *et al. Design of strong-coupling microcavities for optoelectronic applications* in *2017 Conference on Lasers and Electro-Optics Europe European Quantum Electronics Conference (CLEO/Europe-EQEC)* (2017), 1–1.
75. Commons, W. *File:20cm Air 1.jpg — Wikimedia Commons, the free media repository* [Online; accessed 20-May-2019]. 2015. `\url{https://commons.wikimedia.org/w/index.php?title=File:20cm_Air_1.jpg&oldid=175158520}`.
76. Rakić, A. D. *et al.* Optical properties of metallic films for vertical-cavity optoelectronic devices. *Applied Optics* **37,** 5271 (1998).

77. Chilwell, J. *et al.* Thin-films field-transfer matrix theory of planar multilayer waveguides and reflection from prism-loaded waveguides. *Journal of the Optical Society of America A* **1,** 742 (1984).

78. Pettersson, L. A. A. *et al.* Modeling photocurrent action spectra of photovoltaic devices based on organic thin films. *Journal of Applied Physics* **86,** 487–496 (1999).

79. Rodriguez, S. R.-K. Classical and quantum distinctions between weak and strong coupling. *European Journal of Physics* **37,** 025802 (2016).

80. Novotny, L. Strong coupling, energy splitting, and level crossings: A classical perspective. *American Journal of Physics* **78,** 1199 (2010).

81. Bender, C. M. *et al.* Must a Hamiltonian be Hermitian? *American Journal of Physics* **71,** 1095–1102 (2003).

82. Bender, C. M. *et al.* Real Spectra in Non-Hermitian Hamiltonians Having $\mathcal{PT}$ Symmetry. *Physical Review Letters* **80,** 5243–5246 (1998).

83. Bender, C. M. *et al. PT Symmetry: of classical anf quantum systems* (World Scientific (Europe), 2019).

84. Savona, V. *et al.* Quantum well excitons in semiconductor microcavities: Unified treatment of weak and strong coupling regimes. *Solid State Communications* **93,** 733–739 (1995).

85. Hopfield, J. J. Theory of the contribution of excitons to the complex dielectric constant of crystals. *Physical Review* **112,** 1555–1567 (1958).

86. Chernikov, A. *et al.* Electrical Tuning of Exciton Binding Energies in Monolayer WS_2. *Physical Review Letters* **115,** 126802 (2015).

87. Zhang, K. *et al.* Two dimensional hexagonal boron nitride (2D-hBN): synthesis, properties and applications. *Journal of Materials Chemistry C* **5,** 11992–12022 (2017).

88. Zhu, B. *et al.* Exciton Binding Energy of Monolayer WS_2. *Scientific Reports* **5,** 9218 (2015).

89. Wang, S. *et al.* Coherent Coupling of WS_2 Monolayers with Metallic Photonic Nanostructures at Room Temperature. *Nano Letters* **16,** 4368–4374 (2016).

90. Ye, Z. *et al.* Probing excitonic dark states in single-layer tungsten disulphide. *Nature* **513,** 214–218 (2014).

91. Chernikov, A. *et al.* Population inversion and giant bandgap renormalization in atomically thin WS_2 layers. *Nature Photonics* **9,** 466–470 (2015).

92. Fernandez, H. A. *et al.* Electrically tuneable exciton energy exchange between spatially separated 2-dimensional semiconductors in a microcavity. *Applied Physics Letters* **115,** 071103 (2019).

93. Coles, D. M. *et al.* Polariton-mediated energy transfer between organic dyes in a strongly coupled optical microcavity. *Nature materials* **13,** 712–9 (2014).

94. Zhong, X. *et al.* Non-radiative energy transfer mediated by hybrid light-matter states. *Angewandte Chemie - International Edition* **55,** 6202–6206 (2016).

95. Georgiou, K. *et al.* Control over Energy Transfer between Fluorescent BODIPY Dyes in a Strongly Coupled Microcavity. *ACS Photonics* **5,** 258–266 (2018).

96. Lidzey, D. G. *et al.* Photon-mediated hybridization of Frenkel excitons in organic semiconductor microcavities. *Science* **288,** 1620–1623 (2000).

97. Zhong, X. *et al.* Energy Transfer between Spatially Separated Entangled Molecules. *Angewandte Chemie International Edition* **56,** 9034–9038 (2017).

98. Andrew, P *et al.* Forster energy transfer in an optical microcavity. *Science* **290,** 785–788 (2000).

99. Du, M. *et al.* Theory for polariton-assisted remote energy transfer. *Chemical Science* **9,** 6659–6669 (2018).

100. Waldherr, M. *et al.* Observation of bosonic condensation in a hybrid monolayer MoSe2-GaAs microcavity. *Nature Communications* **9,** 3286 (2018).

101. Sidler, M. *et al.* Fermi polaron-polaritons in charge-tunable atomically thin semiconductors. *Nature Physics* **13,** 255–261 (2017).

102. Pau, S. *et al.* Microcavity exciton-polariton splitting in the linear regime. *Physical Review B* **51,** 14437–14447 (1995).

103. Törmä, P *et al.* Strong coupling between surface plasmon polaritons and emitters: a review. *Reports on Progress in Physics* **78,** 013901 (2015).

104. Hagenmüller, D. *et al.* Cavity-Enhanced Transport of Charge. *Physical Review Letters* **119,** 223601 (2017).

105. Chen, Y.-J. *et al.* Valley-polarized exciton–polaritons in a monolayer semiconductor. *Nature Photonics* **11,** 431–435 (2017).

106. Dufferwiel, S *et al.* Valley coherent exciton-polaritons in a monolayer semiconductor. *Nature Communications* **9,** 4797 (2018).